Integration and Processing of High-Resolution Moiré-Interferometry Data

by

Shih-Yung Lin

Dissertation submitted to the Faculty of the
Virginia Polytechnic Institute and State University
in partial fulfillment of the requirements for the degree of

DOCTOR OF PHILOSOPHY
in
Engineering Mechanics

APPROVED:

R. Czarnek, Chairman

J. Morton

D. T. Mook

C. W. Smith

R. Claus

May, 1992
Blacksburg, Virginia

Integration and Processing of High-Resolution Moiré-Interferometry Data

by

Shih-Yung Lin

Committee Chairman : Robert Czarnek

Engineering Mechanics

(ABSTRACT)

A new hybrid method combining moiré interferometry, high-resolution data-reduction technique, two-dimensional data-smoothing method, and Finite Element Method (FEM) has been successfully developed. This hybrid method has been applied to residual strain analyses of composite panels, strain concentrations around optical fibers embedded in composites, and cruciform composite shear test.

This hybrid method allows moiré data to be collected with higher precision and accuracy by digitizing overexposed moiré patterns (U & V fields) with appropriate carrier fringes. The resolution of the data is ± 20 nm. The data extracted from the moiré patterns are interfaced to an FEM package through an automatic mesh generator. This mesh generator produces a non-uniform FEM mesh by connecting the digitized data points into

triangles. The mesh, which uses digitized displacement data as boundary conditions, is then fed to and processed by a commercial FEM package.

Due to the natural scatter of the displacement data digitized from moiré patterns, the accuracy of strain values is significantly affected. A modified finite-element model with linear spring elements is introduced so data-smoothing can be done easily in two-dimensional space. The results of the data smoothing are controlled by limiting the stretch of those springs to be less than the resolution of the experimental method.

With the full-field hybrid method, the strain contours from moiré interferometry can be easily obtained with good accuracy. If the properties of the material are known, the stress patterns can also be obtained. In addition, this method can be used to analyze any two-dimensional displacement data, including the grid method and holography.

The application of this method will be demonstrated with a composite residual strain test and a cruciform composite shear test. The latter case is also compared with the localized hybrid method [1,2] which uses only the boundary conditions defined on the perimeter of the region of interest. The precision of the full-field hybrid method will also be investigated by using a numerical model.

Acknowledgment

The author wishes to express his sincere appreciation to Dr. Czarnek, the chairman of the committee, for his assistance and guidance during this research. Dr. Czarnek has shared with the author his intelligent ideas and valuable experiences on the technical issues of this work. Also his deep concerns on author's non-technical matters are greatly appreciated.

In addition, the author wishes to thank

- his committee members for their participation and guidance,
- Joosik Lee for his help in experimental techniques and friendship, and other colleagues, Ifan Guo, Ray Boeman, Peter Ifju, Tom Rantis, Jau-Je Wu, Chi-Way Chang, Lei Wang, and Bongtae Han for their corporation and friendship,
- M. Y. Tsai and Diane Peters for their assistance in the cruciform test and friendship,
- Vicky Czarnek for her constant concern and friendship,
- his family and in-laws whose support were indispensable for the author to accomplish his work,
- his wife, Li-Hua, for her sacrifice and encouragement, and his son, Michael, for his great smiles and hugs,
- National Science Foundation — Science and Technology Center for the financial support.

TABLE OF CONTENTS

ABSTRACT II
ACKNOWLEDGMENT IV
TABLE OF CONTENTS V
LIST OF FIGURES VII
1 INTRODUCTION 1
2 LITERATURE REVIEW 8
2-1 Moiré Interferometry 8
2-2 Moiré Interferometry Data Reduction and Analysis 9
2-3 Hybrid Methods 10
2-4 Smoothing of Full-Field Displacement Data 11
3 MOIRÉ INTERFEROMETRY 13
3-1 Moiré Interferometers for Two-Dimensional Applications 15
3-2 Moiré Pattern Analysis 19
3-3 Carrier Fringes 21
3-4 Grating Replication Process 27
4 HIGH-RESOLUTION DATA-REDUCTION TECHNIQUE AND NON-UNIFORM MESH GENERATION 29
4-1 Fringe Pattern Recording 29
4-2 Non-Uniform-Mesh Generator 31
5 MODIFIED FINITE-ELEMENT MODEL FOR THE FULL-FIELD DATA SMOOTHING 37
5-1 One-Dimensional Data Smoothing 38
5-2 Two-Dimensional Data Smoothing 40
5-3 Result Interpretation 42
5-4 Criterion of Data Smoothing 43
6 ERROR EVALUATION OF THE FULL-FIELD HYBRID METHOD 44
6-1 Size of the Test Section and Density of the Data Points 44
6-2 Optical System Tuning 45

6-3 Optical Noise 45
6-4 Magnification Factor of the Picture 46
6-5 Carrier Fringes 46
6-6 Resolution of the Digitizing Tablet 47
6-7 Behavior of the Triangular Elements 47
6-8 Calculation Error 48
6-9 Data Smoothing 48
6-10 Summary of Error Evaluation 54
7 APPLICATION OF THE FULL-FIELD HYBRID METHOD - COMPOSITE RESIDUAL STRAIN MEASUREMENT 55
7-1 Specimen and Test Procedures 55
7-2 Test Results 57
7-3 Numerical Process 57
7-4 Data Smoothing and Results 62
8 THE LOCALIZED HYBRID METHOD AND THE FULL-FIELD HYBRID METHOD - CRUCIFORM COMPOSITE SHEAR TEST 72
8-1 Cruciform Composite Shear Test with Moiré Interferometry 72
8-2 The Results of the Localized Hybrid Method 76
8-3 The Results of the Full-Field Hybrid Method 82
8-4 Mechanical Differentiation and Strain Gage Result 86
8-5 Discussion 92
9 SUMMARY 95
10 CONCLUSIONS 99
APPENDIX A 100
APPENDIX B 101
REFERENCES 104
VITA 108

LIST OF FIGURES

Figure 3.1 Basic two-beam moiré interferometer 14
Figure 3.2 Three-mirror four-beam moiré interferometer 16
Figure 3.3 Achromatic moiré interferometer 18
Figure 3.4 Achromatic moiré interferometer for two-dimensional applications 20
Figure 3.5 Geometric approach of moiré pattern analysis 23
Figure 3.6 The effects of the carrier fringes of rotation 26
Figure 3.7 Specimen grating replication process 28
Figure 4.1 The horizontal displacement pattern of the graphite-PEEK composite specimen. Low-contrast photographic process was used. 30
Figure 4.2 The horizontal displacement pattern of the graphite-PEEK composite specimen. High-contrast photographic process was used. The black fringes are much thinner than the white ones. 32
Figure 4.3 The horizontal displacement pattern of the graphite-PEEK composite specimen. High-contrast photographic process and carrier fringes of rotation were used. 33
Figure 4.4 The non-uniform mesh created according to the coordinates of the digitized points. 35
Figure 4.5 Digitally recreated displacement contour. The thick contours match the fringes of the picture. The thin contours are fractional with contour interval equals to 42nm. 36
Figure 5.1 (a)-(d) One-dimensional data-smoothing model 39
Figure 5.2 Two-dimensional data-smoothing model, a flat plate of triangular elements resting on a matrix of springs ..41
Figure 6.1 The strain distribution along the x-axis. An 9x9 array of data points is used. 50
Figure 6.2 The strain contour without data smoothing. A 17x17 array of data points is used. 51

Figure 6.3 The strain contour with data smoothing. A 17x17 array of data points is used. 52
Figure 6.4 The strain distribution along the x-axis. A 17x17 array of data points is used. 53
Figure 7.1 AS4 graphite-PEEK (APC2) composite residual test specimen with fibers perpendicular to the test surface. The thickness of the specimen is 2.2mm 56
Figure 7.2 (a) Horizontal and (b) vertical displacement patterns of the AS4-PEEK composite residual strain test. 58
Figure 7.3 (a) Horizontal and (b) vertical displacement patterns of the composite residual strain test with carrier fringes of rotation and overexposure 59
Figure 7.4 Digitally recreated U-field of the composite residual test. The thick contours represent the original fringes and the thin contours represent fractional fringes. Contour intervals are 417 nm and 42 nm, respectively. 60
Figure 7.5 Digitally recreated V-field of the composite residual test. The thick contours represent the original fringes and the thin contours represent fractional fringes. Contour intervals are 417 nm and 42 nm, respectively. 61
Figure 7.6 The smoothed U-displacement contour 63
Figure 7.7 The smoothed V-displacement contour 64
Figure 7.8 The horizontal strain contour (ε_x) with data smoothing 65
Figure 7.9 The vertical strain contour (ε_y) with data smoothing ...66
Figure 7.10 The shear strain contour (γ_{xy}) with data smoothing ...67
Figure 7.11 The horizontal strain (ε_x) contour without data smoothing 69
Figure 7.12 The vertical strain (ε_y) contour without data smoothing 70
Figure 7.13 The shear strain (γ_{xy}) contour without data smoothing 71

Figure 8.1 Cruciform composite shear test specimen 73
Figure 8.2 Cruciform composite shear test fixture 75
Figure 8.3 Horizontal (U) displacement pattern of the cruciform composite shear test. 77
Figure 8.4 Vertical (V) displacement pattern of the cruciform composite shear test. 78
Figure 8.5 Horizontal strain distribution of the cruciform composite specimen from the localized hybrid method. 79
Figure 8.6 Vertical strain distribution of the cruciform composite specimen from the localized hybrid method. 80
Figure 8.7 The maximum shear strain (γ_{12}) distribution of the cruciform composite specimen from the localized hybrid method. 81
Figure 8.8 A random mesh created according to the digitized coordinates. 83
Figure 8.9 The smoothed U-displacement contour of the cruciform composite shear test from the full-field hybrid method. 84
Figure 8.10 The smoothed V-displacement contour of the cruciform composite shear test from the full-field hybrid method. 85
Figure 8.11 Horizontal strain distribution of the cruciform composite specimen from the full-field hybrid method. 87
Figure 8.12 Vertical strain distribution of the cruciform composite specimen from the full-field hybrid method. 88
Figure 8.13 The maximum shear strain distribution (γ_{12}) of the cruciform composite specimen from the full-field hybrid method 89
Figure 8.14 Mechanically differentiated U-field. The pattern represents horizontal strain contour 90

Figure 8.15 Mechanically differentiated U-field. The pattern represents horizontal strain contour 91
Figure 8.16 Comparison of the maximum shear strain distribution (γ_{12}) along the horizontal center line obtained from both hybrid methods. 93

1. INTRODUCTION

Moiré interferometry is a full-field, high-sensitivity optical method that measures displacement distribution on the surface of a specimen. A sensitivity of 417 nm per fringe order is commonly used. The sensitivity of the moiré interferometry is high. However, it is hard to extract useful data from a test area if it contains only a few fringes. Typical examples include residual strain measurement, the high-stiffness material test, and a small region of interest.

There are basically two ways to handle the problem of pattern analysis with only a few fringes: increasing the sensitivity and enhancing the resolution. The sensitivity can be increased by reducing the wavelength of the laser light and/or increasing the incidence angle of the optical system. The former option requires a much higher priced laser and increases the risk of workers. The latter option reduces the diffraction efficiency and, therefore, requires a high-efficiency grating or higher-power laser. Also, the 417 nm sensitivity is already 50% to 80% of the theoretical limit*

---

* The theoretical limit of sensitivity is defined as the maximum sensitivity of a moiré system with an incidence angle of 90°. In this situation, the corresponding sensitivity is $\lambda/2$ per fringe order. From physical reasoning, a 90° incidence angle will have zero

for the visible light. There is not much room to increase the sensitivity by increasing the incidence angle. In order to enhance the resolution of pattern interpretation, digital imaging techniques [3, 4, 5, 6] are used to resolve fractional fringes in a moiré pattern. This approach requires an image-processing system and suffers from optical noise. The high-resolution data-reduction technique [7, 8] approaches this low-fringe-density situation by introducing carrier fringes (either rotational or extensional). The function of the carrier fringes [9] is to increase the fringe vector. The fringe density, therefore, is increased, and it is much easier to locate the center of a fringe. If the moiré pattern is overexposed, the fringes with minimum intensity will be much thinner, about 10% of the distance between two fringes. The displacement patterns with carrier fringes and overexposure are digitized instead of the original low-fringe-density patterns. The data points are selected right on the thin (black fringes on the pictures) fringes; thus, the resolution is enhanced to $\pm$ 20 nm. The carrier fringes are then removed from the digitized data, and the original pattern is recovered with high resolution. This technique requires extra numerical processing but the moiré system need not be changed at all.

---

intensity illuminating the specimen, and therefore no diffraction from the specimen.

The resolution of the moiré pattern becomes very critical when the fringes are sparse. In taking derivatives (to determine strains), the error will be magnified. The high-resolution data-reduction technique enhances the resolution to ± 20 nm. However, the accuracy of the strain fields is still hardly acceptable. Also the time involved in the pattern analysis is very long.

To obtain accurate derivatives and reduce the time of pattern analysis, a new hybrid method is developed. The hybrid method defined here combines an experimental method for a material property measurement and a numerical analysis for the test result processing. In this study, the moiré interferometry is the experimental method, and the finite element (FE) analysis with a data-smoothing model is the numerical tool.

The optical system set-up of the moiré interferometry varies depending upon the applications. For two-dimensional in-plane applications, the moiré systems used in this study included the three-mirror four-beam system [10, 11] and the achromatic system [11, 12, 13]. Even though both systems have their advantages and disadvantages, the test results are exactly the same. It does not matter what moiré interferometer is used to produce the fringe patterns for the hybrid method.

The test procedures of the moiré interferometry need not be changed in the hybrid method, except the fact that the fringe-

pattern recording is done according to the requirements of the high-resolution data-reduction technique. Those requirements are the over-exposure of the film and the introduction of appropriate carrier fringes.

In the digitizing process of moiré patterns, the data points are selected right along the center of the thin fringes (points with the highest resolution) produced by overexposure. The density of the data points will be determined according to the nature of the specimen geometry and the loading condition. The patterns are digitized with a digitizing tablet. The nodal coordinates and displacement information are stored in two computer files and ready to be processed.

Since the data points are constrained to be located at the center of a fringe, they are not regularly spaced. Therefore, a non-uniform FE mesh is created instead of a uniform one. The mesh using triangular elements represents a plate, and linear springs are attached to each node of the triangular mesh. To save time on mesh generation, this work is done automatically by a computer program. The digitized displacement data need to be processed if the carrier fringes are introduced. The removal of carrier fringes is performed by comparing the recreated contours with the original patterns without carrier fringes or known boundary conditions. This part of work is also done by the same program with the user's interactive input.

The previous results are interfaced to create a modified two-dimensional data-smoothing FE model. This model contains a thin plate resting on a matrix of springs attached to each node on the plate. The other ends of the springs are loaded with one of the two in-plane displacement data. The model is written into a batch file for a commercial finite element method (FEM) package to be read and analyzed directly. No manual mesh generation is required.

The quality of the data-smoothing is controlled by the relative stiffness of the plate and springs. If the plate stiffness approaches zero compared to the spring constant, the nodal displacement on the plate will match the displacement boundary conditions applied to the springs. However, as we increase the stiffness of the plate, the displacement field will be smoothed, and we obtain unique nodal partial derivatives at the nodes on the plate. These partial derivatives are the smoothed strain values with minimal error caused by the scatter of the digitized data. The smoothing criterion is determined according to the nature of the data. From the high-resolution data-reduction technique, it is proven that the resolution of the data is ± 20 nm. Therefore, the difference between the original displacement field and the smoothed displacement field shall not exceed the resolution at any node on the plate.

The FEM results are obtained as a data file, and are processed by a computer program. The results carry smoothed displacement data and much more accurate strain contours if the smoothing

criterion is satisfied. The stress component can be calculated later if the material properties are known. The contours of the displacements, strains, and even stresses can then be produced by the computer program.

There are three objectives for this study to achieve. The first one is to make the high-resolution data-reduction technique a practical research tool. The second objective of this study is to develop a complete full-field hybrid method for two-dimensional moiré data analysis with controlled data smoothing. The last objective is to shorten the total time required for pattern analysis by using well-designed computer programs. The results of this hybrid method are much better than those of the traditional method, in both quality and quantity.

Two real cases have been studied with this full-field hybrid method - composite residual strain test and cruciform composite shear test. The first case contains fewer than three fringes and has a small test area. The results are presented in Chapter 7. The second case has a lot more fringes and a large test area. The localized hybrid method [1,2] has also been used for comparison. The results are presented in Chapter 8. The major differences between the hybrid methods are as follows: the localized method uses displacement boundary conditions, a regular manually-created mesh, and material property data; at the same time, the full-field method uses full-field displacement data, a random automatically-created

mesh, data smoothing, and high-resolution data-reduction technique. No material property data are required, unless stress results are required.

A numerical case is presented in Chapter 6 to model the experimental result. The accuracy and sampling effect are investigated.

2 LITERATURE REVIEW

2-1 Moiré Interferometry

Moiré interferometry was introduced in 1965 by Guild [14] as a method of measuring displacements in one in-plane direction on a flat surface. When lasers became available in the 1960s, moiré interferometry was found to have practical applications in high-sensitivity displacement measurement. After decades of development, moiré interferometry has become a full-field, high-sensitivity optical method that measures in-plane and out-of-plane displacements on the surface of a specimen.

The three-mirror four-beam moiré interferometry system [10, 11] has been widely used for two-dimensional measurement of in-plane displacements. This system provided convenience and compactness, since all three mirrors were arranged together. As with other optical methods, a vibration isolation system was required. An achromatic system was introduced by Czarnek [12, 13] in 1984. This system reduced the requirement of the vibration isolation system and could be used with a testing machine. Also, the coherence of the light used was not critical. A broad-band light source, like a laser diode, could be used. A different moiré interferometer was also used by Tuttle and Klein [15]. Four mirrors were used to reflect a collimated light source in four directions. Another set of four mirrors was used to redirect beams to the right

directions. The emergent beams from the specimen were redirected by an additional mirror and photographed. This system provided the advantage that the optical components did not need to be close to the specimen.

Usually, a moiré test requires the switching of fields to isolate two displacement patterns. Therefore, the applications are limited to the static experiments. Dadkhah et al. [16] added a beam splitter and two polarizers to a three-mirror moiré system. Using those two displacement fields yielded different polarization directions; the fringe patterns were directed into two perpendicular directions and polarized individually. Two displacement patterns were thus recorded separately. This method allowed simultaneous on-line measurements of orthogonal displacement fields.

The sensitivity of the moiré interferometer commonly used is 417 nm per fringe order. Depending upon the method of recording, the resolution of a moiré pattern ranges from 1/20 to 1/4 of a fringe, which corresponds to 20 nm and 100 nm, respectively.

2-2 Moiré Interferometry Data Reduction and Analysis

Moiré interferometry results come in displacement fringe patterns. The patterns are recorded on high-resolution films. A picture is usually exposed so that black and white fringes have the same width. This is also the conventional way of moiré pattern recording. The displacement data are extracted manually or by using

a digitizing tablet. The resolution is about 1/4 of a fringe. Strain components are derived by measuring the distance between points and the difference of their fringe orders. The slope of a fringe line can also be used to calculate strains. This conventional method is simple and no elaborate equipment is required. However, the accuracy of the results is limited.

New methods of moiré data acquisition include digital image processing [3, 4, 5, 6] and high-resolution data-reduction techniques [7, 8, 17]. The former requires a computer, a high-resolution video system, and an image processor. Fractional fringes can be obtained by using gray-level analysis, but optical noise needs to be properly removed. The latter method changes the way of pattern recording. A film is over-exposed to get much thinner black fringes on high contrast paper. The resolution is thus enhanced to about 20 nm. The data are further organized digitally and are ready to be analyzed. Also, the resolution of a film is much higher than a video camera.

2-3 Hybrid Methods

Hybrid Method is a combination of numerical and experimental approaches. While the experimental data serve as boundary conditions, finite-element method is used for the analysis.

Weathers et al. [18] combined laser-speckle technique and finite-element method, and studied the stress pattern around a hole. The displacement values around a local zone of interest were

digitized and used as boundary conditions of the finite-element model. They concluded that the advantages of the integrated approach are evident; however, randomly distributed errors in experimental displacement will substantially alter the calculated stress field. Morton et al. [1] and Tsai [2] approached the problem with a localized hybrid method that combined moiré interferometry and finite element method. Both approaches required correct constitutive law for the material so the equilibrium conditions could be satisfied exactly. With the St. Venant's principle, the effect of experimental scatter for both approaches would be negligible as long as a node was away from the boundary where the displacement data were specified. The advantage of these methods was the fact that the numerical or mechanical differentiation was not required. The analytical process was thus simplified.

2-4 Smoothing of Full-Field Displacement Data

The scatter of the digitized displacement data is magnified in the differentiation process. To minimize the error in the derivatives, a proper data-smoothing scheme is needed. Rowlands and Segalman [19, 20] used spline-like finite-element differentiation to process full-field experimental data over a small discrete region. The approximating functional in their finite element analyses could be interpreted physically as the strain energy of a plate loaded by stretched springs attached at the data locations. These techniques were used in mechanics studies, such as

fracture parameter determination [21, 22]. Due to the high fringe count near the crack tip, the resolution of the data was not critical. For low fringe density situations, data reduction with higher resolution is recommended. If a data smoothing scheme and a high-resolution data-reduction technique are combined, the accuracy of the results can be significantly enhanced.

3 MOIRÉ INTERFEROMETRY

Moiré interferometry is an optical method that provides full-field information about in-plane surface displacements. It is based on two-beam interference. As shown in Figure 3.1, a high-frequency diffraction grating is replicated on the surface of the specimen and deforms together with it. This specimen grating is illuminated by two mutually coherent and collimated beams of laser. Their +1 and -1 diffraction orders carry information about the deformation of the specimen grating. If the specimen is not loaded, the grating consists of straight and parallel lines. The wave fronts of these diffraction orders are flat and parallel to each other. The interference pattern is a uniform-intensity field. This is called a null pattern. However, if the specimen deforms, the grating changes the spacing between lines and/or rotates accordingly. The wave fronts are warped. The phase differences of these two beams thus vary from point to point and form fringes of constructive and destructive interference. This interference pattern is a contour map of in-plane displacement in the direction perpendicular to the grating lines. Therefore, a grating of vertical lines forms a horizontal displacement pattern, a U-field. Similarly a grating of horizontal lines forms a vertical displacement pattern, a V-field. The sensitivity is equal to half the distance between grating lines.

The system set-up shown in Figure 3.1 is a two-beam interferometer. This system is used to detect one in-plane

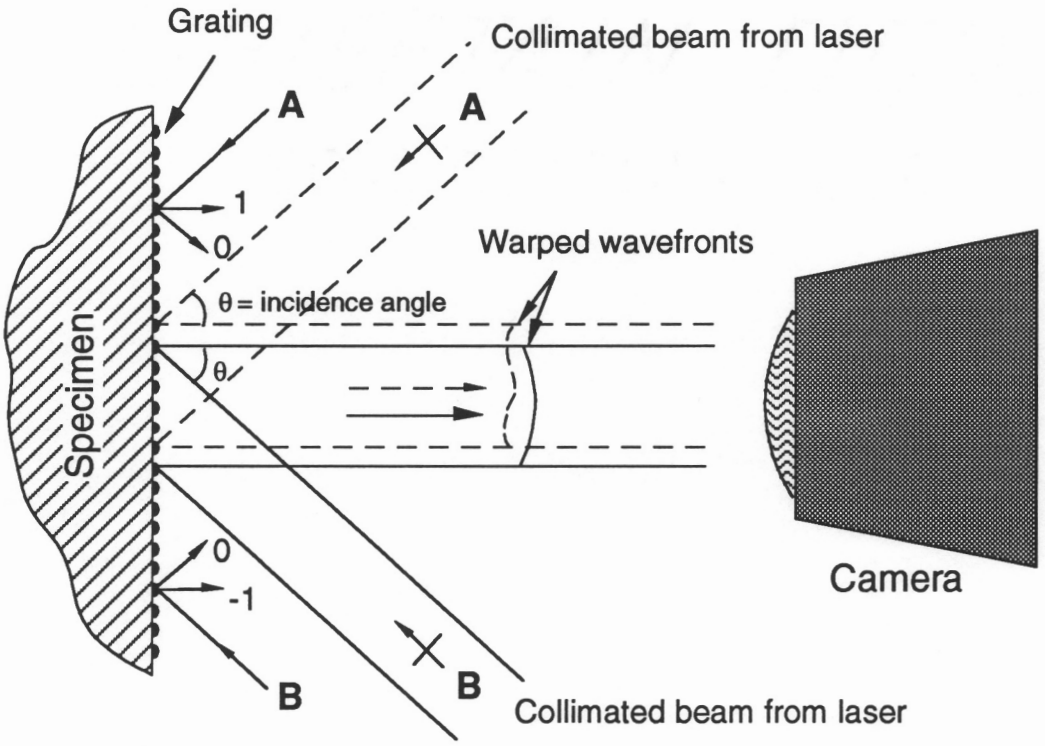

Figure 3.1 Basic two-beam moiré interferometer

displacement at a time. If another in-plane displacement field is needed, the system and the specimen need to be rotated by exactly 90° relative to each other. It is not practical for high-sensitivity moiré interferometry, because any small deviation from 90° rotation can produce a huge error on the shear strain. Also, rotation of either the specimen or the optical system makes the test very complicated.

For two-dimensional applications, a three-mirror four-beam moiré interferometer or an achromatic moiré interferometer is much easier to use. These moiré systems are used in this study in two different cases. They are discussed in the following section.

3-1 Moiré Interferometers For Two-Dimensional Applications

A three-mirror four-beam moiré interferometer [10, 11] shown in Figure 3.2 is used for the composite residual-strain test. It will be discussed in Chapter 7. Two mirrors aligned in ±45 degrees are added to the two-beam system. These two mirrors provide another two beams, forming the interference pattern of the vertical displacement field. A cross grating is replicated on the specimen surface instead of a linear grating. The cross grating consists of two sets of parallel lines perpendicular to each other or a matrix of equally spaced dots. The laser light diffracts in both in-plane directions, providing two orthogonal components of displacement at the same time. An aperture is added to separate the displacement patterns. We can record a horizontal displacement field by blocking

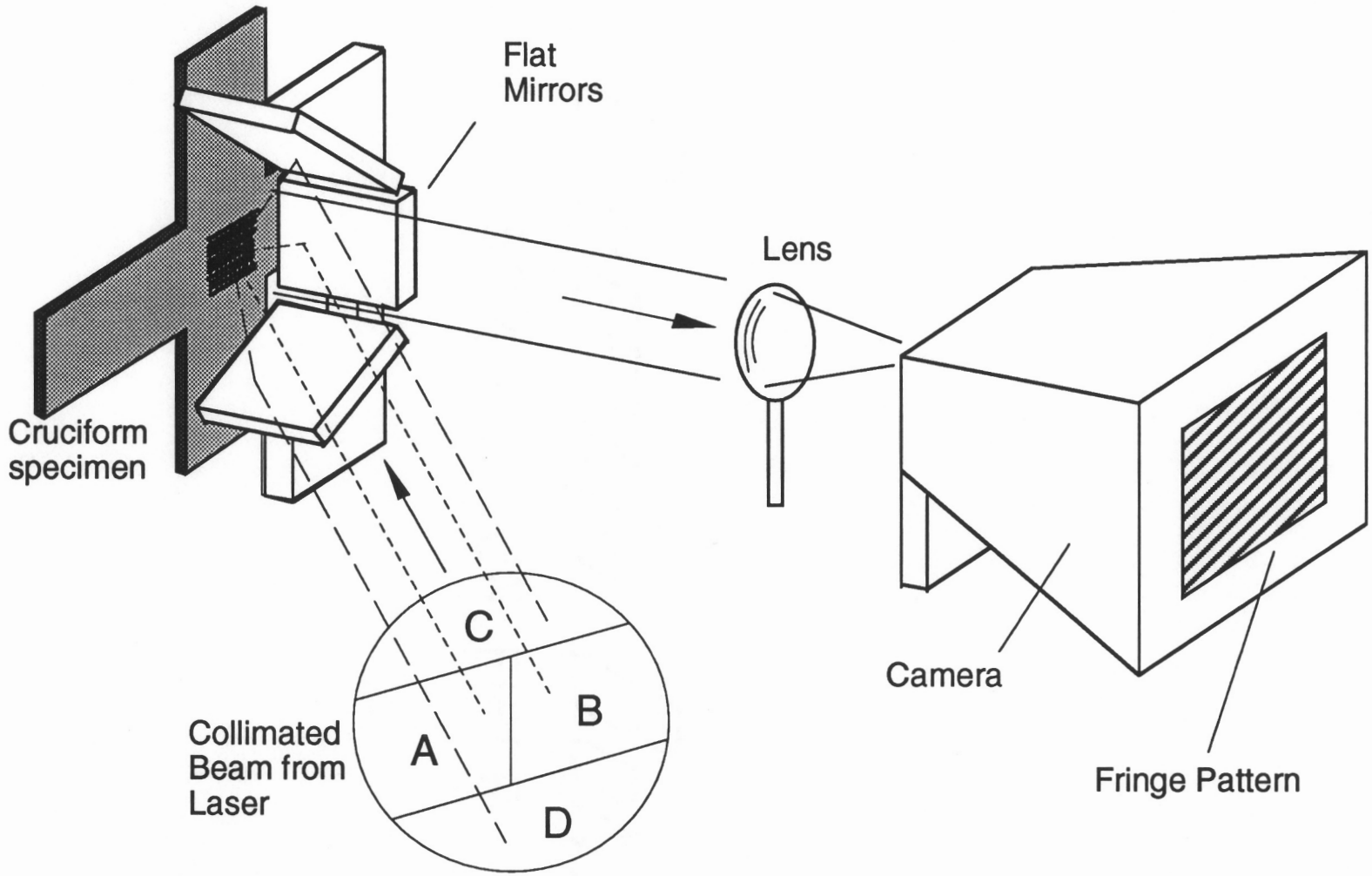

Figure 3.2 Three-mirror four-beam moiré interferometer

C and D beams, or record vertical displacement field by blocking A and B beams. The in-plane strain tensors (ε_x, ε_y, γ_{xy}) can be obtained from these two in-plane displacement patterns. Since optical components of the moiré system have no relative movement during the test, the shear strain is obtained accurately.

For a testing environment that has some minor vibration, an achromatic moiré system [11, 12, 13] shown in Figure 3.3 is preferred over a three-mirror four-beam system. The achromatic system is used in the cruciform composite shear test. It will be discussed in Chapter 8. A compensation grating is illuminated by a collimated light source. The propagation direction is perpendicular to the grating surface. This grating diffracts the light in different directions according to the wavelength. The relation of the diffraction angle, α, and the wavelength, λ, is represented by the Equation (3-1):

$$\alpha = \sin^{-1} \lambda f_c, \qquad (3\text{-}1)$$

where f_c is the compensation grating frequency. The +1 and the -1 diffraction orders from the compensation grating are reflected by the optical mirrors and intersect at the surface of the specimen. A fringe pattern is thus formed. The incidence angle of the beams, θ, happens to be equal to the diffraction angle, α. The sensitivity s is thus calculated by the Equation (3-2):

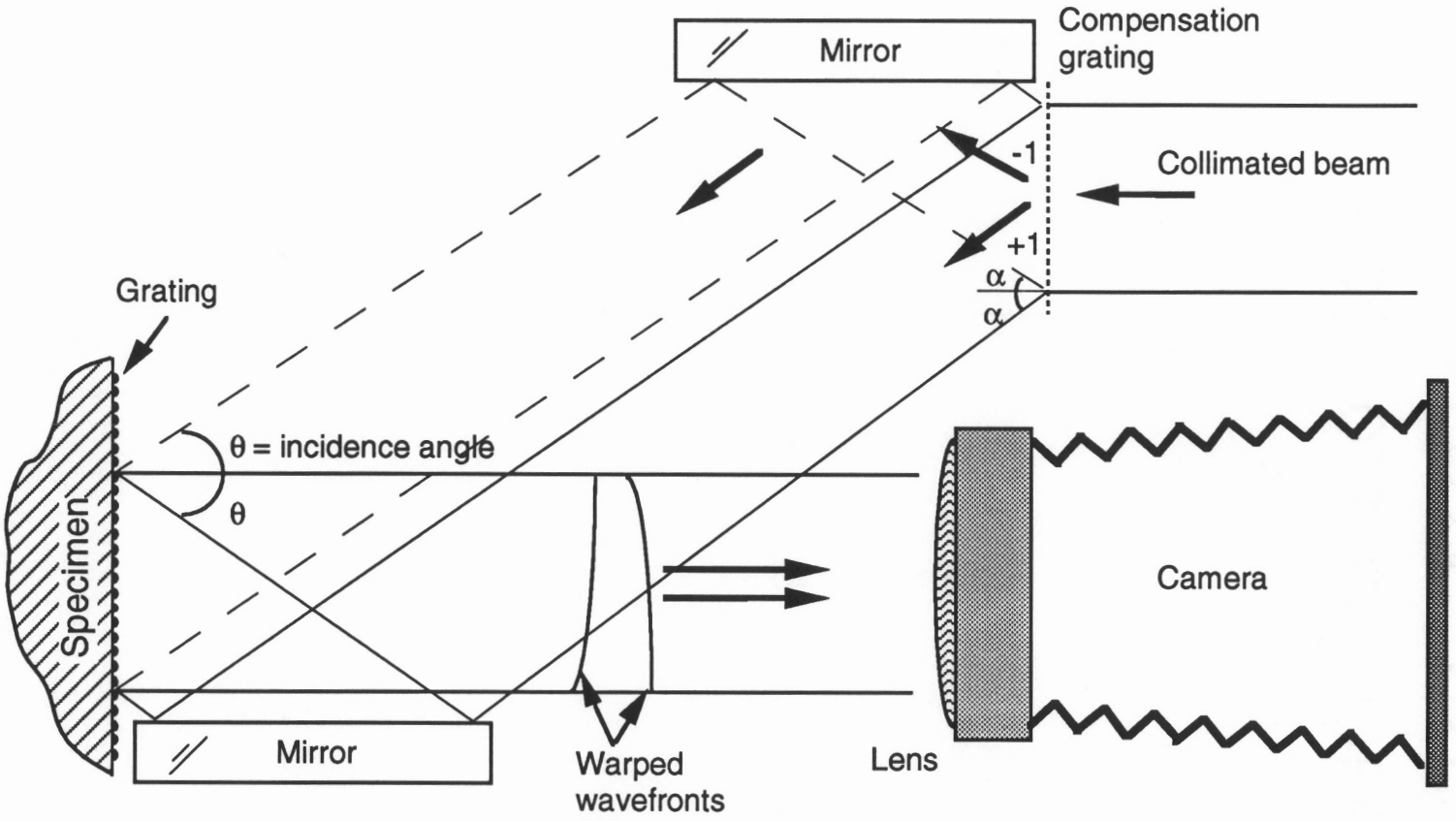

Figure 3.3 Achromatic moiré interferometer

$$s = \frac{l}{2\sin\theta} = \frac{1}{2f_c}. \qquad (3\text{-}2)$$

The equation (3-2) proves that the sensitivity of the achromatic system is independent of the wavelength, but depends on the frequency of the compensation grating only. Therefore, this system can use a broad-band light source, like a laser diode. However, a light source with a long coherent length, like a laser, is the easiest for the system tuning.

The misalignment of the illuminating beam has no effect on the fringe patterns, as was proved in [13]. The optical components (mirrors, compensation grating) are fixed together to minimize the relative motion caused by the vibration. If the optical components are attached to the testing equipment and vibrate with the specimen, the vibration sensitivity can be reduced to a minimum. For two-dimensional measurement, two sets of the optical components shown in the Figure 3.3 are arranged perpendicularly to each other, as shown in Figure 3.4. A cross specimen grating is also required.

3-2 Moiré Pattern Analysis

The sensitivity of a moiré system depends on the wavelength of the light used and on the arrangement of optical components, as shown in Equation (3-2). Let N_x and N_y represent the fringe orders of

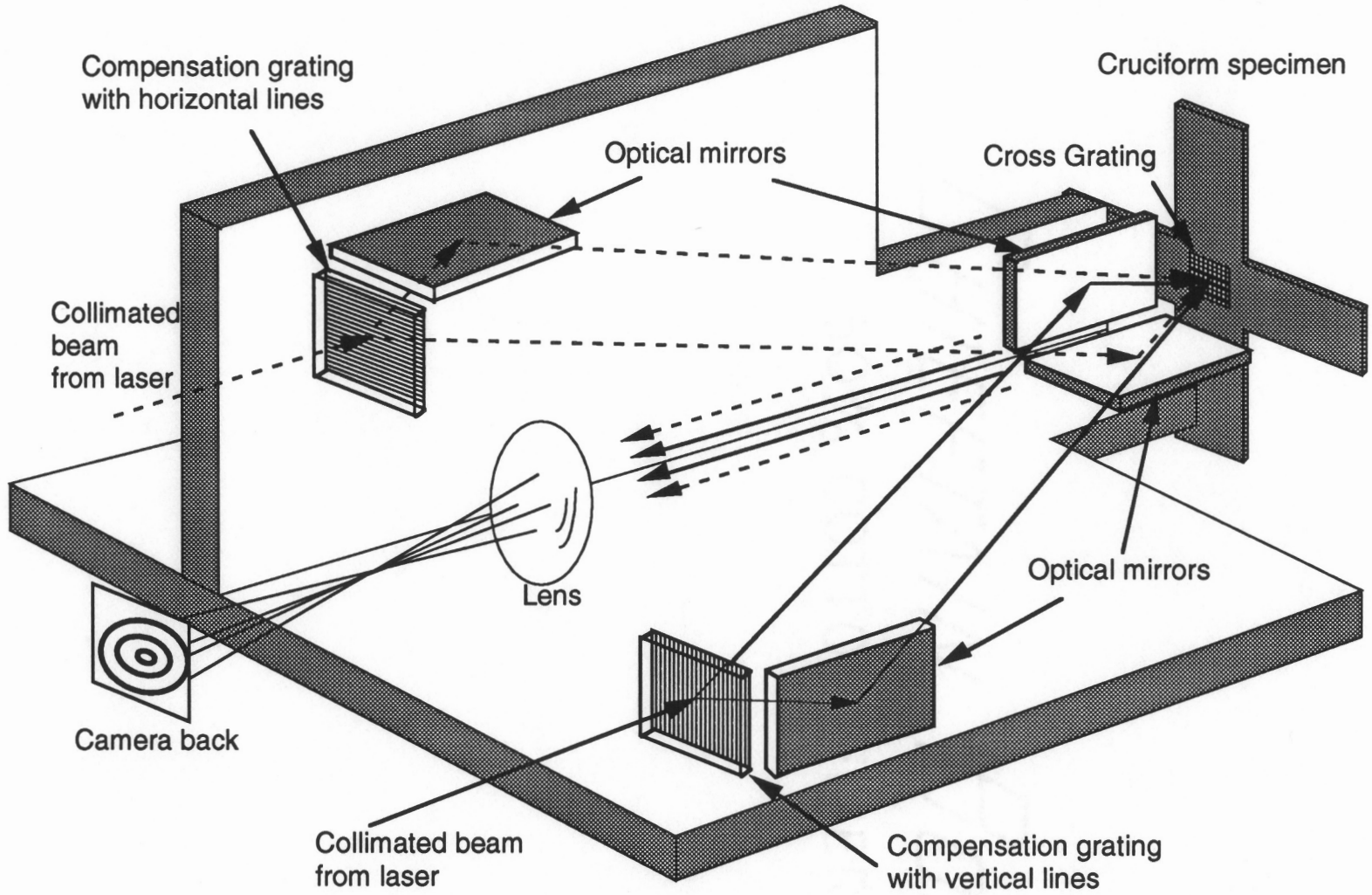

Figure 3.4 Achromatic moiré interferometer for two-dimensional applications

the U and V displacement patterns, respectively. The displacements relative to the zeroth fringe order at any point are expressed as the Equations (3-3a) and (3-3b) shown below:

$$U = \frac{\lambda}{2\sin\theta} N_x = s\, N_x, \tag{3-3a}$$

$$V = \frac{\lambda}{2\sin\theta} N_y = s\, N_y. \tag{3-3b}$$

The normal and shear strains are then calculated from the following strain-displacement relations:

$$\varepsilon_x = \frac{\partial U}{\partial x} = s\, \frac{\partial N_x}{\partial x}, \tag{3-4a}$$

$$\varepsilon_y = \frac{\partial V}{\partial y} = s\, \frac{\partial N_y}{\partial y}, \tag{3-4b}$$

$$\gamma_{xy} = \frac{\partial U}{\partial y} + \frac{\partial V}{\partial x} = s\, [\, \frac{\partial N_x}{\partial y} + \frac{\partial N_y}{\partial x}\,]. \tag{3-4c}$$

3-3 Carrier Fringes

There are two types of carrier fringes, carrier fringes of rotation and carrier fringes of extension. Carrier fringes of rotation are introduced by rotating the specimen grating relative to the optical system. On the other hand, carrier fringes of extension are introduced by mismatching the grating frequency to the optical system arrangement. The geometric approach of analyzing the

carrier effects [9,23] is explained as follows. The methodology for the moiré interferometry is exactly the same.

Let a reference grating frequency be f, and a specimen grating frequency be f′. The pitches between grating lines are g and g′, respectively. The reference grating lines are assumed to be vertical, and the specimen grating lines have a small angle θ from the vertical, as shown in Figure 3-5. An arbitrary point P is located at (x, y) from the origin, O, where the fringe number is assumed to be zero. Relative to the reference grating, x can be expressed by the Equation (3-5):

$$x = k\,g, \tag{3-5}$$

where k is the number of reference grating lines between O and P. Similarly, x can also be expressed relative to the specimen grating as shown in Equation (3-6):

$$x = \frac{m\,g'}{\cos\theta} = y \tan\theta, \tag{3-6}$$

where m is the number of specimen grating lines from O to P. The number of fringes, N_x, formed by the grating mismatch can be expressed as $N_x = k - m$, where the subscript x indicates that the fringe pattern is related to the horizontal displacement field. Therefore, the fringe order at the point P is

$$N_x = \frac{x}{g} - \frac{x - y\tan\theta}{g'}\cos\theta, \tag{3-7}$$

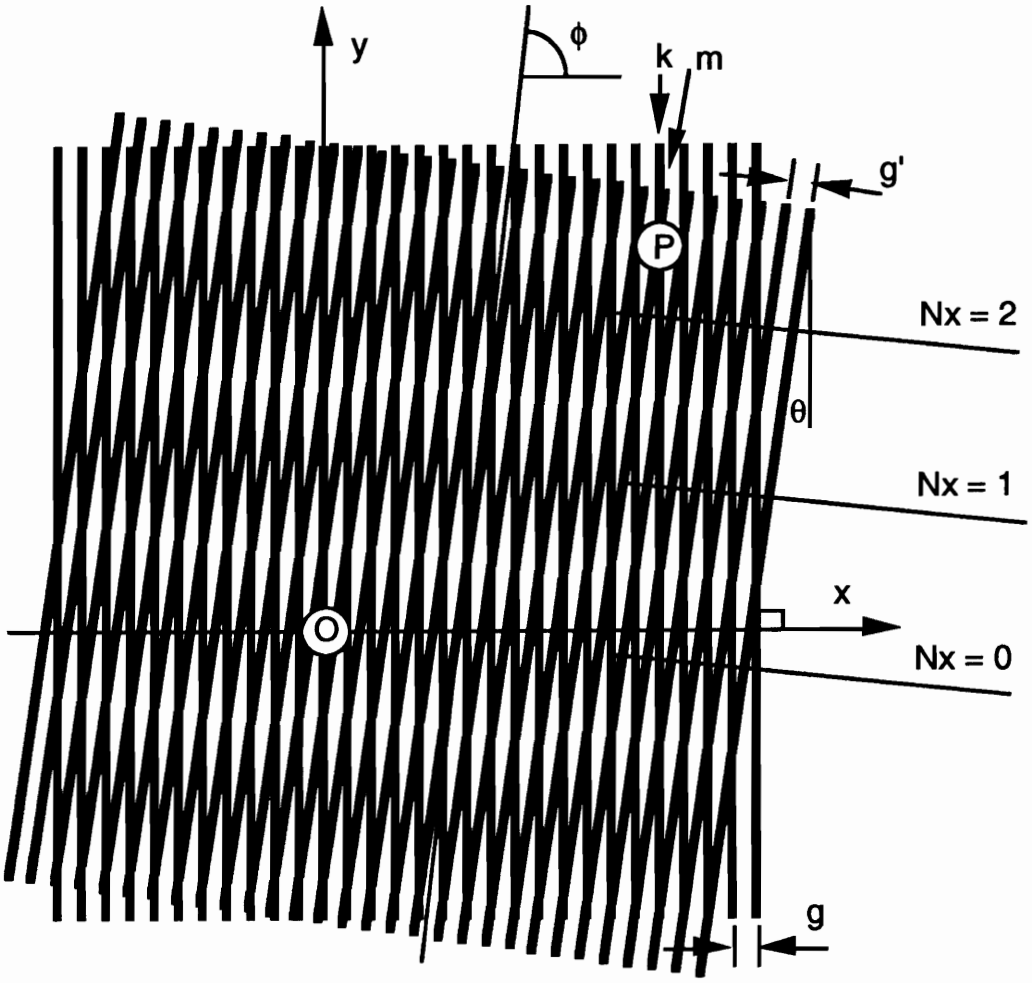

Figure 3.5 Geometric approach of moiré pattern analysis

or

$$N_x = f\,x - f'\,(x - y \tan\theta)\cos\theta. \qquad (3\text{-}8)$$

The direction of the fringe vector, ϕ, is expressed as shown in Equation (3-9).

$$\tan\phi = -\frac{g \sin\theta}{g' - g\cos\theta}. \qquad (3\text{-}9)$$

From Equation (3-8), the fringe number between O and P can be changed by changing the angle θ or the grating frequencies. The corresponding fringes are carrier of rotation and carrier of extension, respectively.

Consider the case that $f = f'$ and θ is small; the carrier of rotation frequency equals $f\theta$ per vertical unit length. The fringe vector direction ϕ is very close to 90°. That is, the carrier fringes of rotation are horizontal for the U-field. On the other hand, consider the angle $\theta = 0$, the carrier of extension frequency equals to $f - f'$ per horizontal unit length. The fringe vector direction ϕ is equal to 0°. The extensional fringes are vertical for the U-field. A similar approach can be applied to the vertical displacement field, whose reference grating lines are horizontal.

The effects of the carrier fringes on the strain components are evident. As we take the derivatives of the U-field, the horizontal-

fringe frequency indicates the change in the angle and virtually the shear strain component. On the other hand, the vertical-fringe frequency indicates the displacement per unit horizontal length and virtually the normal strain. That is, the effect of the carrier fringes is equal to adding a constant strain to the fringe pattern. The carrier of rotation adds equal but opposite amounts of strains, which will be automatically canceled, to two in-plane shear components, and the carrier of extension adds normal strain. The carrier fringes can be easily removed by comparing the recreated contour map to the original pattern, or checking with the boundary conditions.

For the V-field, the effects of the carriers are similar. However, there is one thing that needs to be emphasized about the carrier of rotation. As Figure 3-6 has shown, the specimen is rotated. An arbitrary point P on the specimen is moved to its new position P′. The distance of P moved can be represented by two orthogonal components, -dx and dy. If the coordinate of the point P is (x, y), and the angle of rotation is small, the following relationship exists.

$$\frac{dx}{y} = -\frac{dy}{x}. \qquad (3\text{-}10)$$

That is, the effects of the rotational carrier fringes are positive on one displacement field while negative on the other. Since the rotational amount is the same for both fields, the shear strain value

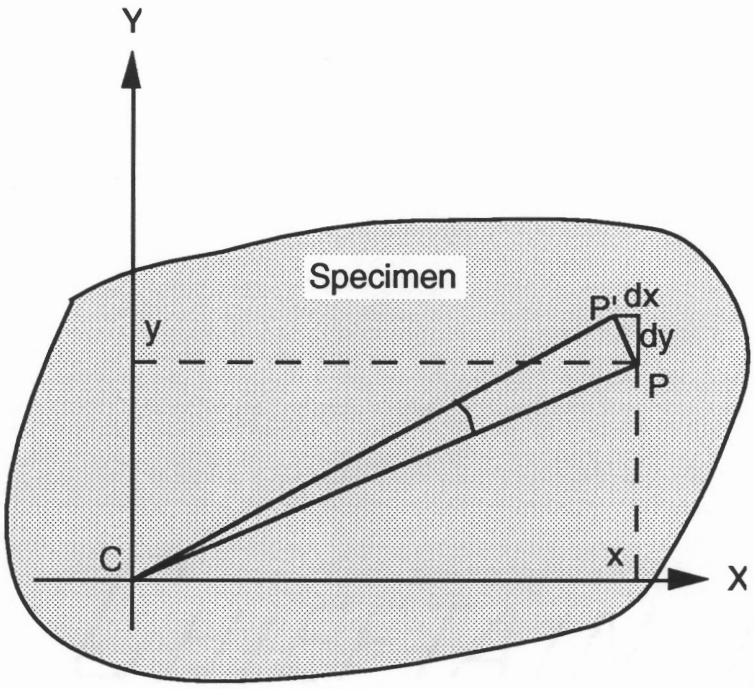

Figure 3.6 The effects of the carrier fringes of rotation

is automatically compensated. For this reason, the carrier of rotation is preferred over the carrier of extension if any carrier is needed.

3-4 Grating Replication Process

The grating replication process [11] is shown in Figure 3.7. A holographic plate is exposed to two interfering beams of light. The constructive and destructive interferences form a series of sinusoidal distribution of intensity. Then the plate is developed, and the unexposed emulsion shrinks, creating a linear phase diffraction grating. After being treated with a release agent, the grating mold is vacuum deposited with a thin layer of metal (aluminum usually). The mold is then cemented to the specimen surface and separated after the cement is cured. A reflective phase grating is thus replicated on the specimen. If a cross grating is desired, the holographic plate needs to be exposed in two orthogonal directions. This can be done easily by double exposure.

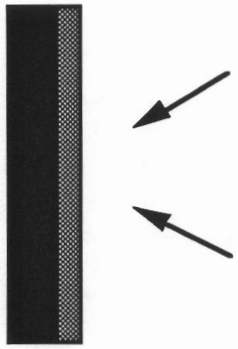

Exposure of a holographic plate to two interfering beams of light

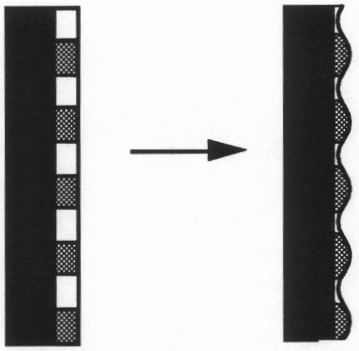

Development of the plate; unexposed emulsion shrinks creating a phase diffraction grating

Thin layer of metal is vacuum deposited on the grating surface treated with a parting agent. The mold is ready to be used.

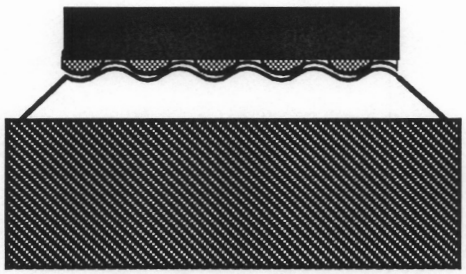

The mold is cemented to the specimen surface.

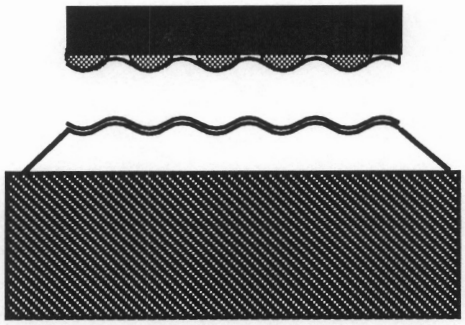

The mold is separated from the specimen. A reflective phase diffraction grating is replicated on the specimen surface.

Figure 3.7 Specimen grating replication process

4. HIGH-RESOLUTION DATA-REDUCTION TECHNIQUE AND NON-UNIFORM MESH GENERATION

Depending upon the frequency of a moiré pattern, the recording methods may vary. In cases of low frequency moiré patterns, it is a common practice to record them in a low contrast photographic process. The variation of the light intensity allows the fractional fringes to be obtained by means of the gray-level analysis. A video camera and a digital image processor are usually used in this process. In cases of high frequency moiré patterns, it is sufficient to record them in a high-contrast photographic process with strong overexposure. The data digitization is done right on the center of a fringe. Due to the limited resolution of a video camera relative to a photographic film camera, a photographic film is recommended for the high-frequency fringe-pattern recording.

To simplify the pattern recording process and analysis, a high-resolution data-reduction technique was developed by Czarnek and Lee [7, 8]. This technique uses the advantages of the high resolution of a photographic film and the high frequency of the carrier fringes. It allows moiré pattern to be digitized with high resolution, independently of the frequency of the original fringe pattern.

4-1 Fringe Pattern Recording

A low frequency moiré pattern is demonstrated in Figure 4.1. The specimen is a unidirectional composite with a cut on the left-

Figure 4.1 The horizontal displacement pattern of a graphite-PEEK unidirectional composite specimen with a cut on the left-hand side of the specimen to release the residual stresses. Fibers are perpendicular to the test surface. Low contrast photographic process was used.

hand side of the specimen to release the elastic residual stresses. This pattern represents a horizontal displacement field and was taken with normal exposure. A low contrast photographic process was used. Unless an image processor was used to perform the gray-level analysis, the resolution of the data digitization would be about 1/4 of a fringe order. The same pattern was photographed with high-contrast process and overexposure, as shown in Figure 4.2. The black fringes were much thinner than the white ones. The resolution at the centers of black fringes was enhanced. However, the data-point selection was still limited if the center of a fringe were to be digitized only. Therefore, the carrier fringes were introduced and photographed again with a high-contrast process and overexposure, as shown in Figure 4.3. This pattern included the carrier pattern of rotation. Due to increase in the fringe frequency, the selection of the data points was much more flexible. The carrier fringes of rotation could be removed later in the numerical process, but the high-resolution quality was maintained. Therefore, even for low frequency fringe patterns, the resolution of a displacement measurement could be enhanced by using this high-resolution data-reduction technique.

4-2 Non-Uniform-Mesh Generator

The non-uniform-mesh generator was developed by Lee and Czarnek and further modified by the author. It is a computer program written in Quick Basic on a Macintosh computer. As Lee and

Figure 4.2 The horizontal displacement pattern of the graphite-PEEK composite specimen. High-contrast photographic process was used. The black fringes are much thinner than the white ones.

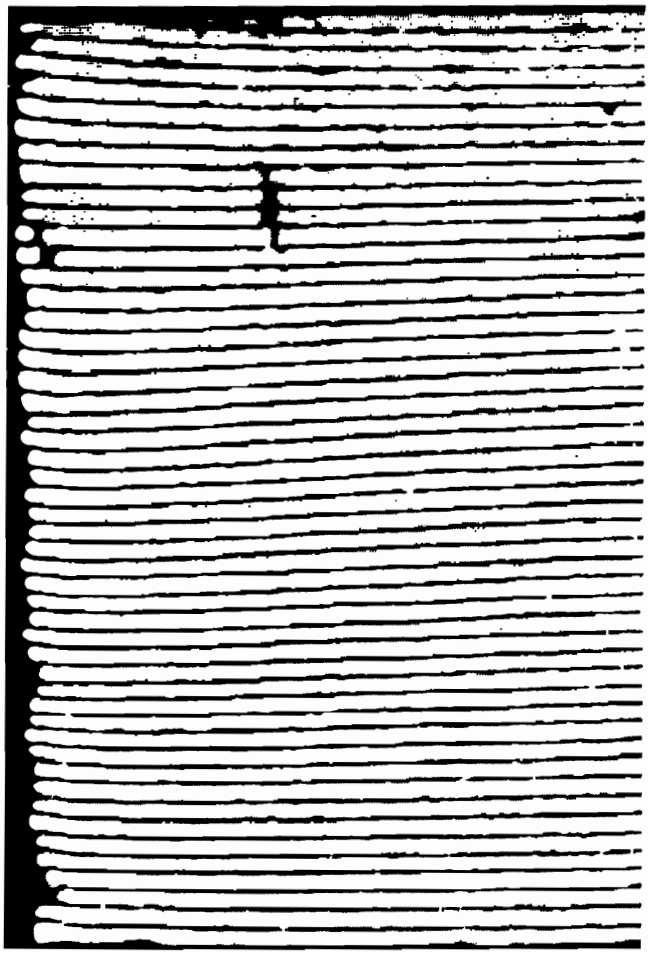

Figure 4.3 The horizontal displacement pattern of the graphite-PEEK composite specimen. High-contrast photographic process and carrier fringes of rotation were used.

Czarnek developed it, the program can automatically generate an all-triangular finite-element mesh, as shown in Figure 4.4, using the coordinates of the digitized points. This mesh was used to recreate the displacement patterns with high resolution by linear interpolation, as shown in Figure 4.5. As the finite element analysis was required for moiré pattern analysis, some interfacing modules were added by the author. According to the mesh generated, the same mesh, along with the boundary conditions, can be processed into a text file that is needed for FEM. The following FEM packages, PATRAN, ABAQUS, and FE77 were successfully interfaced. The results can also be processed by a different module in the program. The strain, or even stress, contours can be easily plotted.

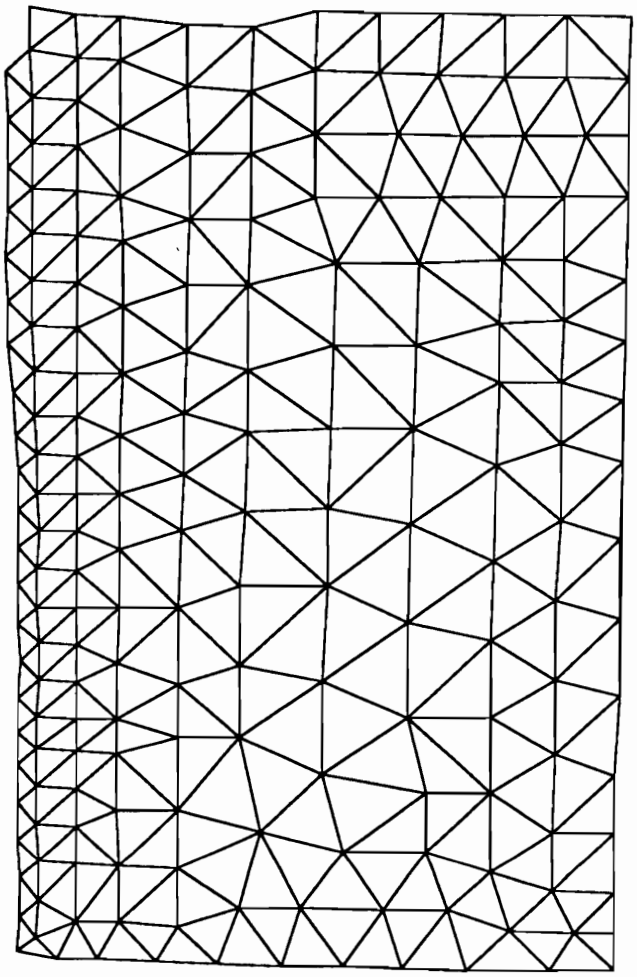

Figure 4.4 The non-uniform mesh created according to the coordinates of the digitized points.

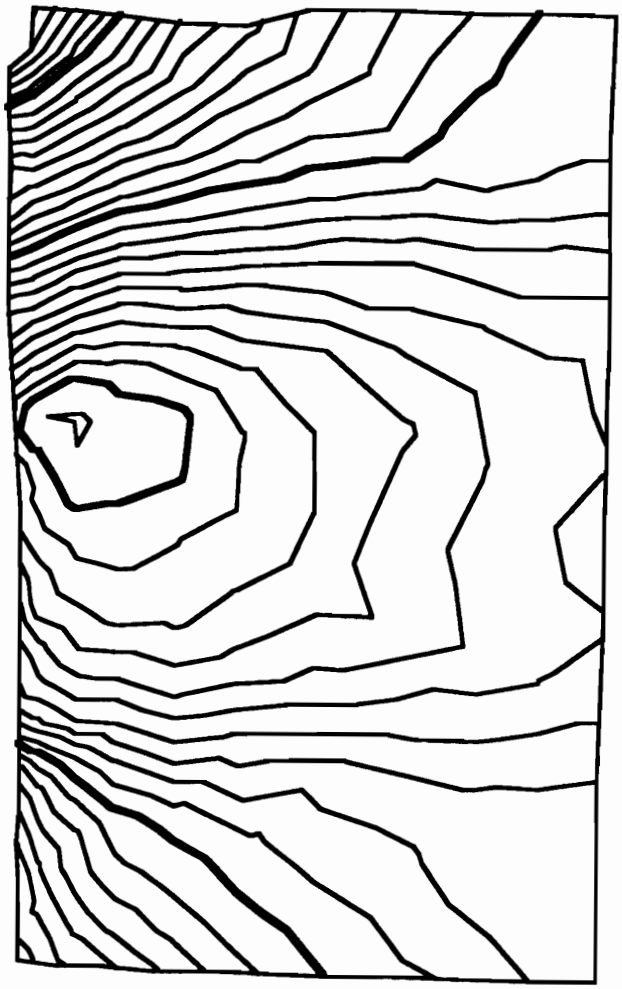

Figure 4.5 Digitally recreated displacement contour. The thick contours match the fringes in the picture. The thin contours are fractional, with fringe interval equal to 42 nm.

5 MODIFIED FINITE-ELEMENT MODEL FOR THE FULL-FIELD DATA SMOOTHING

The sensitivity of the moiré interferometry is high. In practice, a 417 nm per fringe order sensitivity is commonly used. The resolution of the high-resolution data-reduction technique is ± 20 nm. Despite the fact that the sensitivity and the resolution are high, there are some situations in which the moiré data need improvement, especially in taking derivatives (strains in this case) out of a pattern with only a few fringes. The examples include residual strain measurement, high-stiffness material test, and small area of interest.

If the strains are calculated with the use of the finite difference approach, $\varepsilon = \frac{\Delta U}{\Delta x}$, which is a common practice. The error of the derivatives is much higher than that of the original data. In fact, the error increases with the density of the collected data points. Therefore, data-smoothing schemes are widely used to minimize the error. A one-dimensional data-smoothing model [24] including a beam resting on a series of springs has been successful. To maintain the full-field nature of the moiré data, a two-dimensional data smoothing scheme is required. The previous model is modified into a two-dimensional FEM data-smoothing model. The advantage of using this two-dimensional model is that it makes it

possible to include the data smoothing and moiré data analysis in one easy step.

5-1 One-Dimensional Data Smoothing

There are many one-dimensional data-smoothing schemes in the field of numerical analysis. Engelstad [24] considered a beam resting on a series of linear springs attached to a deformable foundation, as shown in Figure 5.1(a). The experimental data were applied as the foundation settlement at the nodal points. If the beam had a zero stiffness, the contour of the beam would follow exactly the contour of the foundation, as shown in Figure 5.1(b). Consequently, the slopes of the beam at nodal points would not be continuous (multi-valued). If the stiffness of the beam were increased, it would bend according to how much moment it sustained due to the foundation settlement. The contour of the beam would be a smooth curve. The scattering of the data specified at the foundation would be eliminated, as shown in Figure 5.1(c). Most importantly, the slopes at the nodes would be continuous and single valued. Appropriate smoothing could be found by optimizing the ratio of the beam stiffness and the spring constant. However, if the beam stiffness went to infinity compared to the spring constant, the beam would remain flat, as shown in Figure 5.1(d). This approach is equivalent to a cubic-spline data-smoothing method, since the deflection of the beam has its third derivative (the shear force) as a step function.

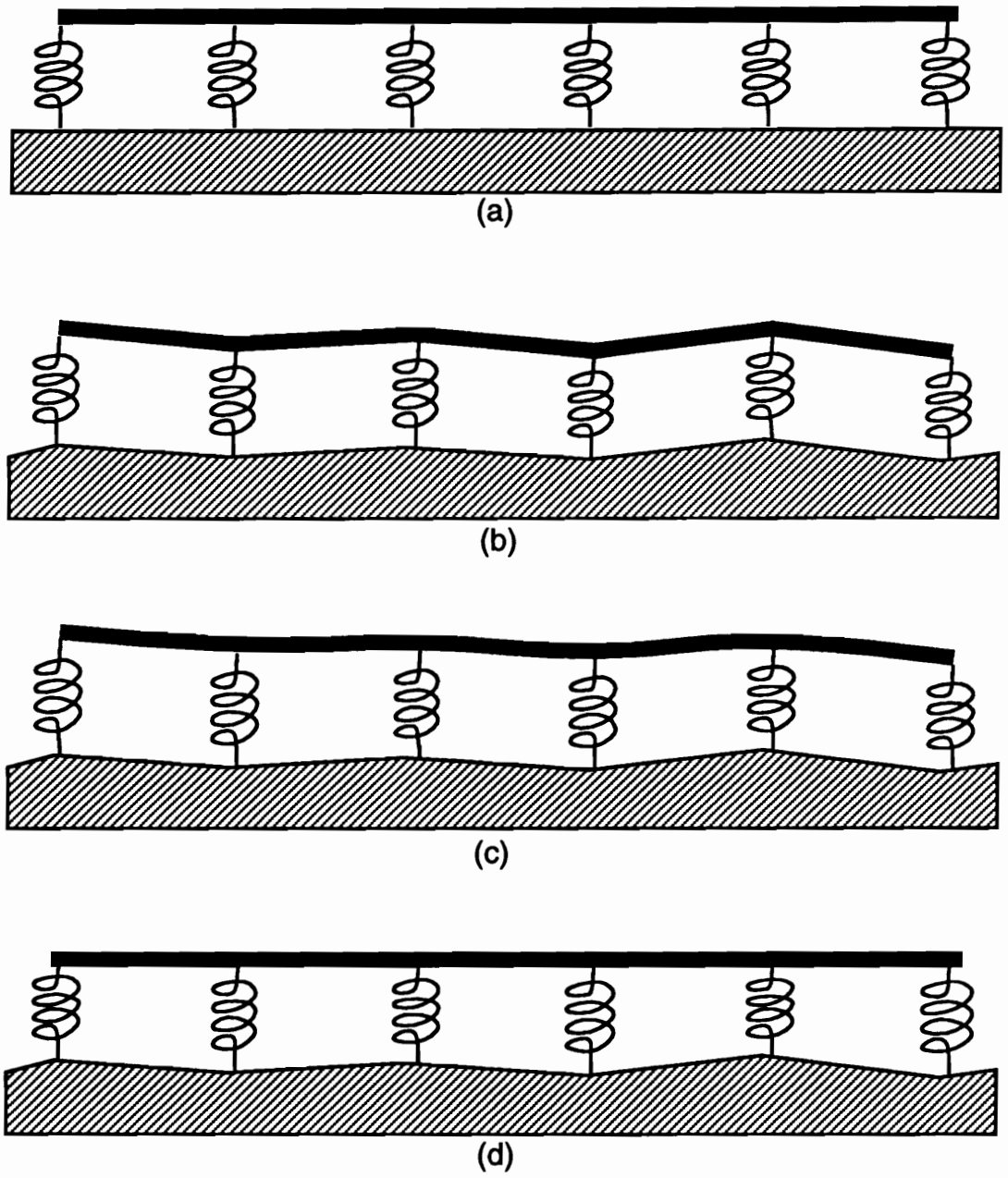

Figure 5-1 One-dimensional data-smoothing model; (a) a beam on a series of springs attached to a foundation; (b) a zero stiffness beam and a deformed foundation; (c) appropriately smoothed model; (d) a beam with infinite stiffness

5-2 Two-Dimensional Data Smoothing

The one-dimensional model was extended into a two-dimensional data-smoothing FEM model, as shown in Figure 5.2. This model is a flat plate resting on a matrix of springs free at the other ends. The reason the two-dimensional model has springs free at one end instead of a foundation is that at each node we may not have matching data points for both fields. The free ends will not constrain the model where there are no boundary conditions provided. Therefore, two-displacement fields can be applied to the same mesh as two load cases.

Similarly to the one-dimensional model, if the plate has a zero stiffness, the surface contour of the plate will follow exactly the displacement data specified at the free ends of the springs. The slopes at the nodes will be neither continuous nor single-valued. If the stiffness of the plate is increased, the surface contour of the plate will be smoothed. The scattering of the original data will be reasonably eliminated. Most importantly, the slopes at the nodes will be continuous and single-valued. Appropriate smoothing could be found by optimizing the ratio of the plate stiffness and the spring constant. However, if the ratio goes to infinity, the plate will remain flat.

Only one out-of-plane displacement can be specified in the two-dimensional data-smoothing model, and there are two in-plane

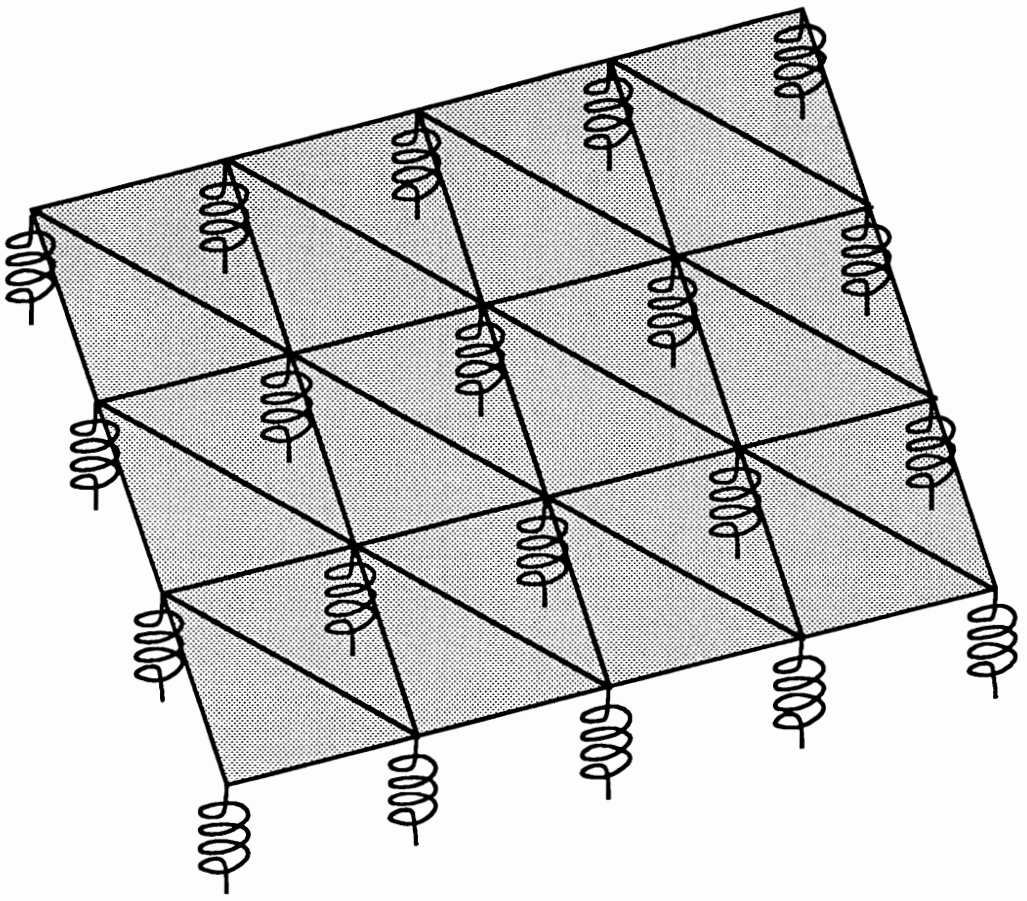

Figure 5-2 Two-dimensional data-smoothing model, a flat plate of triangular elements resting on a matrix of springs

displacement fields. The model needs to be run twice as two different load cases. Both results are then combined to obtain in-plane strain components.

5-3 Result Interpretation

Since the in-plane data are applied as the out-of-plane displacement, the FEM results are interpreted accordingly. The plate is assumed to be lying on the x-y plane, and the in-plane displacements U and V correspond to the x and y directions, respectively. The out-of-plane displacement of the FEM model is represented by W. The first load case uses the U data as W in the FEM model. Then the slopes of the plate are $\frac{\partial W}{\partial x}$ and $\frac{\partial W}{\partial y}$. They correspond to $\frac{\partial U}{\partial x}$ and $\frac{\partial U}{\partial y}$, respectively, where $\frac{\partial U}{\partial x}$ is the normal strain in x direction, and $\frac{\partial U}{\partial y}$ is part of the shear strain components. The second load case uses the V data as W in the FEM model. Similarly, $\frac{\partial W}{\partial x}$ and $\frac{\partial W}{\partial y}$ correspond to $\frac{\partial V}{\partial x}$ and $\frac{\partial V}{\partial y}$, respectively, where $\frac{\partial V}{\partial x}$ is another part of the shear strain components, and $\frac{\partial V}{\partial y}$ is the normal strain in the y direction. Therefore, if U-field data are used in the FEM model,

$$\frac{\partial W}{\partial x} = \frac{\partial U}{\partial x} = \varepsilon_x, \tag{5-1a}$$

$$\frac{\partial W}{\partial y} = \frac{\partial U}{\partial y}. \tag{5-1b}$$

If V-field data are used in the FEM model,

$$\frac{\partial W}{\partial x} = \frac{\partial V}{\partial x}, \tag{5-2a}$$

$$\frac{\partial W}{\partial y} = \frac{\partial V}{\partial y} = \varepsilon_y. \tag{5-2b}$$

The shear strain is obtained as the combination of the Equations (5-1b) and (5-2a). Thus,

$$\gamma_{xy} = \frac{\partial U}{\partial y} + \frac{\partial V}{\partial x} \ . \tag{5-3}$$

5-4 Criterion of Data Smoothing

To derive optimal results, the criterion of the data smoothing scheme needs to meet the nature of the data. From the high-resolution data-reduction technique, the scattering of the data will not exceed ±20 nm, which is the data resolution. Therefore, the criterion is set as limiting the difference between the smoothed results and the digitized data at every data point to be within ± 20 nm. The objective becomes finding the optimal ratio of plate stiffness and spring constant so that the surface contour is smoothed and the criterion is fulfilled. Thus, the derivatives of the displacement should contain minimum error.

6 ERROR EVALUATION OF THE FULL-FIELD HYBRID METHOD

There are some major factors affecting the accuracy of the method and they will be discussed in the following sections. An example is also presented for better understanding of the error.

6-1 Size of the Test Section and Density of the Data Points

The test section of a moiré experiment is usually less than a 50 mm by 50 mm area. Under the same level of strain, a large test section gives more mechanical fringes* than a small one. Even though higher magnification factor and carrier fringes are helpful for the case of a small test section, the resolution of the pattern is fixed. In general, the fewer mechanical fringes between two data points, the higher the percentage of the error will be. Also, the shorter the actual distance between two data points, the higher the error will become. According to finite difference method, the maximum error of high-sensitivity moiré interferometry data combined with high-resolution data-reduction technique without data smoothing is estimated as shown in Equation (6-1), where Δx is the actual distance between two data points:

---

* The mechanical fringes refer to the fringes caused by loading, temperature change, residual strain, etc. But exclude the carrier fringes of rotation and the carrier fringes of extension which are introduced by adjusting the optical components.

$$\Delta\varepsilon_{max} = \frac{2 \times 20nm}{\Delta x}. \qquad (6\text{-}1)$$

The maximum error indicated above suggested the boundary of error band without data smoothing. The denser the data points, the larger the error band will be. However, with data smoothing, the over-sampling effect reduces the error band if denser data points are used. Therefore, when a better result is needed, high-density data points are used. The example presented in section 6-9 will show the over-sampling effect.

6-2 Optical System Tuning

A well-tuned optical system is essential for a successful moiré test. Null patterns for both displacement fields are required. However, it is common that an initial moiré pattern contains a little non-uniformity. Usually the initial non-uniformity can be ignored. However, in a low-fringe-density situation, the error may be a concern. The best way to avoid too much non-uniformity is to use quality optics, tune the system precisely, and conduct the whole experiment in a constant-temperature environment. Another alternative is to subtract the initial pattern during the analytical process.

6-3 Optical Noise

The optical noise comes in the form of light intensity. If possible, the optical noise should be avoided. The high-resolution

data-reduction technique digitizes only the points of minimum intensity; therefore the optical noise effect is not critical. In addition, the optical noise can be manually avoided in the digitizing process.

6-4 Magnification Factor of the Picture

Higher magnification factors make it easier to locate the center of a fringe. In practice, a fringe pattern is usually enlarged to the size of about one full page of paper for easy handling. However, a high-enough magnification factor must be used to ensure high-resolution of the data.

6-5 Carrier Fringes

Even though they can be adjusted in the later process, carrier fringes of extension change the magnitude of the measured normal strains. The carrier fringes of rotation basically do not change the strain values. Therefore, carrier fringes of rotation are preferred and commonly used.

As discussed in the section 3-4, the fringe vector of the carrier fringes of rotation is not exactly at 90° for U-field. A tiny amount of normal strain is introduced by the carriers. Usually, the amount of rotation introduced is less than 0.5°, that corresponds to 21 fringe/mm if 1200 line/mm specimen grating is used with a fringe multiplication factor of 2. The direction of the fringe vector is 89.75°. Therefore, the normal strain introduced can be calculated

as shown in Equation (6-2). The value is negligible in most cases, and if it is not, it can be numerically considered:

$$21 \frac{\text{fringe}}{\text{mm}} \times 417\times10^{-6} \frac{\text{mm}}{\text{fringe}} \times \cos 89.75° = 0.38\times10^{-6}. \qquad (6\text{-}2)$$

In fact, the introduction of carrier fringes makes the high-resolution data-reduction technique applicable to low-fringe-density situations, and thus reduces the error. The carrier fringes also make data-point selection more flexible.

6-6 Resolution of the Digitizing Tablet

The resolution of the digitizing tablet used is 0.0254 mm. Compared to a typical picture size of 150 mm by 150 mm, a matrix of 6000 by 6000 point resolution is provided by the tablet. A maximum error is considered as half of the 0.0254 mm that corresponds to $\frac{1}{12000}$ of the total fringes on the picture. A pattern for digitization usually contains fewer than 100 fringes. Therefore, in the worst case, the maximum error on the fringe order is $\frac{100 \text{ fringe}}{12000}$ = 0.83% of a fringe = 3.5 nm. Compared to the 20 nm data-reduction resolution, the error due to the resolution of the digitizing tablet is negligible. Furthermore, a higher magnification factor can always be used to reduce this type of error.

6-7 Behavior of the Triangular Elements

The shape of the triangular elements affects the results of the FE analysis. In the non-uniform mesh generation program, acute

triangles are avoided. In the digitization process, well-distributed data points can also help in creating a well-behaved mesh.

6-8 Calculation Error

The round-off error during the FE analysis can be minimized by using double precision variables and well-organized matrix when the model is being solved. This type of error is usually ignored.

6-9 Data Smoothing

The data-smoothing scheme is supposed to reduce the scattering of the data, and thus reduce the error. The effect of the scheme really depends on how well the data are smoothed. When the smoothing criterion is satisfied, the smoothed displacement contours should fit the original pattern, and without scattering.

The following example demonstrates the effect of data smoothing with known displacement boundary conditions. The assumed test area is a 8mm by 8mm square. The center of the test area is the origin. The displacement fields are assumed as shown in Equations (6-3a) and (6-3b). The corresponding strain fields are as shown in Equations (6-4a) and (6-4b):

$$u = \frac{x^2}{16} \times 417\text{nm}, \qquad (6\text{-}3a)$$

$$v = \frac{y^2}{16} \times 417\text{nm}, \qquad (6\text{-}3b)$$

$$\varepsilon_x = \frac{x}{8} \times 417, \qquad (6\text{-}4a)$$

$$\varepsilon_y = \frac{y}{8} \times 417. \qquad (6\text{-}4b)$$

In the first case of the example, an 9×9 array of data points is entered with a random error within ± 20 nm of displacement. This 9×9 case is run twice, with and without data-smoothing scheme. The results along the x-axis is plotted as shown in Figure 6.1. The maximum error without data smoothing is 27×10^{-6}, while the maximum error with data smoothing is 22×10^{-6}. The average error drops from 9×10^{-6} to 7×10^{-6} if data smoothing scheme is used.

The second case uses a 17x17 array of data points instead. The horizontal strain contour is as shown in Figure 6.2. As mentioned in the section 6-1, the error band increases if the density of data points is increased. The contour already failed to show the correct distribution of the strain. On the other hand, the smoothed result is as shown in Figure 6.3, which is much closer to the accurate pattern defined by the Equations (6-4). The strain distributions along the x-axis are shown in the Figure 6.4. The smoothed result reduces the average error down to 5×10^{-6}, while the average error is increased to 12×10^{-6} without data smoothing. The maximum errors are reduced to 18×10^{-6} with data smoothing, and increased to 32×10^{-6} without data smoothing, respectively. That is, when a local disturbance of displacement pattern shows, a denser mesh can be used to enhance the accuracy of the strain data.

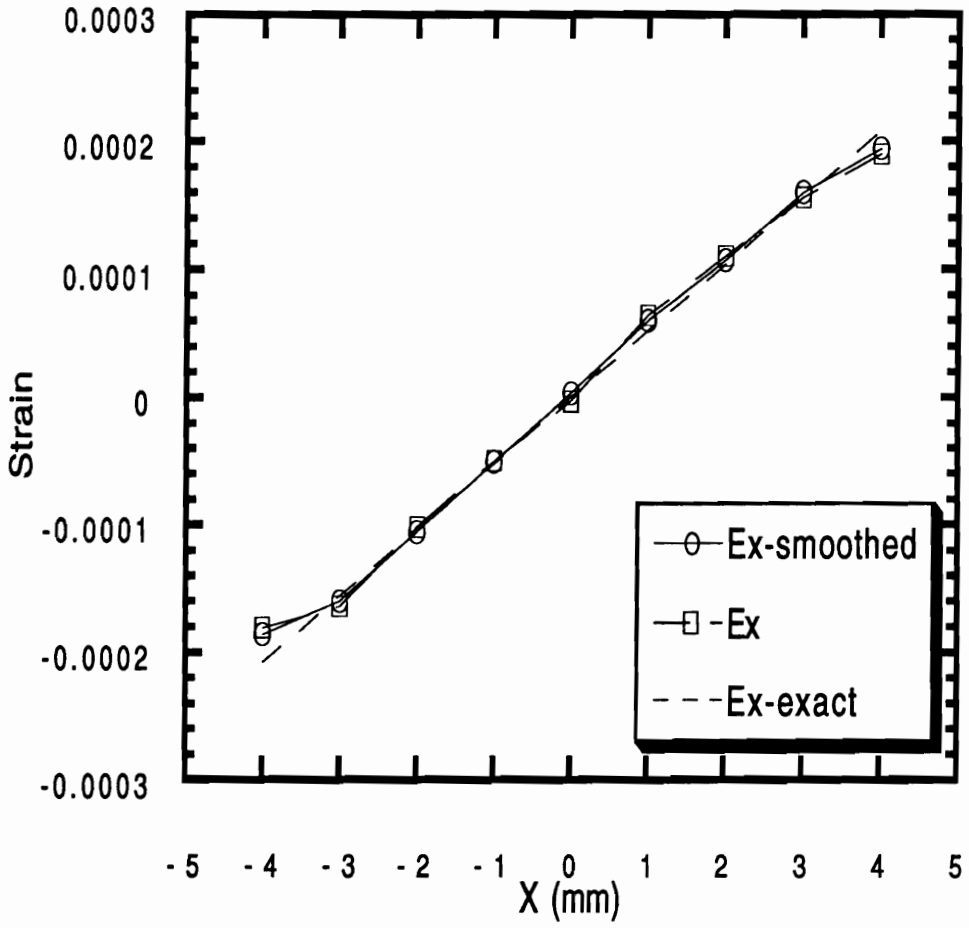

Figure 6.1 The strain distributions along the x-axis. An 9×9 array of data points is used. The average error with data smoothing (Ex-smoothed) is 7×10^{-6}; without data smoothing (Ex) is 9×10^{-6}. The maximum errors are 27×10^{-6} and 22×10^{-6}, respectively.

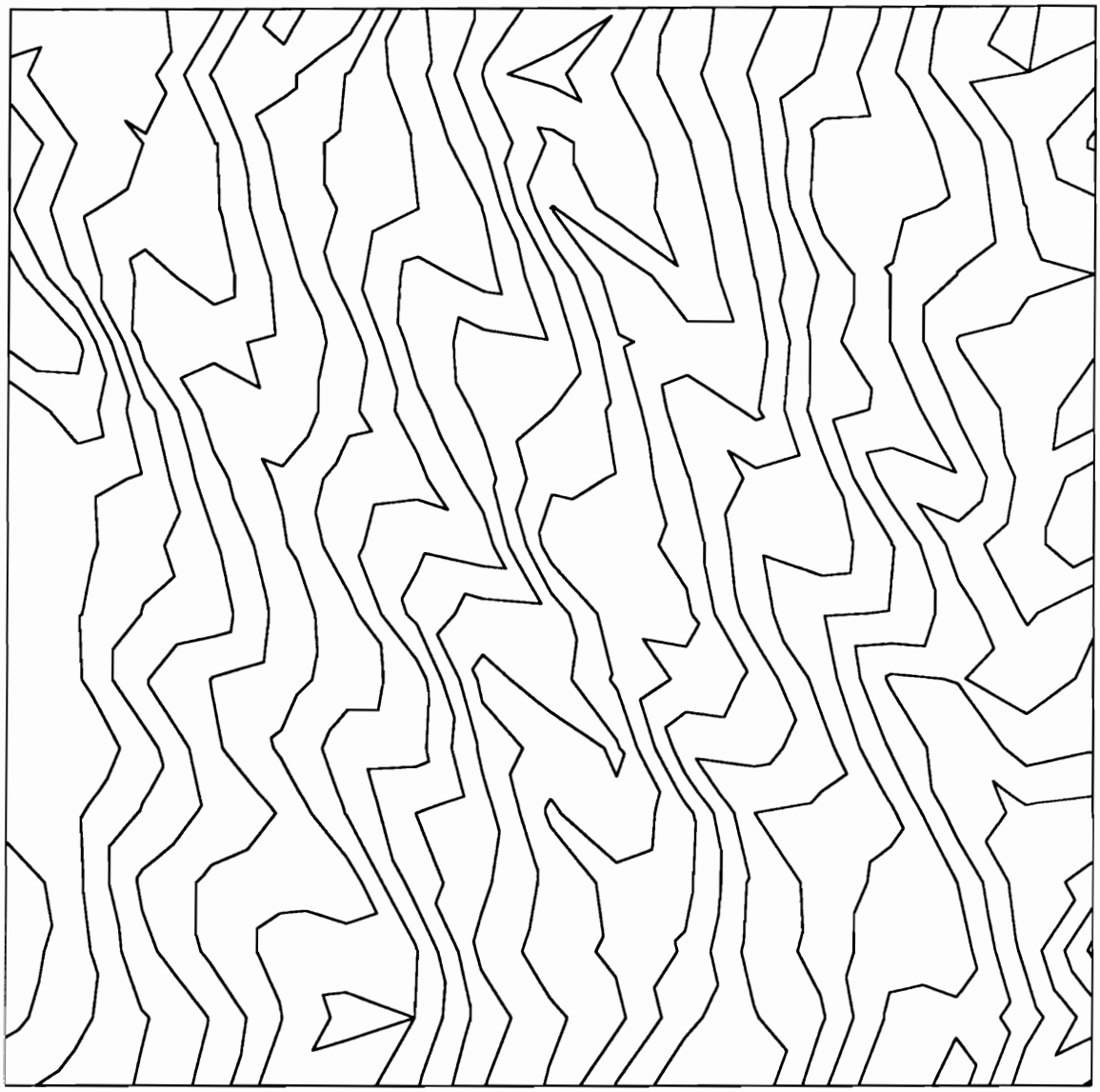

Figure 6.2 The strain contour without data smoothing. A 17x17 array of data points is used.

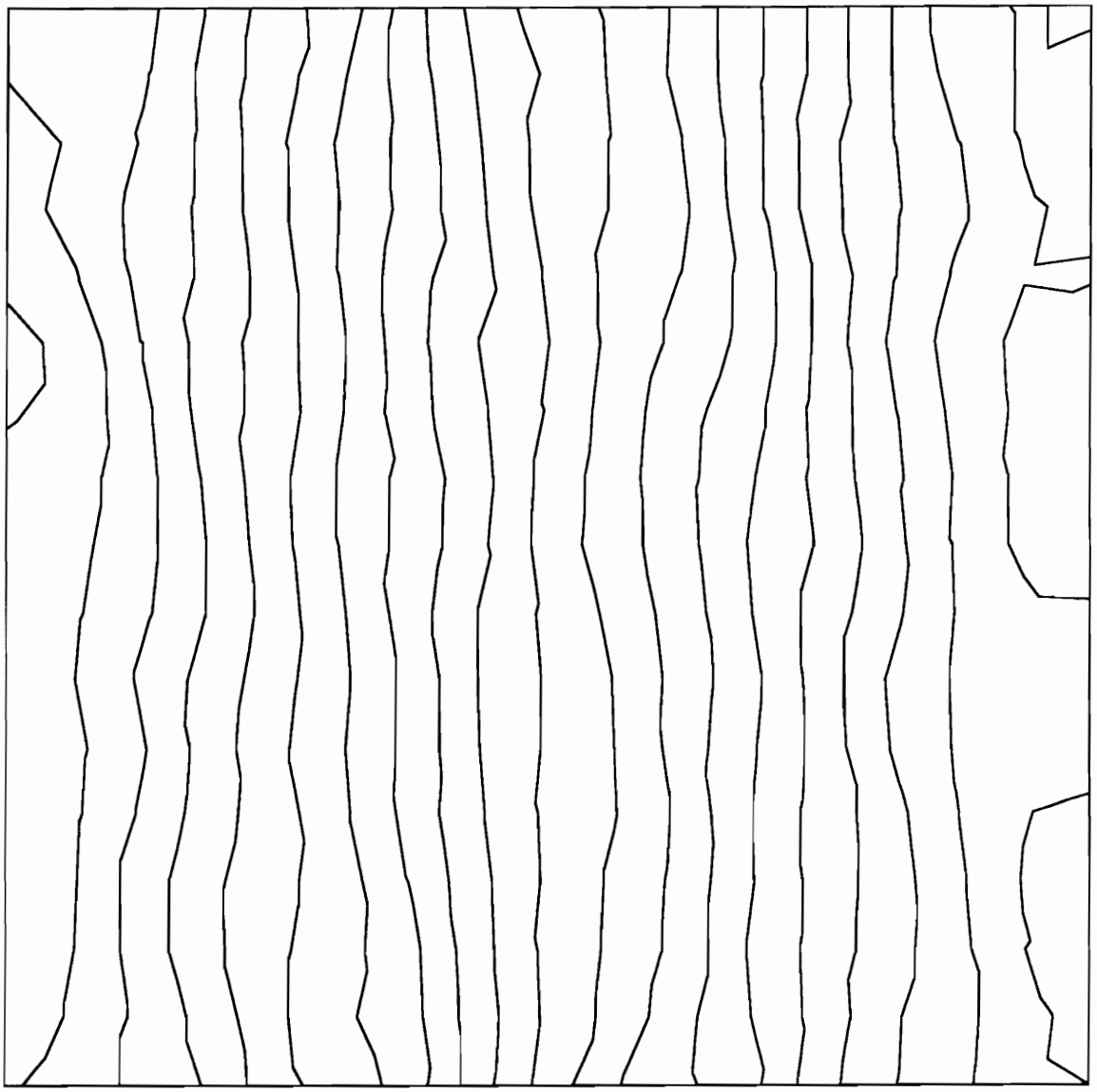

Figure 6.3 The strain contour with data smoothing. A 17x17 array of data points is used.

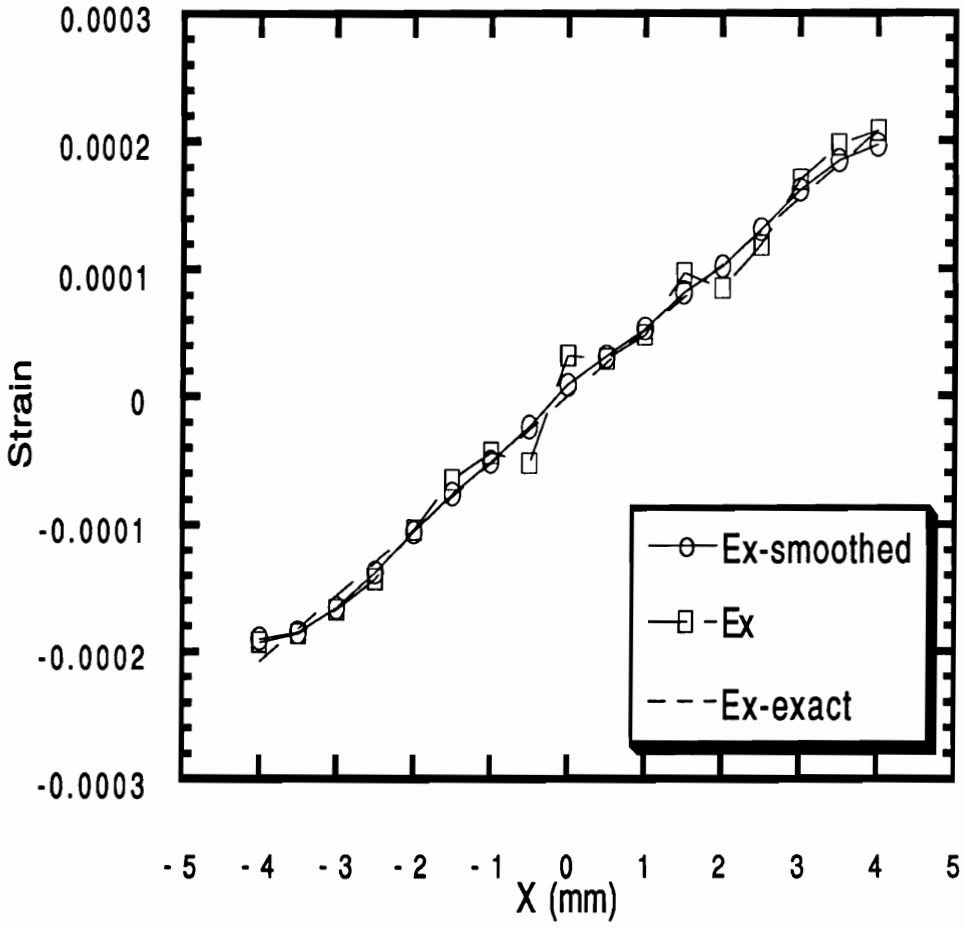

Figure 6.4 The strain distributions along the x-axis. A 17x17 array of data points is used. Without data smoothing (Ex), the average error is 12×10^{-6}; with data smoothing (Ex-smoothed), the average error is 5×10^{-6}. The maximum errors are 32×10^{-6} and 18×10^{-6} respectively.

6-10 Summary of Error Evaluation

Summarizing the previous discussion; most of the error sources are avoidable or negligible. The data resolution provides the limit of error at $\frac{2\times 20nm}{\Delta x}$, while the data-smoothing scheme reduces the amount of error and holds it small as the density of data points increases. This over-sampling effect allows detection of disturbance existing in the moiré patterns by increasing data points.

7 APPLICATION OF THE FULL-FIELD HYBRID METHOD - COMPOSITE RESIDUAL STRAIN MEASUREMENT

The full-field hybrid method was applied to a unidirectional graphite-PEEK composite residual test. The displacement contours from the moiré test contained only a few fringes. They are very difficult to analyze by means of the conventional method, but they constitute a very good example of the need for this full-field hybrid method.

7-1 Specimen and Testing Procedures

The composite specimen was a 16-ply unidirectional AS4 graphite-PEEK (also known as APC2) panel with fibers perpendicular to the test surface, as shown in Figure 7.1. The thickness of the specimen was 2.2 mm. A 1200 line/mm reflective grating was replicated on the edge of the specimen before the test. A three-mirror four-beam moiré interferometer was tuned to null patterns on both fields with the specimen. The sensitivity was set at 417 nm per fringe order. The specimen then was cut with a low-speed diamond saw to release the elastic residual strain and then put back to the interferometer. The photographic process was executed as the high-resolution data-reduction technique required. The right hand side of the cut was analyzed on an area of 1.2 mm by 2.2 mm.

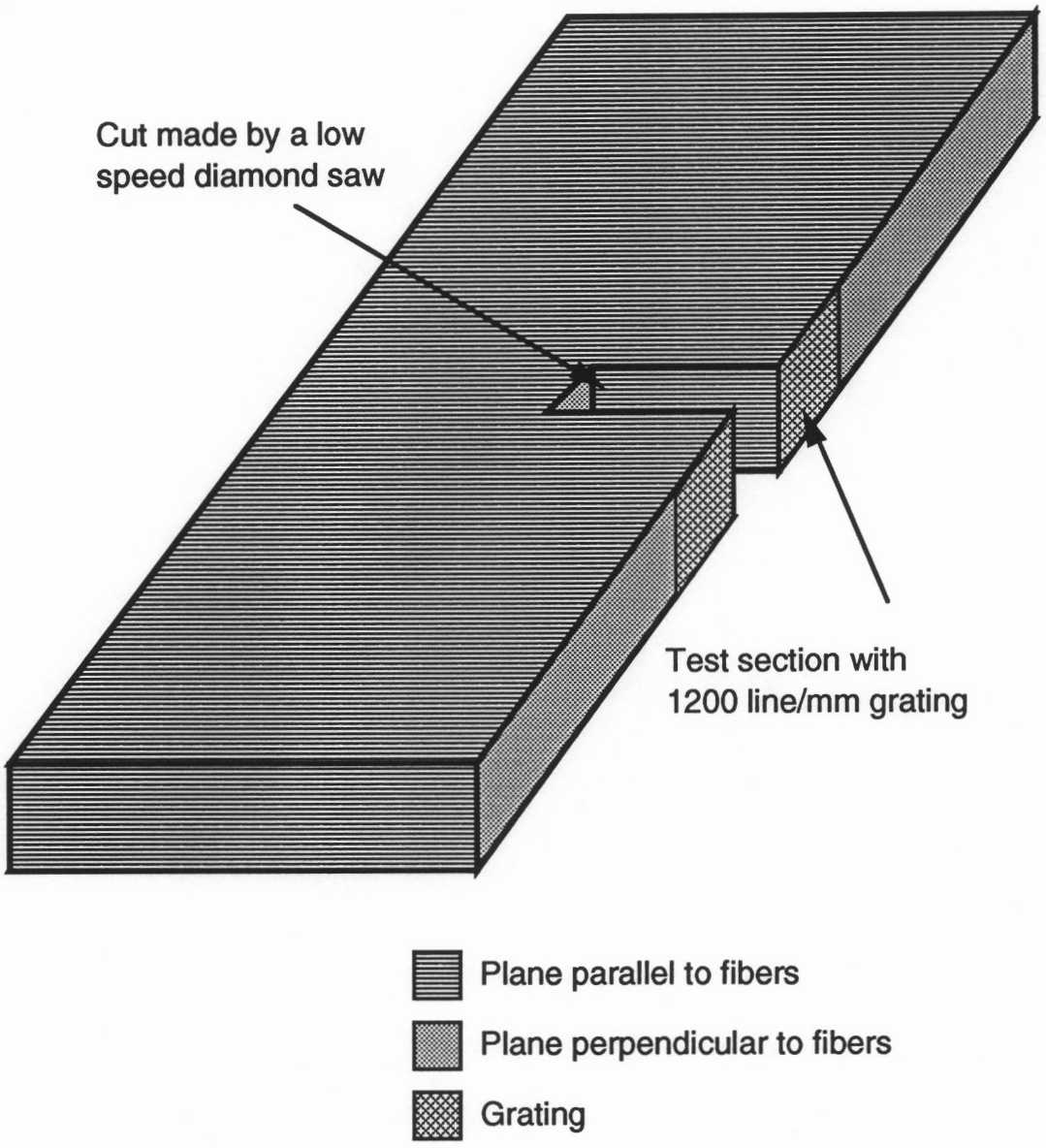

Figure 7.1 AS4 graphite-PEEK (APC2) composite residual test specimen with fibers perpendicular to the test surface. The thickness of the specimen was 2.2 mm.

7-2 Test Results

The horizontal (U) and the vertical (V) displacement fields of the residual test are shown in Figures 7.2(a) and (b). Because of low fringe density, the resolution of the traditional moiré-data interpretation (1/4 of a fringe order or 100 nm) was not enough. Therefore, another set of patterns was recorded with appropriate carrier fringes of rotation plus overexposure as shown in Figures 7.3(a) and (b). These patterns with carrier were digitized instead of the original patterns to enhance the resolution to $\pm$ 20 nm.

7-3 Numerical Process

The digitized data (coordinates of data points and their corresponding fringe numbers) were processed by the mesh generation program. A non-uniform mesh was created, as shown in Figure 4.4 on page 35. The next step in the numerical process was to remove the carrier fringes from the digitized data. The original fringe patterns were recreated digitally, as shown in Figures 7.4 and 7.5. The thick contours represent the original moiré fringes, and the thin contours are the fractional fringes. The contour intervals of original fringes and fractional fringes were 417 nm and 42 nm, respectively. In this step, we could also check if a mistake was made during the digitizing process by comparing the recreated contours to the original patterns. The data-smoothing scheme was not used here yet. Even though the patterns were very carefully digitized, some fluctuations could be seen on the contours.

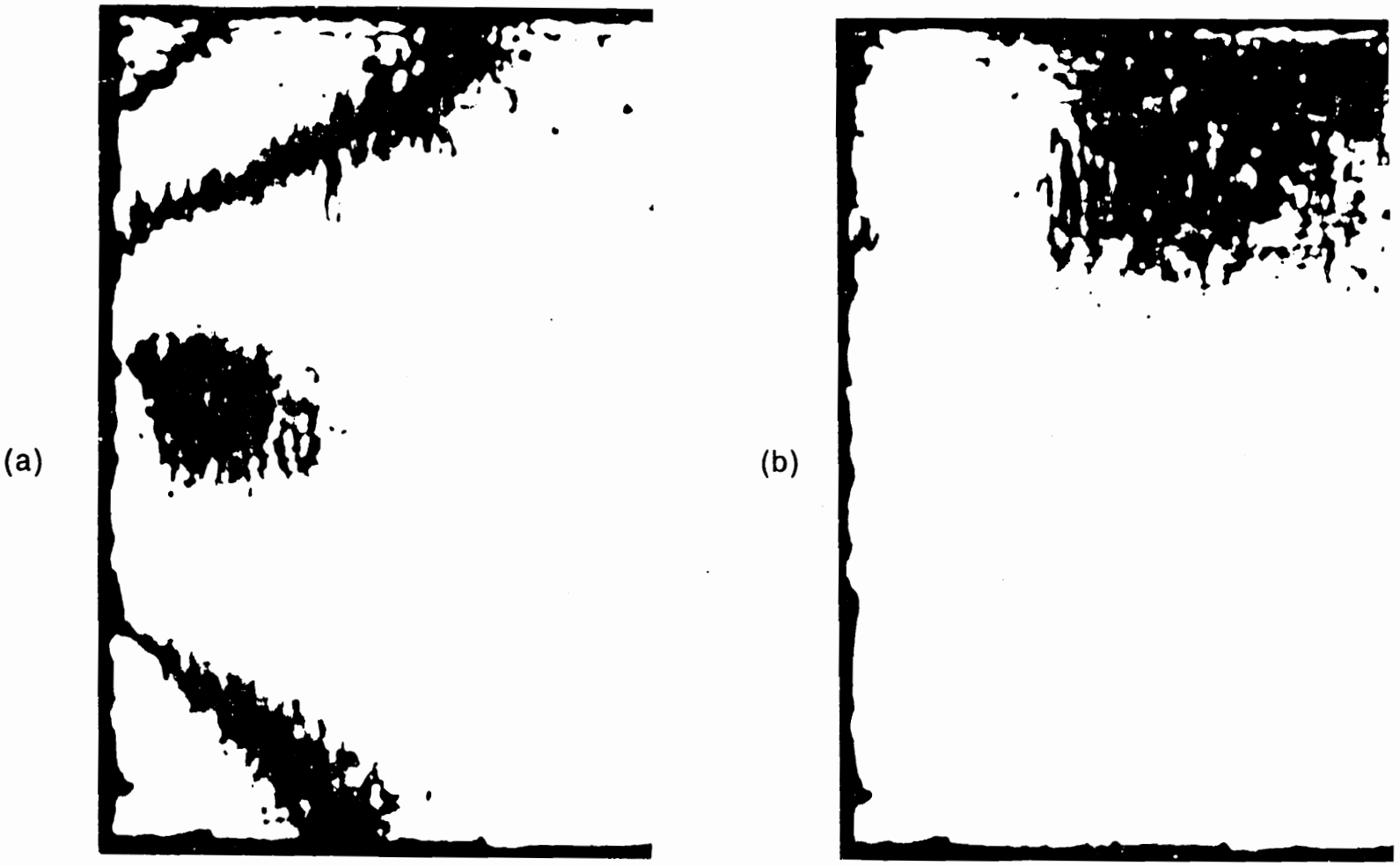

Figure 7.2 (a) Horizontal and (b) vertical displacement patterns of the composite residual strain test.

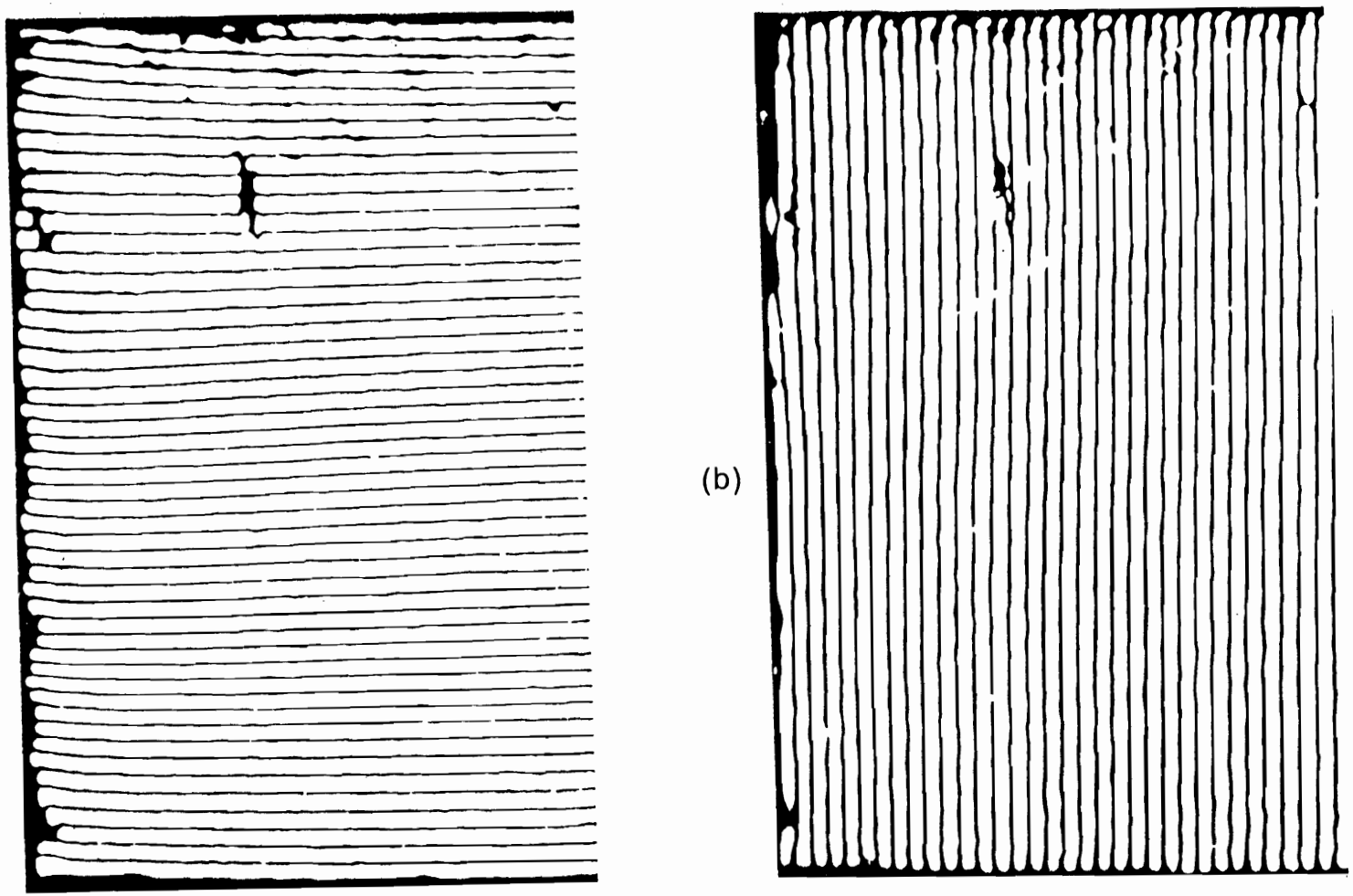

Figure 7.3 (a) Horizontal and (b) vertical displacement patterns of the composite residual strain test with carrier fringes of rotation and overexposure.

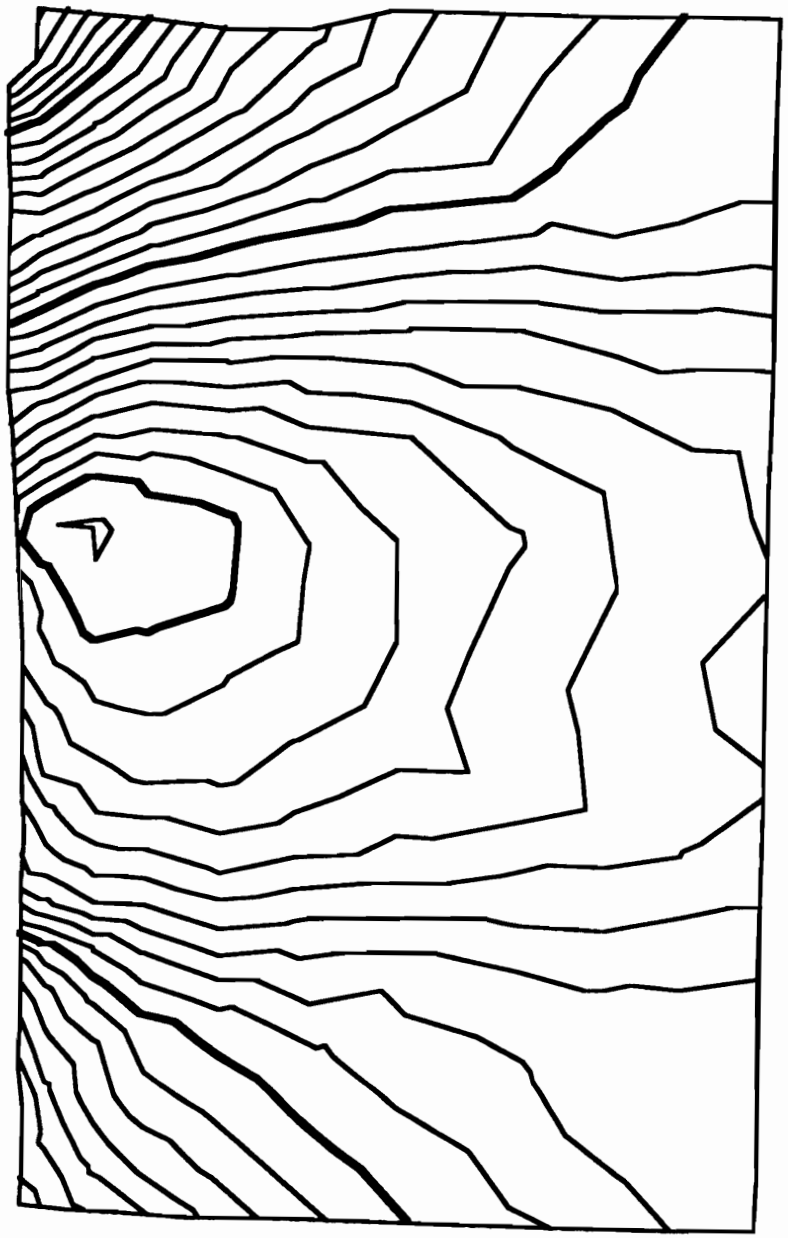

Figure 7.4 Digitally recreated U-field of the composite residual test. The thick contours represent the original fringes, and the thin contours represent fractional fringes. Contour intervals are 417 nm and 42 nm, respectively.

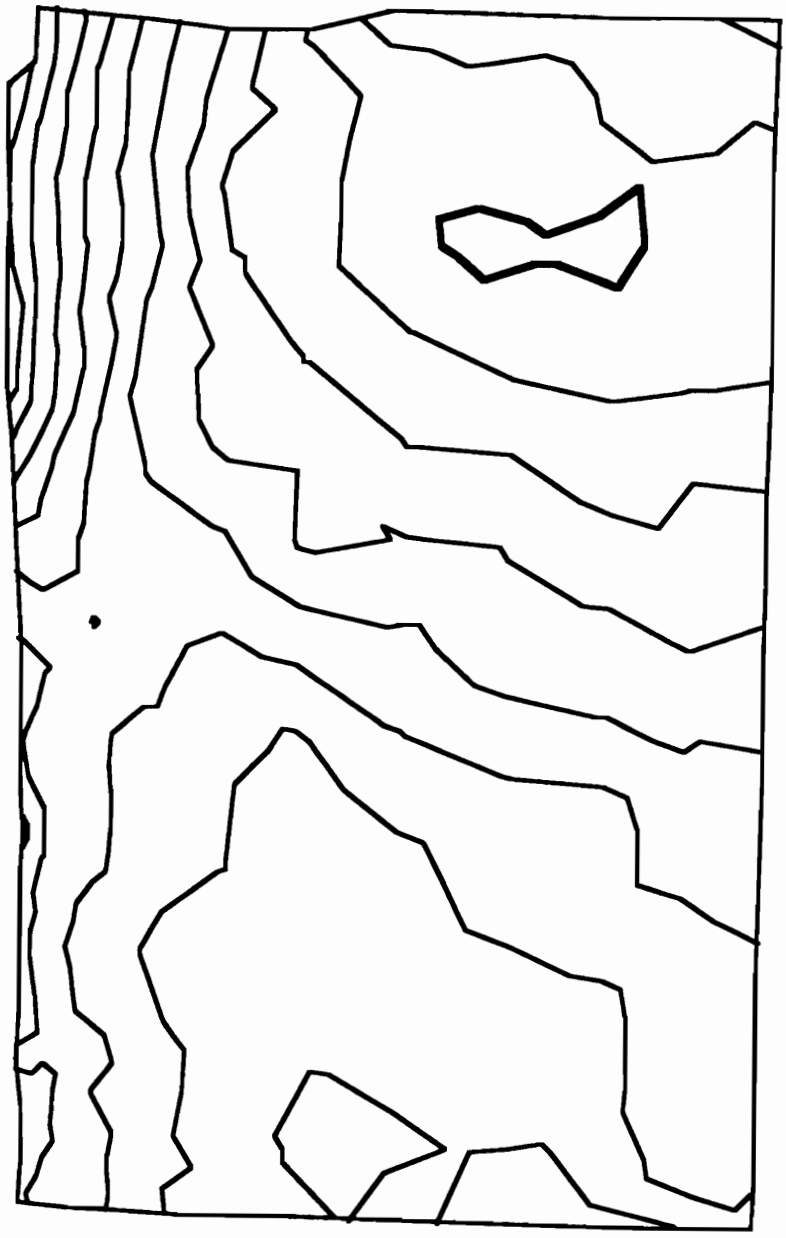

Figure 7.5 Digitally recreated V-field of the composite residual test. The thick contour represent the original fringe, and the thin contours represent fractional fringes. Contour intervals are 417 nm and 42 nm, respectively.

Before it can be analyzed by an FEM package, the mesh was modified into a data-smoothing model by the same program. Properly interfaced, a text file of instructions for the FEM package was run automatically. The results of FEM were checked to satisfy the smoothing criterion.

7-4 Data Smoothing and Results

The smoothed displacement contours are shown in Figures 7.6 and 7.7. The contour intervals were the same as the recreated contours in Figures 7.4 and 7.5. It was obvious that the smoothed results eliminated most of the scattering in the recreated patterns. Also, at any data point, the difference between two sets of contours did not exceed 20 nm. The smoothing criterion was satisfied.

Because residual stresses were released by cutting, the displacement patterns were reversed. Therefore, actual strain values should be opposite to the analytical results. The smoothed strain contours (ε_x, ε_y, and γ_{xy}) are shown in Figures 7.8, 7.9, and 7.10. The actual strains are also indicated. The contour interval was set at 100×10^{-6} for both normal strain contours and 200×10^{-6} for the shear strain contour. The ranges of strains were -1200×10^{-6} to 300×10^{-6} for ε_x, -400×10^{-6} to 500×10^{-6} for ε_y, and -2100×10^{-6} to 1600×10^{-6} for γ_{xy}.

For comparison, the same mesh without springs (i.e. without data smoothing) was analyzed. This time, both displacement fields

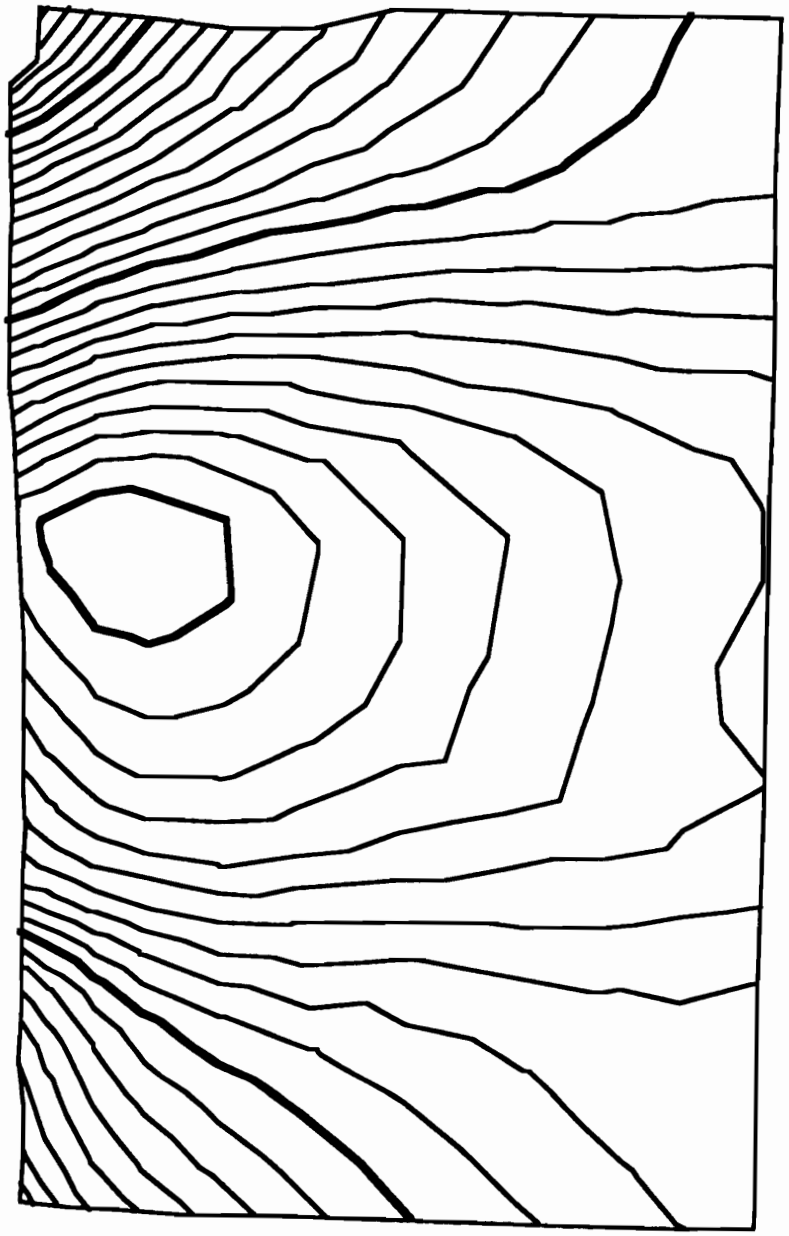

Figure 7.6 The smoothed U-displacement contour. The thick contours represent the original fringes, and the thin contours are the fractional fringes. The contour intervals are 417 nm and 42 nm, respectively.

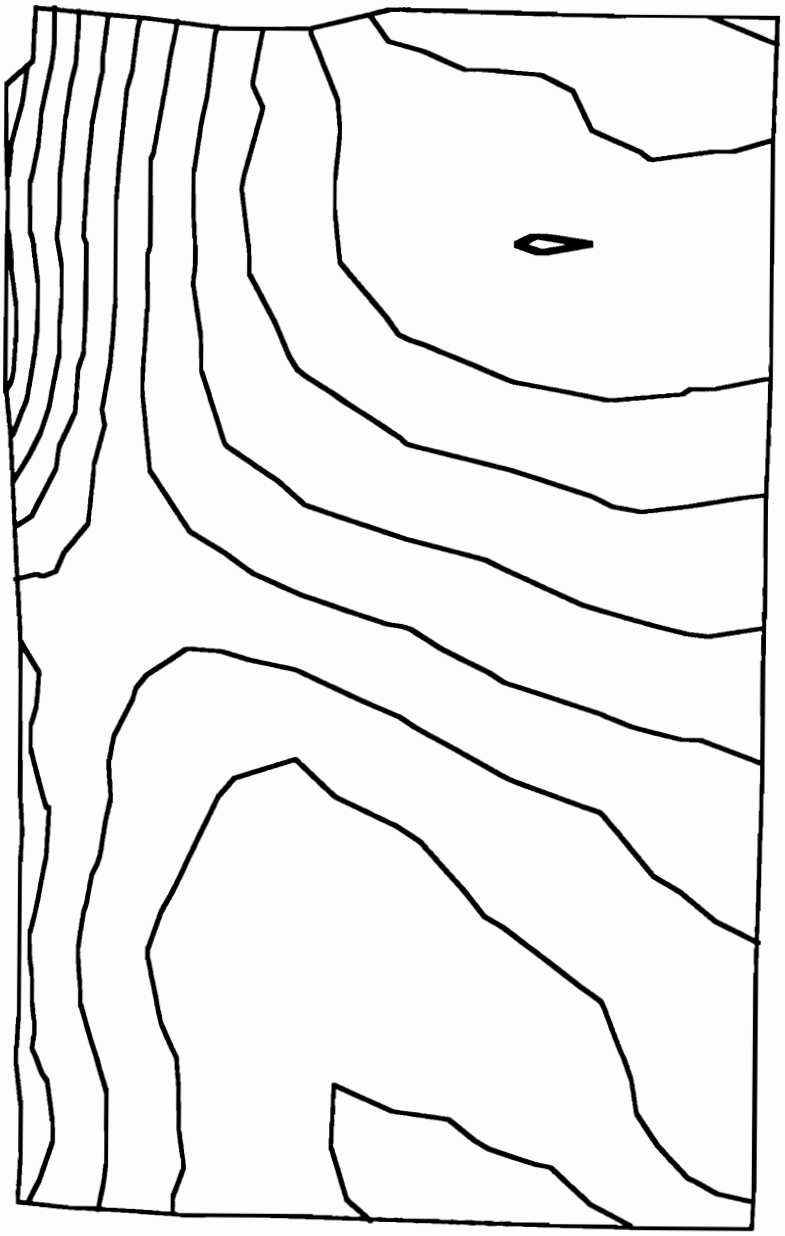

Figure 7.7 The smoothed V-displacement contour. The thick contours represent the original fringes, and the thin contours are the fractional fringes. The contour intervals are 417 nm and 42 nm respectively.

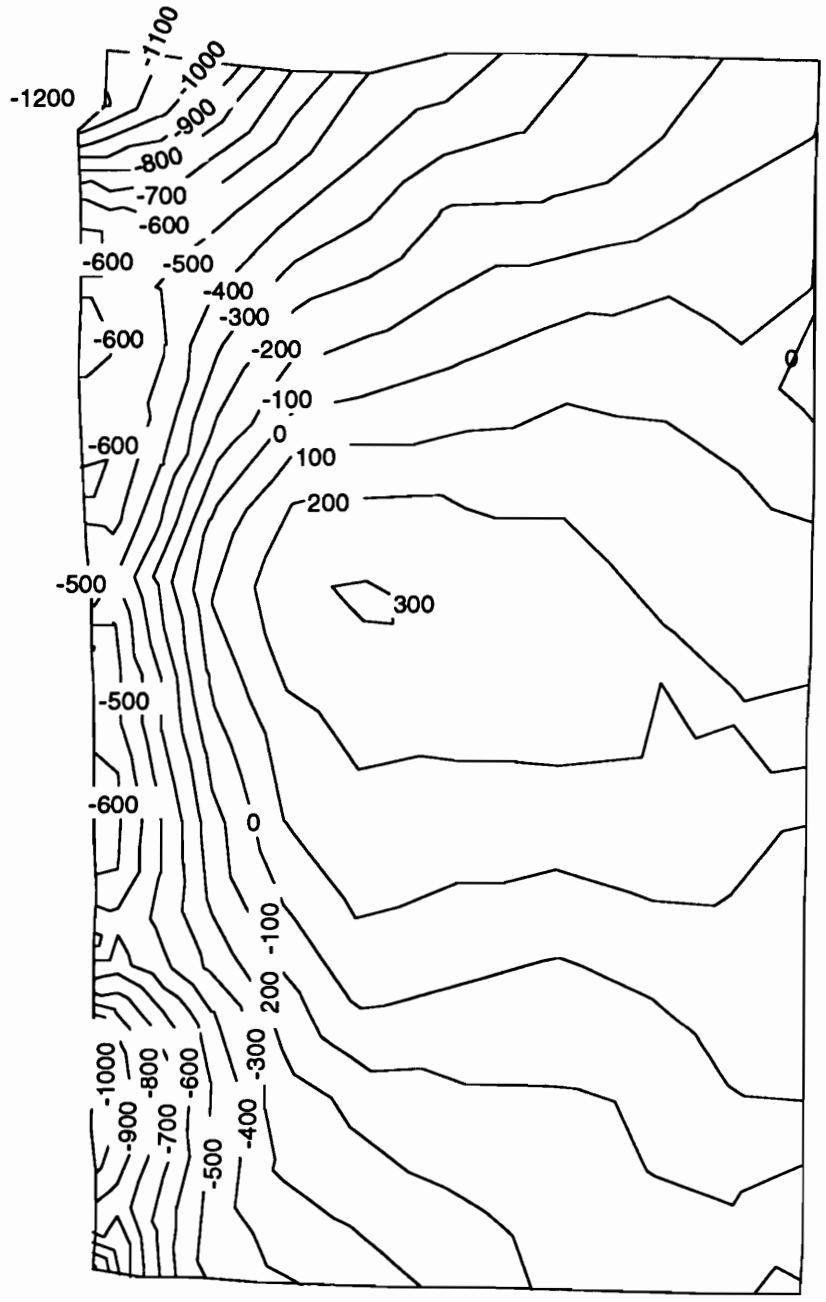

Figure 7.8 The horizontal strain contour (ε_x) with data smoothing. The contour interval is 100×10^{-6}.

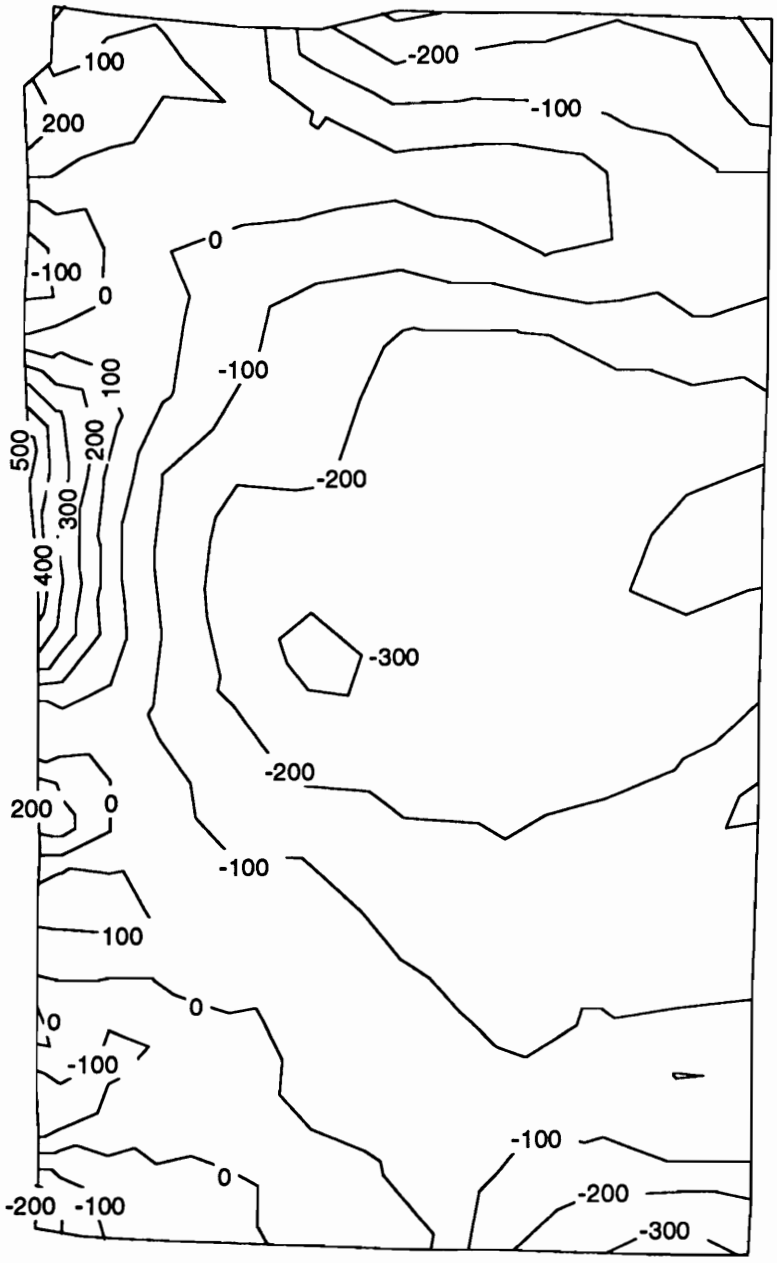

Figure 7.9 The vertical strain contour (ε_y) with data smoothing. The contour interval is 100×10^{-6}.

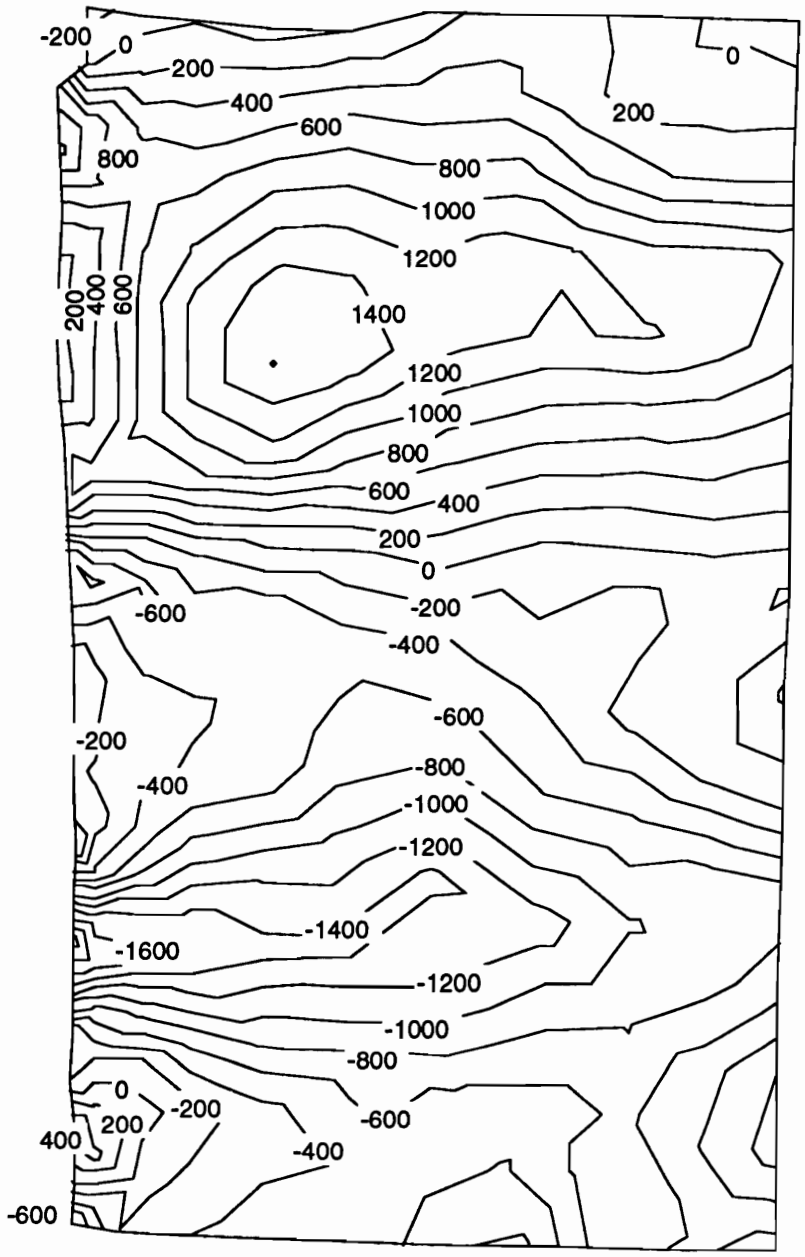

Figure 7.10 The shear strain contour (γ_{xy}) with data smoothing. The contour interval is 200×10^{-6}.

were applied in-plane in one load case. The strain patterns (ε_x, ε_y, and γ_{xy}) are shown in Figures 7.11, 7.12, and 7.13, respectively. Some local strain concentration was observed, especially in the region where the mesh was fine. The maximum error is $\frac{2 \times 20 \text{ nm}}{0.1 \text{ mm}}$ = 400×10^{-6} mm/mm, if the finite difference method is used. The value reflects the error if data-smoothing is not used. From the experience of the example in Chapter 6, with data smoothing the average error is 8×10^{-6}. The distance between neighboring data points, Δx, was 0.5mm. For the residual case, Δx is about 0.1mm. Since the average error is not proportional, conservatively speaking, the average error of the residual strain is less than 40×10^{-6}.

This example shows some advantages of the full-field hybrid method. First is that it can be used on a small area of interest that a strain gauge can hardly reach. Also, a full-field information is obtained instead of pointwise information. The resolution is at least five times higher than the traditional data reduction method. Furthermore, the data-smoothing model allows us to get accurate results even at low-fringe-density situation. And finally, no material property is required prior to analysis.

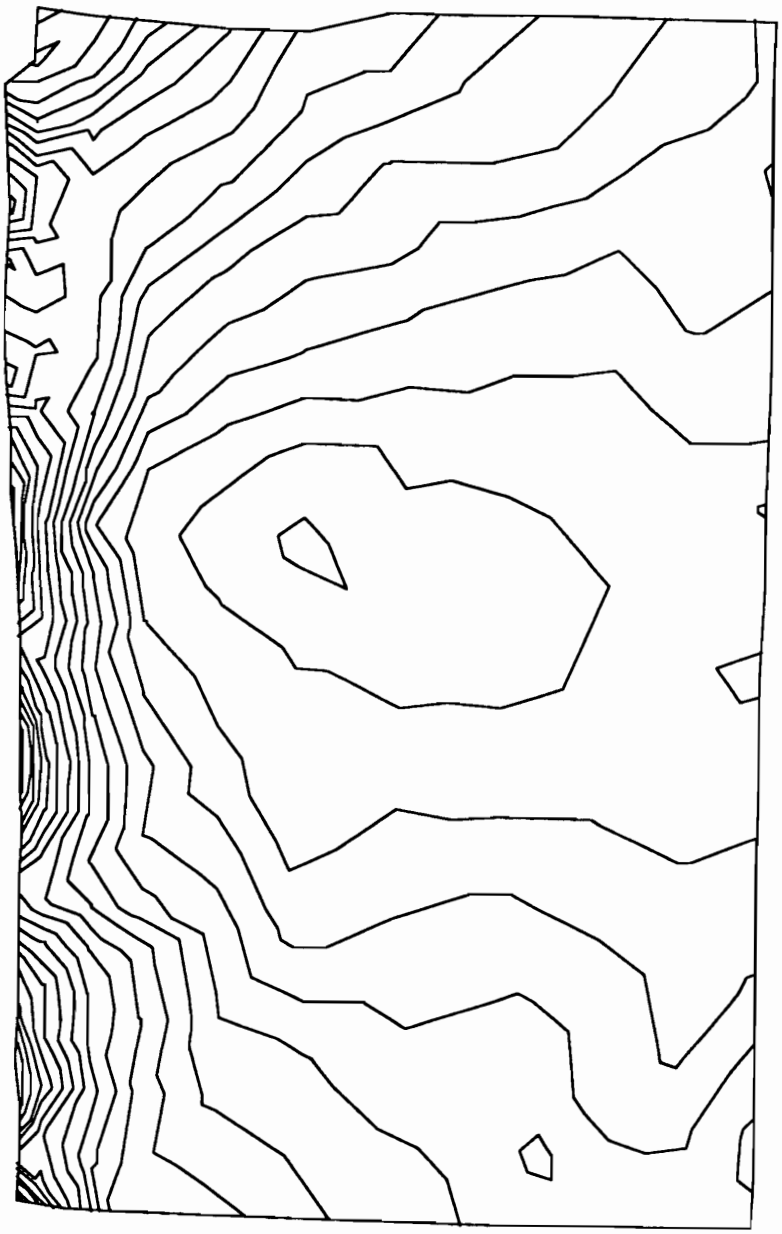

Figure 7.11 The horizontal strain (ε_x) contour without data smoothing. The contour interval is 100×10^{-6}. The maximum error is about 400×10^{-6}.

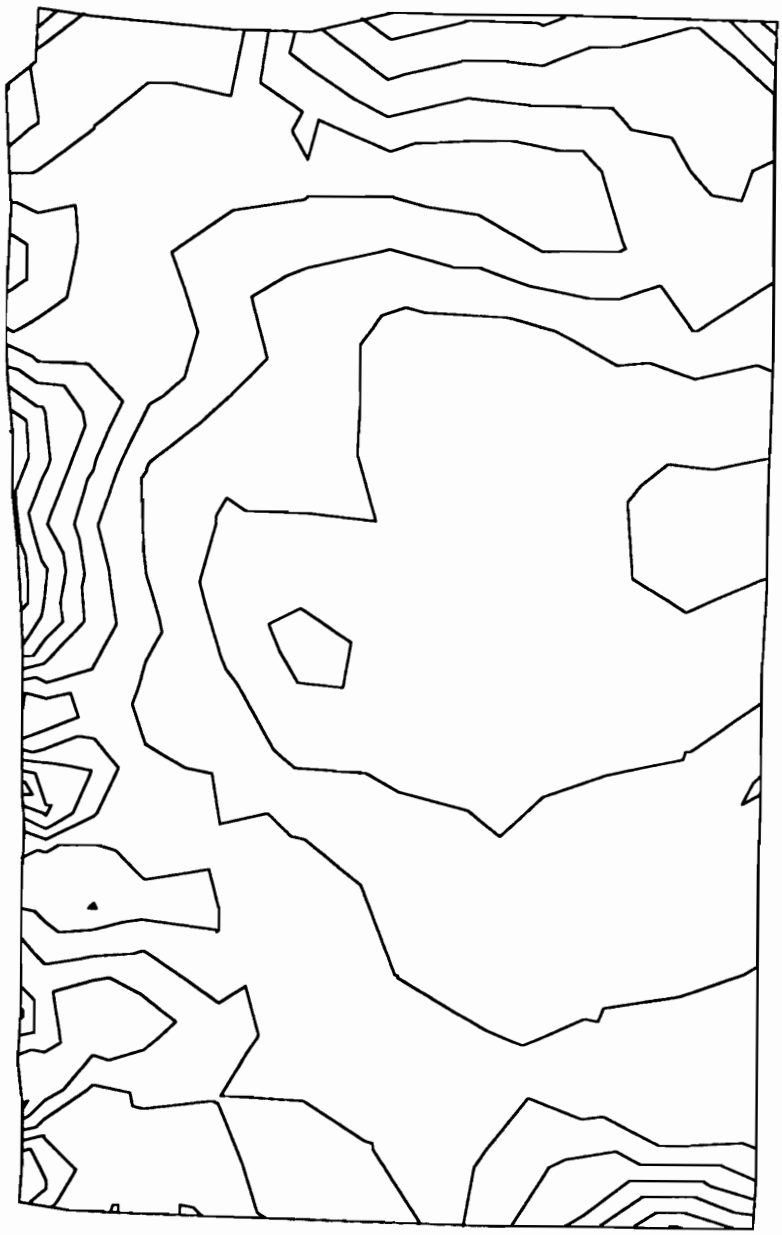

Figure 7.12 The vertical strain (ε_y) contour without data smoothing. The contour interval is 100×10^{-6}. The maximum error is about 400×10^{-6}.

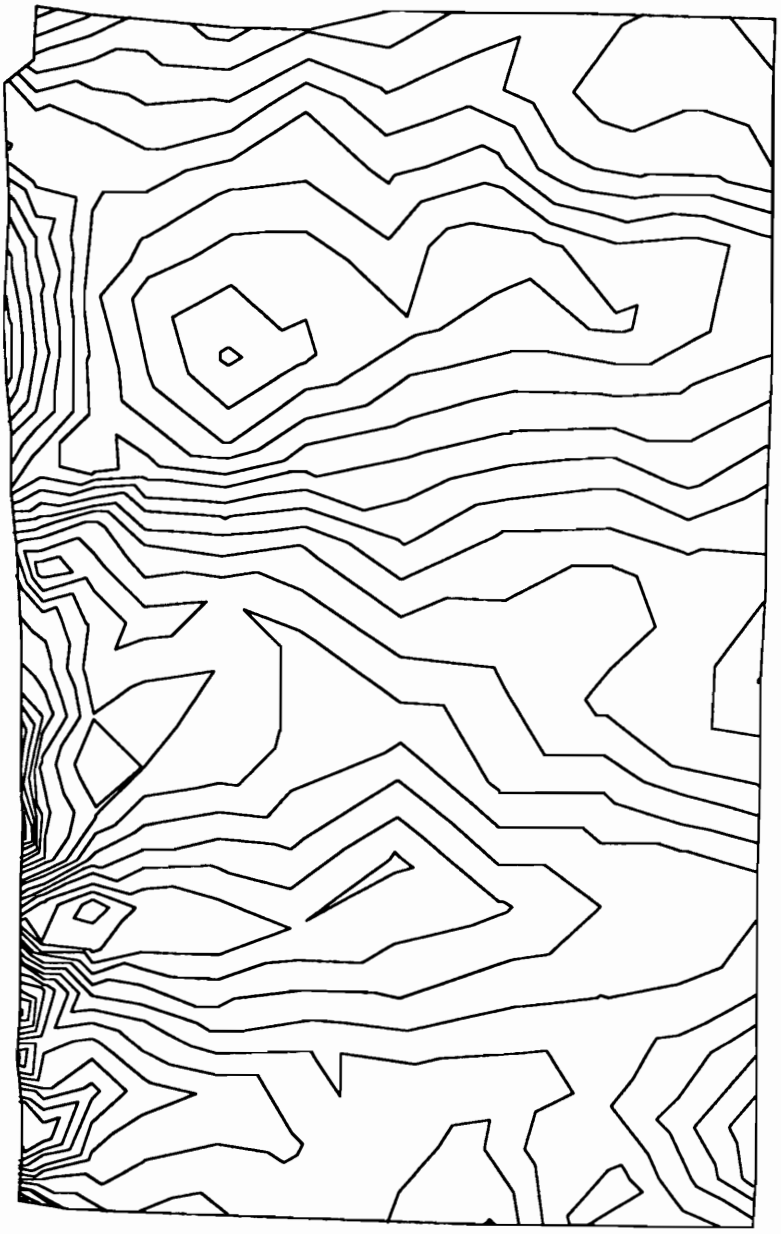

Figure 7.13 The shear strain (γ_{xy}) contour without data smoothing. The contour interval is 200×10^{-6}.

8 THE LOCALIZED HYBRID METHOD AND THE FULL-FIELD HYBRID METHOD - CRUCIFORM COMPOSITE SHEAR TEST

Both the localized hybrid method and the full-field hybrid method have been used to study the strain distribution of a cruciform composite shear test specimen. This is an example to compare these hybrid methods with exactly the same experimental data.

It must be emphasized that the localized method uses only boundary data, and the data is manually interpreted. A regular mesh is created for this method. The high-resolution data-reduction is not a standard practice for this method. The material properties must be known for the analysis. The full-field hybrid method instead uses full-field data all over the test section. A random mesh according to the digitized coordinates is created, and the high-resolution data-reduction technique is a standard procedure. The material properties will be needed only if the stress results are requested.

8-1 Cruciform Composite Shear Test with Moiré Interferometry

The cruciform specimen was designed with a view to determine the shear strength of composite materials. The general concept is illustrated in Figure 8.1 in which a cross-ply composite cruciform specimen is subjected to equal tensile and compressive loads. The fiber directions are at ±45° to the load axes so that a

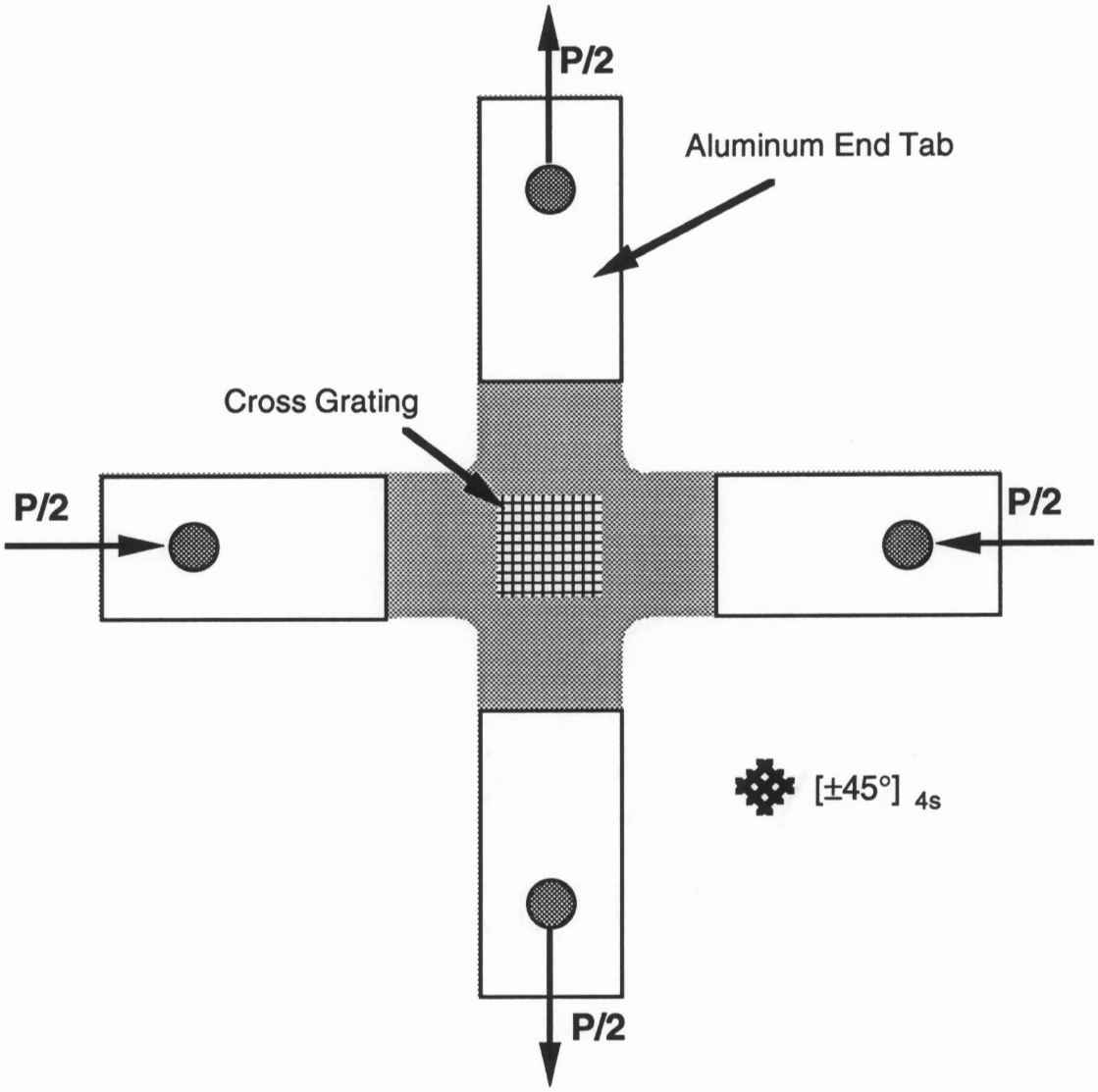

Figure 8.1 Cruciform composite shear test specimen

state of pure shear is developed in the principal directions of the material. Under ideal condition, the shear strain field in the specimen should be uniform throughout the test section.

The loading of the cruciform specimen is achieved by using the fixture shown in Figure 8.2. Eight rectangular steel bars are pinned together with the specimen and the adapters. The steel bars provide high stiffness compared to the extensional stiffness of the specimen so that the loading condition can be achieved.

The composite specimen was machined to the width of one inch on every legs. To enhance the bearing capability at the holes, the ends of the specimen were tabbed with aluminum. The material used in this study was a 16-ply AS4/3502-6 graphite-epoxy composite plate with a stacking sequence of $[\pm 45]_{4S}$. The material property data are listed in Appendix A.

Moiré interferometry provides a unique method of evaluating full-field surface displacements. The ideal condition can be easily checked for the existence in practice. To reduce vibration effects, this experiment was conducted with an achromatic moiré system which is vibration insensitive. An argon laser of wavelength 514 nm (green light) was used. The frequencies of the compensation grating and of the specimen grating were both 1200 line/mm. With the fringe multiplication factor set at 2, the sensitivity was 417 nm per fringe order.

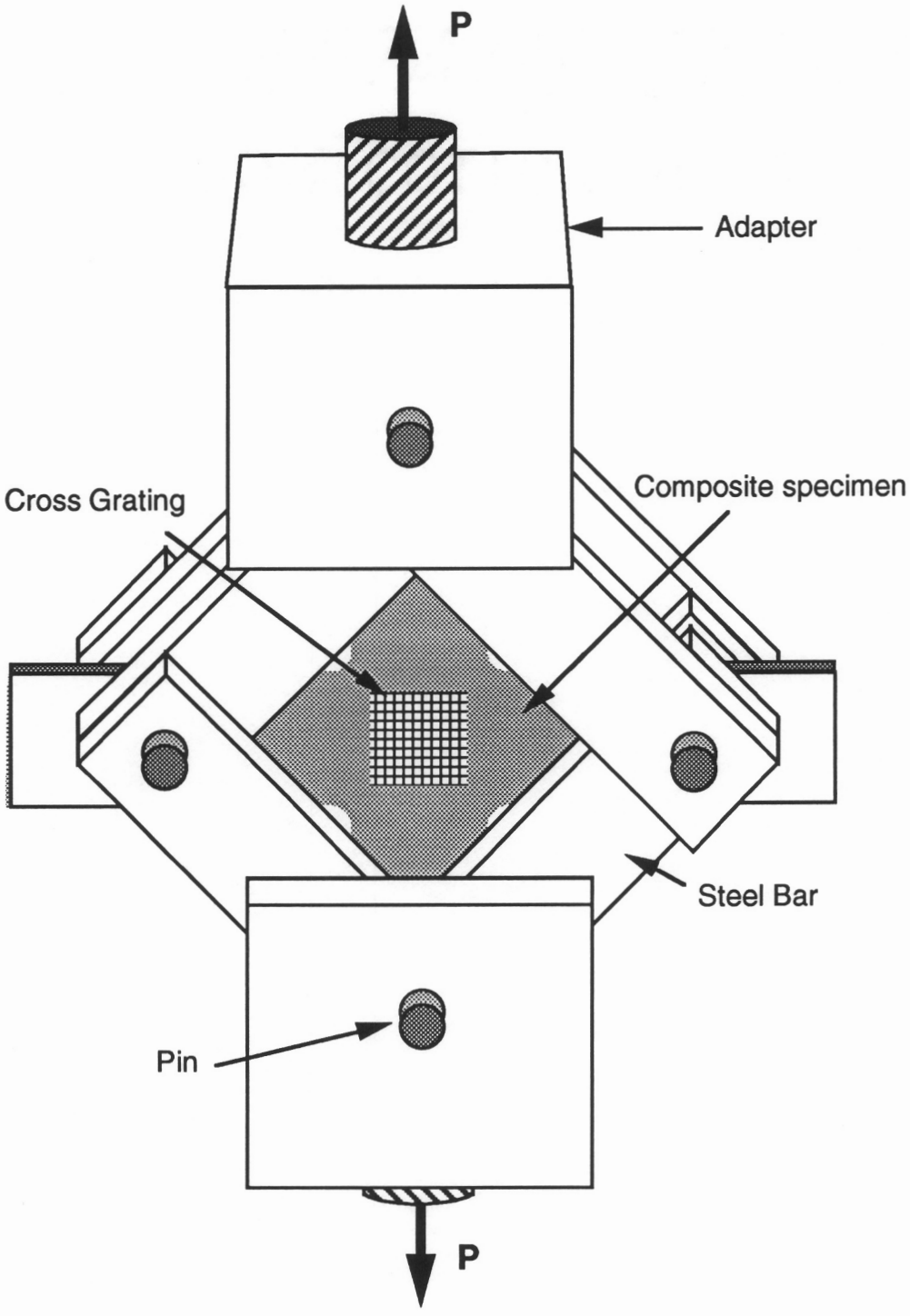

Figure 8.2 Cruciform composite shear test fixture

A total of five load steps were taken. The 302 pound (1343 Newton) load step was analyzed with both the localized hybrid method and the full-field hybrid method. The displacement patterns (U and V) of the load step were as shown in Figures 8.3 and 8.4. Since these patterns contained enough fringes for the data-reduction technique, no carrier fringe was introduced. In addition, a strain rosette was mounted on the back of the specimen.

8-2 The Results of the Localized Hybrid Method

For the localized hybrid method, the displacement patterns were manually interpreted around an area of 17.8 mm by 19.3 mm at the center of the test section. An FEM mesh was created as a 22 by 24 array of linear rectangular elements. The displacement data at the edges were listed as in the Appendix B. The mesh then was analyzed.

The design purpose of the cruciform test fixture is to provide a section of constant shear at the center of the specimen. However, from the results of the localized hybrid method as shown in Figures 8.5, 8.6, and 8.7 (ε_x, ε_y, and γ_{12} respectively), the strain distribution of the specimen is not uniform in the test section. As shown in the Figures 8.5 and 8.6, the maximum absolute strain level is 11% higher in the vertical direction (2900×10^{-6}) than in the horizontal direction (2550×10^{-6}). This result indicated that the load applied did not achieve the ideal condition. The maximum shear strain on

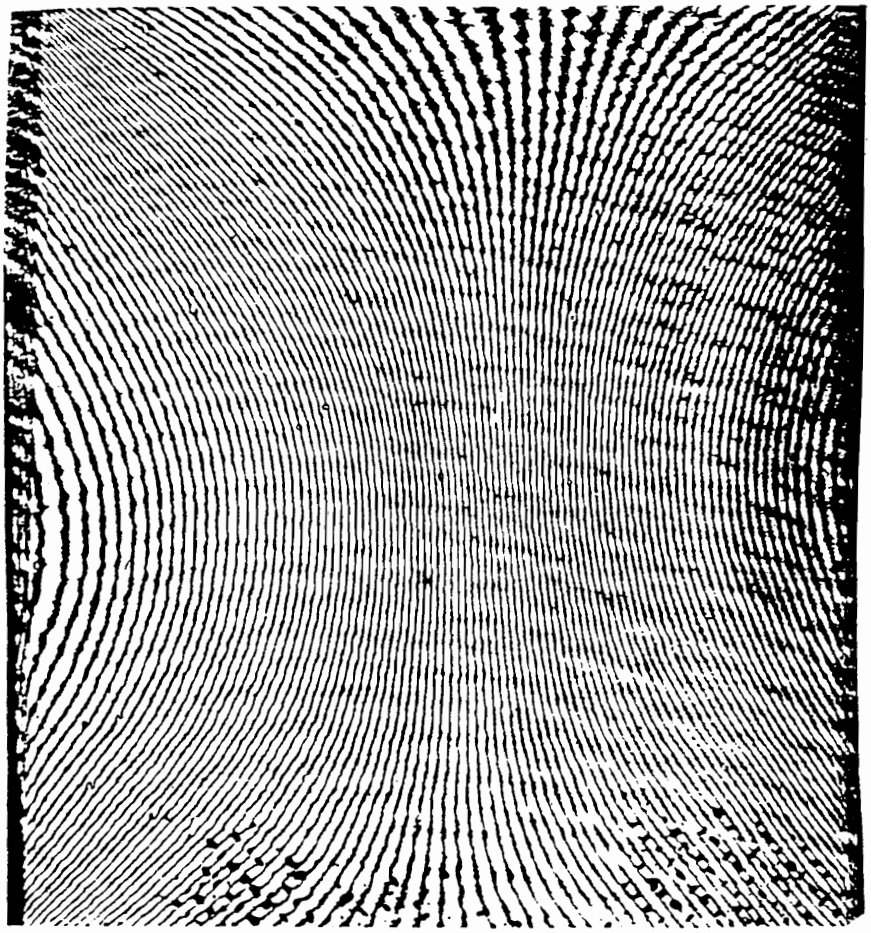

Figure 8.3 Horizontal (U) displacement pattern of the cruciform composite shear test

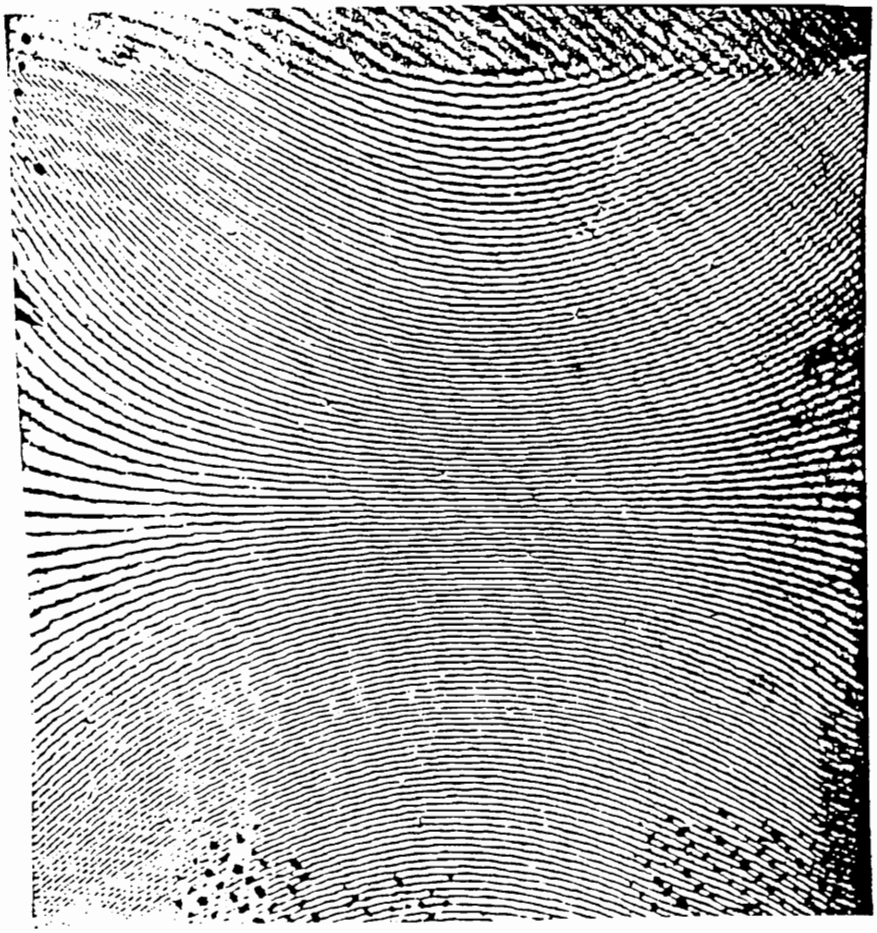

Figure 8.4 Vertical (V) displacement pattern of the cruciform composite shear test

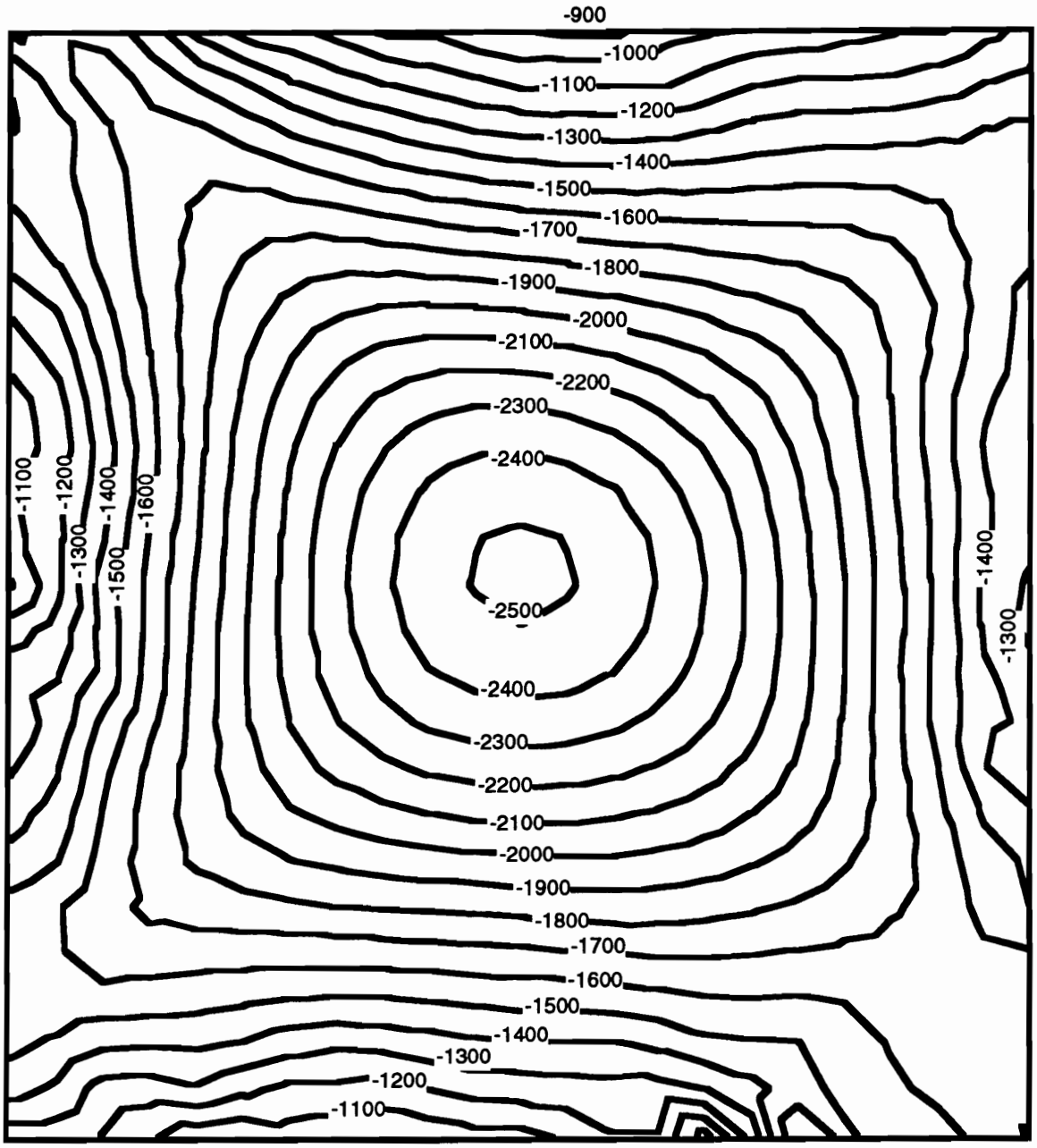

Figure 8.5 Horizontal strain distribution of the cruciform composite specimen from the localized hybrid method

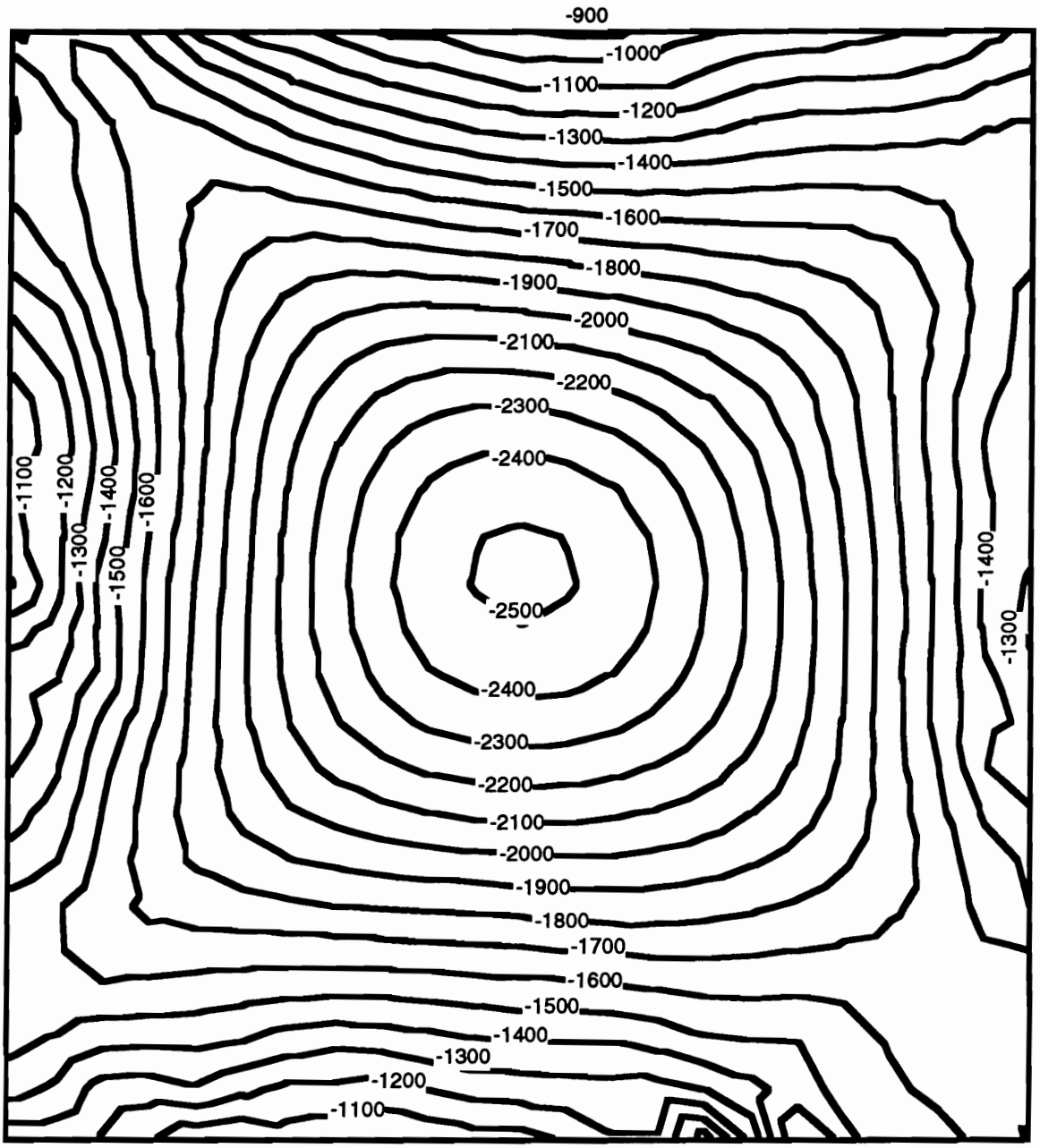

Figure 8.6 Vertical strain distribution of the cruciform composite specimen from the localized hybrid method

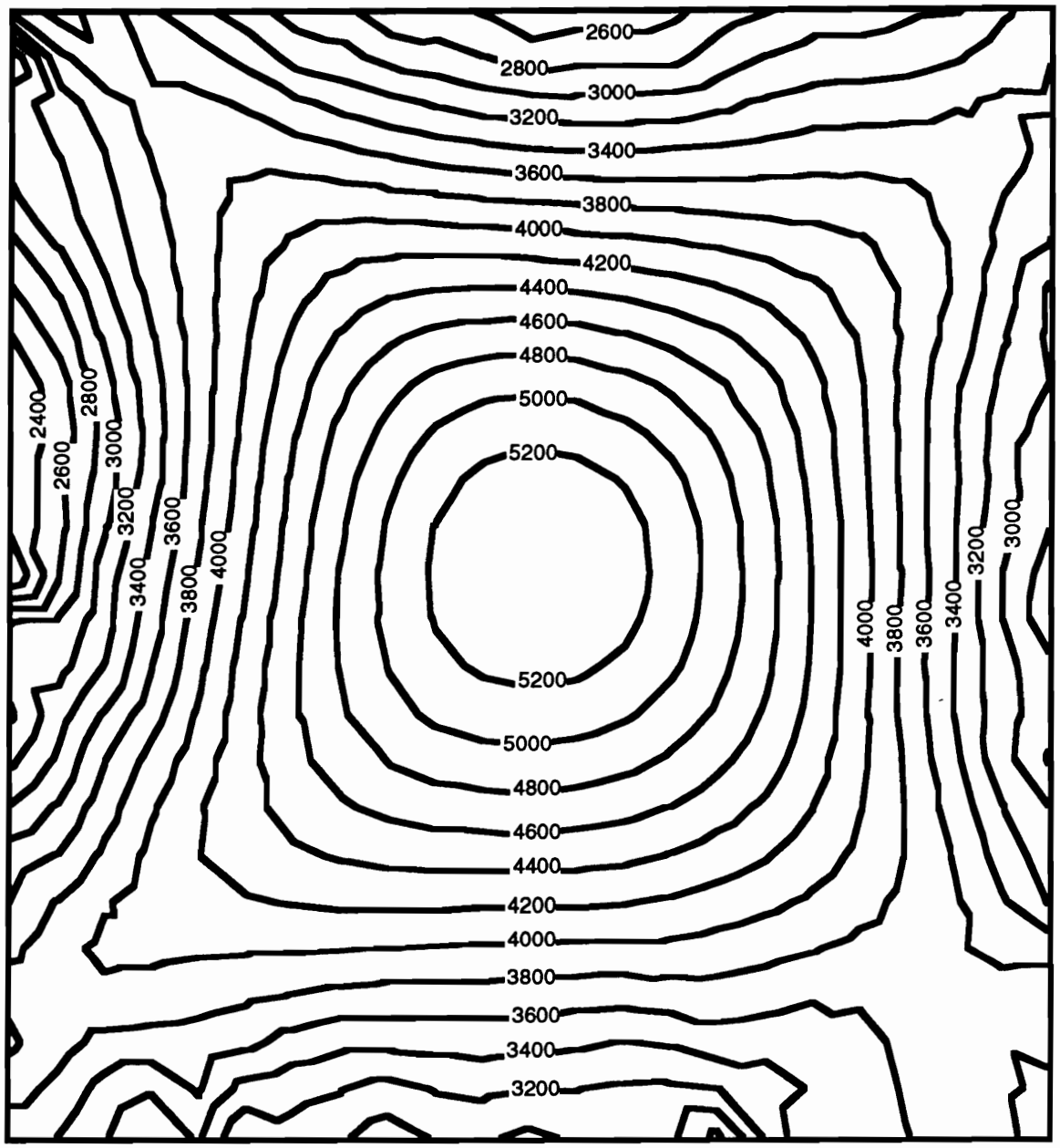

Figure 8.7 The maximum shear strain (γ_{12}) distribution of the cruciform composite specimen from the localized hybrid method

the test section varies from 2400×10^{-6} to 5500×10^{-6}. The gradient on the shear strain pattern shows that the pure shear state does not exist. However, the principal axes match the loading directions. The disturbance around the edges of the strain contours should be ignored because of the limited resolution of the manual data interpretation and the absence of data smoothing.

8-3 The Results of the Full-Field Hybrid Method

The same displacement fields shown in the Figures 8.3 and 8.4 were digitized according to the high-resolution data-reduction technique. A total of 491 data points were taken on the same area of the localized hybrid method. A random mesh with triangular elements was created as Figure 8.8 shows. A linear spring (not shown) was attached at every node and displaced at the free end, with the boundary condition obtained from the displacement contours. This mesh was written into a text file with directives that a FEM package can execute automatically.

It is part of the process that the smoothed results need to be checked. The smoothed displacement patterns were as shown in Figures 8.9 and 8.10. The fringe interval remained the same as in the original pictures. The smoothed patterns found matched the originals. In addition, the digital data were also checked to confirm that the smoothing criterion was satisfied. The strain distribution of the FEM results was processed and plotted as shown in

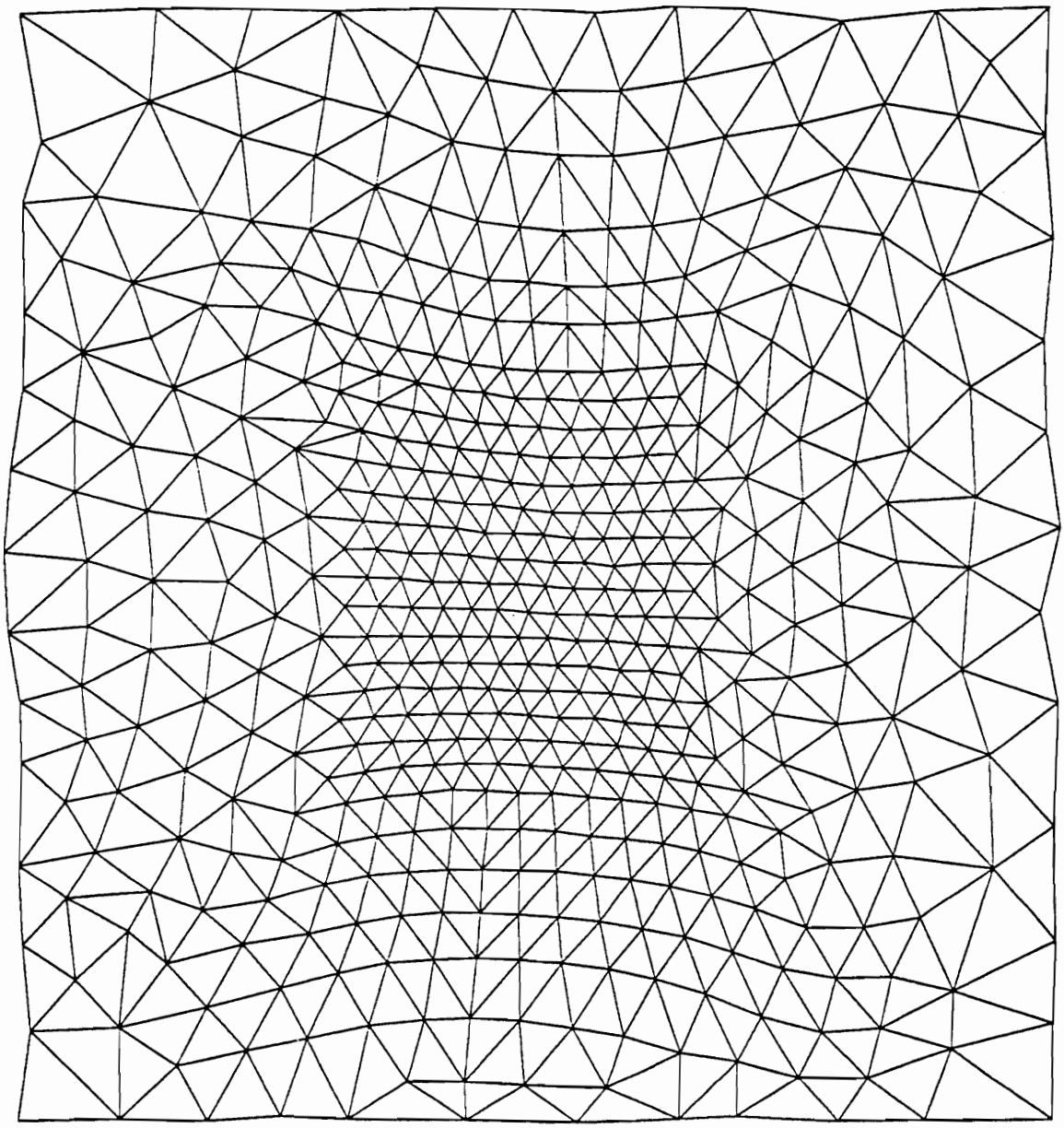

Figure 8.8 A random mesh created according to the digitized coordinates

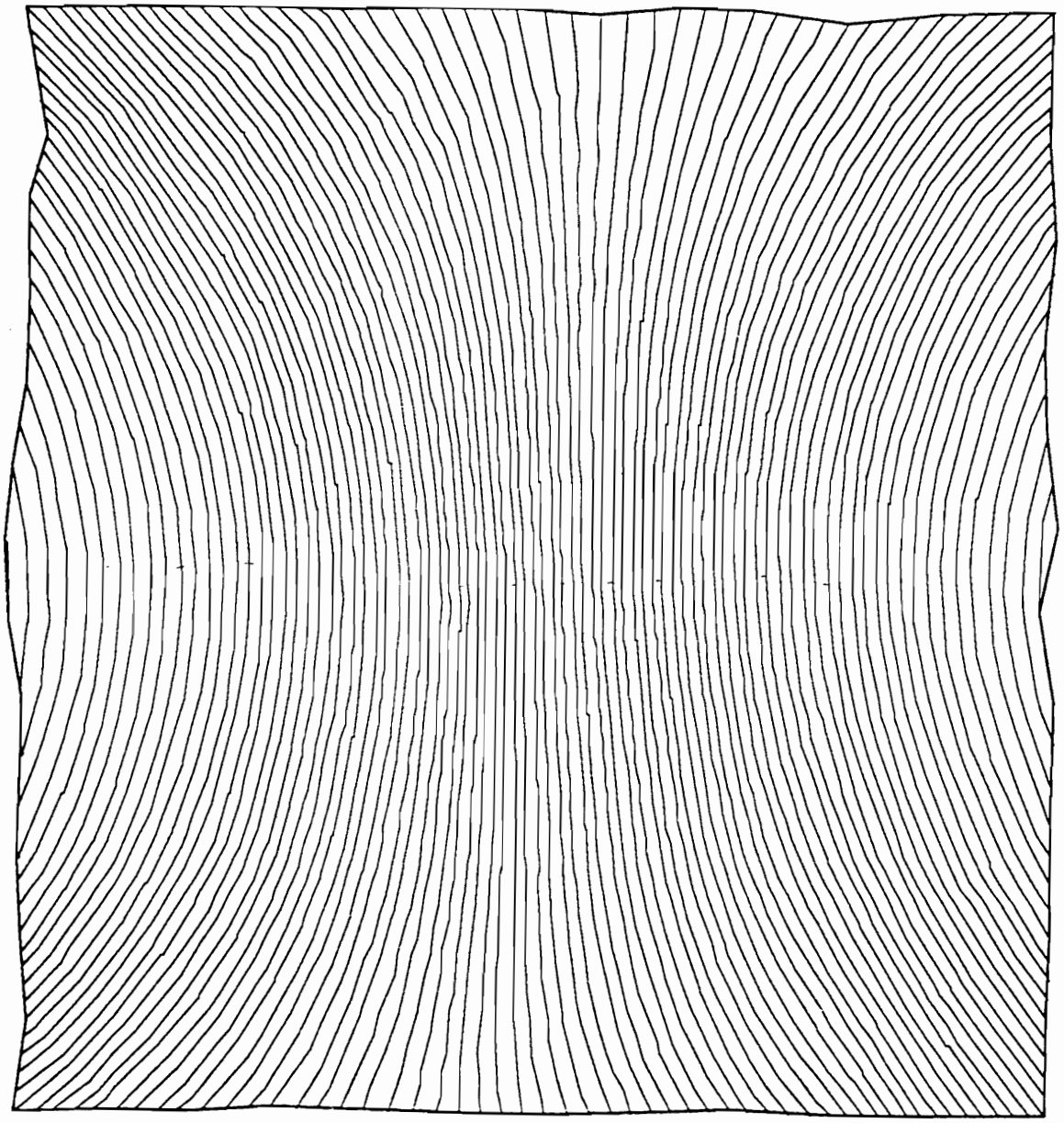

Figure 8.9 The smoothed U-displacement contour of the cruciform composite shear test from the full-field hybrid method.

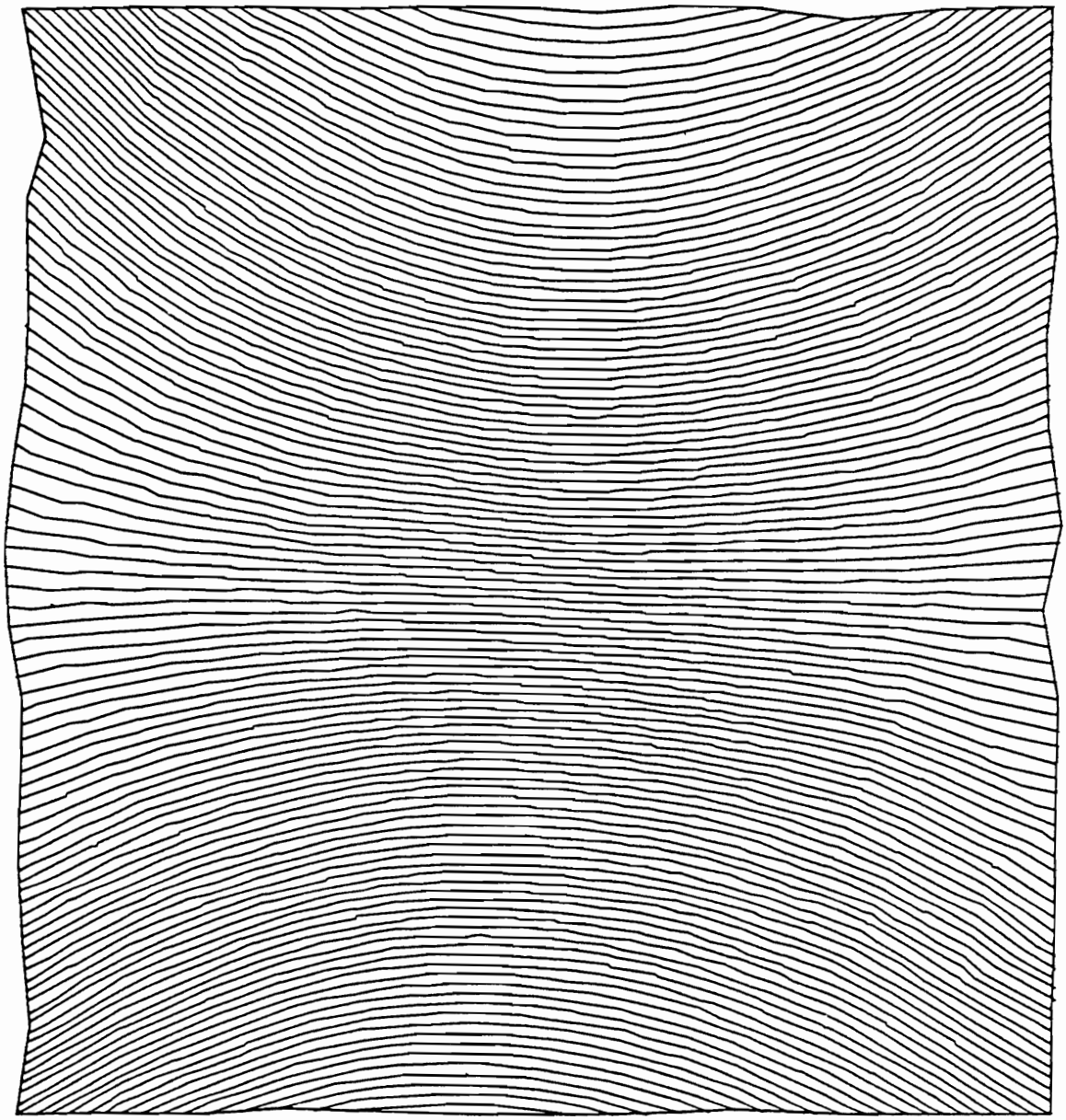

Figure 8.10 The smoothed V-displacement contour of the cruciform composite shear test from the full-field hybrid method.

Figures 8.11, 8.12, and 8.13 (ε_x, ε_y, and γ_{12} respectively). The ranges of strain components were -900×10^{-6} to -2600×10^{-6} for the horizontal strain, 1120×10^{-6} to 2900×10^{-6} for the vertical strain, and 2400×10^{-6} to 5500×10^{-6} for the maximum shear strain. These results also showed that the normal strain distributions have an 11% difference and the pure shear status does not exist at the test section as the localized hybrid method showed.

8-4 Mechanical Differentiation and Strain Gage Result

The mechanical differentiation is done by overlaying two copies of the same displacement pattern with a small amount of shifting. It requires a sufficient number of fringes to show the differentiated pattern. In this test, we did have enough fringes, and the differentiated patterns are shown in Figures 8.14 and 8.15 (ε_x and ε_y respectively). The advantage of these patterns is that they showed the trend of the strain contours and can be used as a reference for the hybrid methods.

In Figure 8.15, we noticed some disturbance in the vertical strain field. It was caused by the material non-uniformity. From the localized hybrid method, this phenomenon was not observed because of the material uniformity assumed in the analytical process. On the other hand, the full-field method showed the phenomenon because the strain fields were obtained directly from the displacement fields.

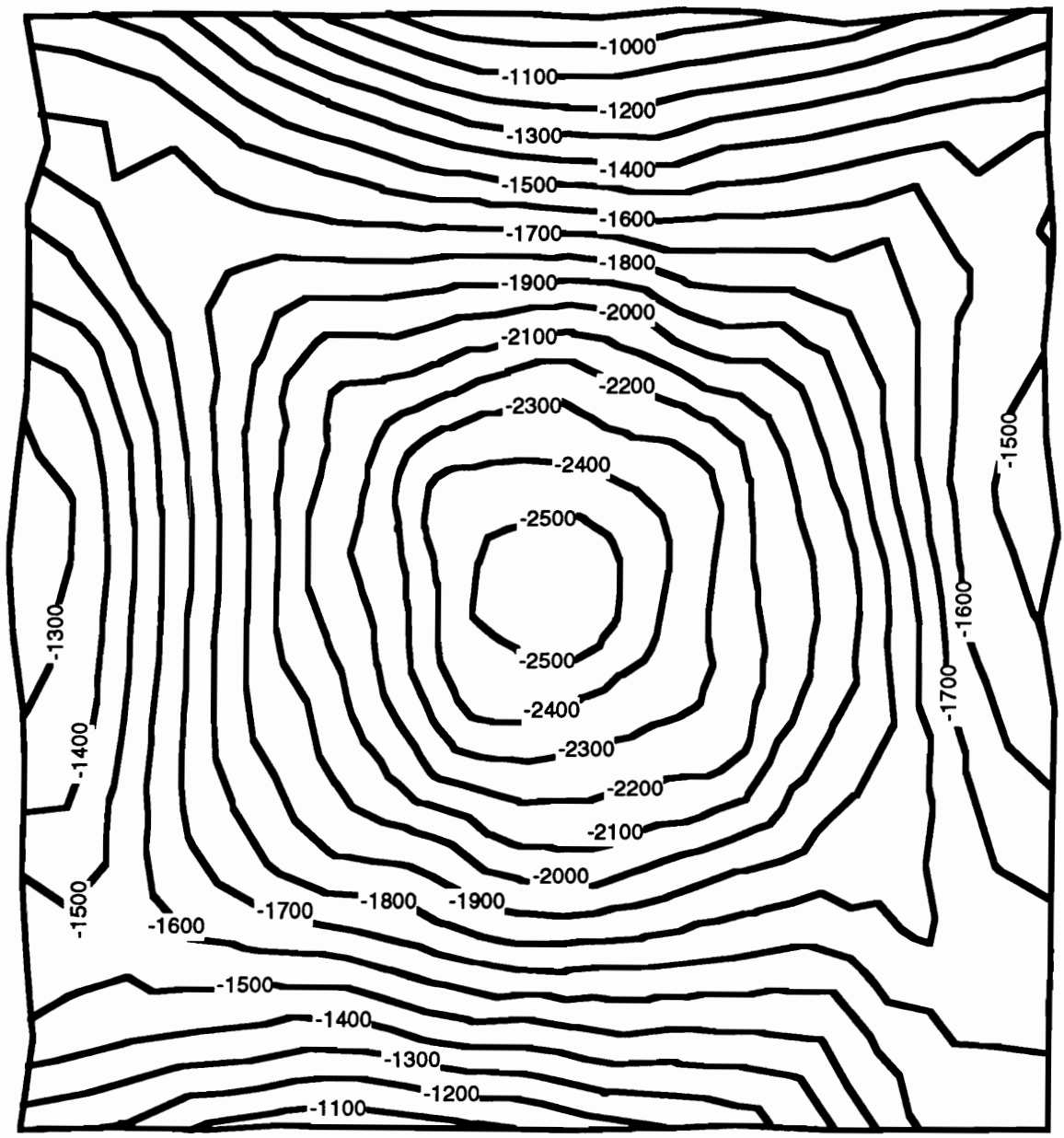

Figure 8.11 Horizontal strain distribution of the cruciform composite specimen from the full-field hybrid method

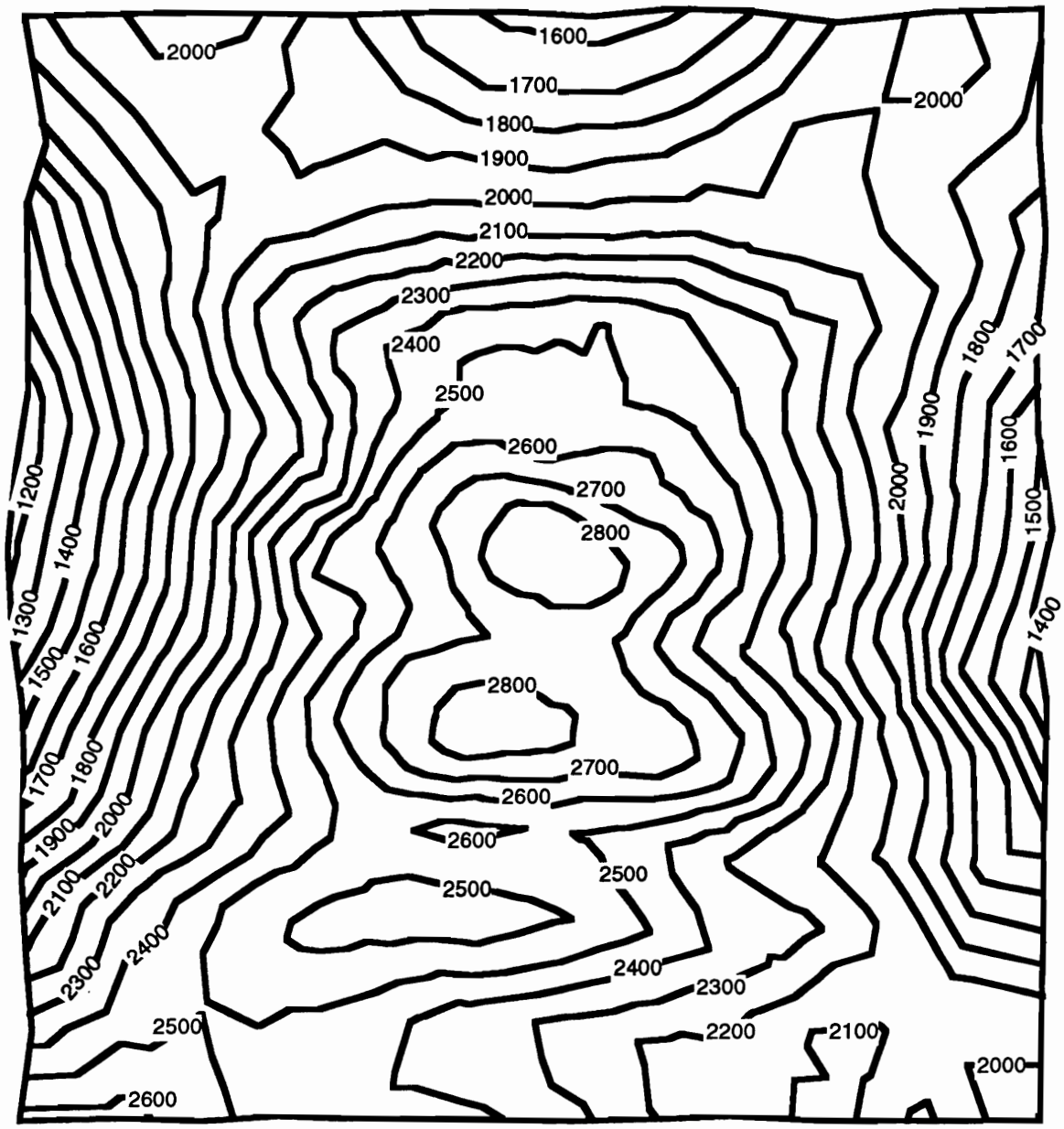

Figure 8.12 Vertical strain distribution of the cruciform composite specimen from the full-field hybrid method

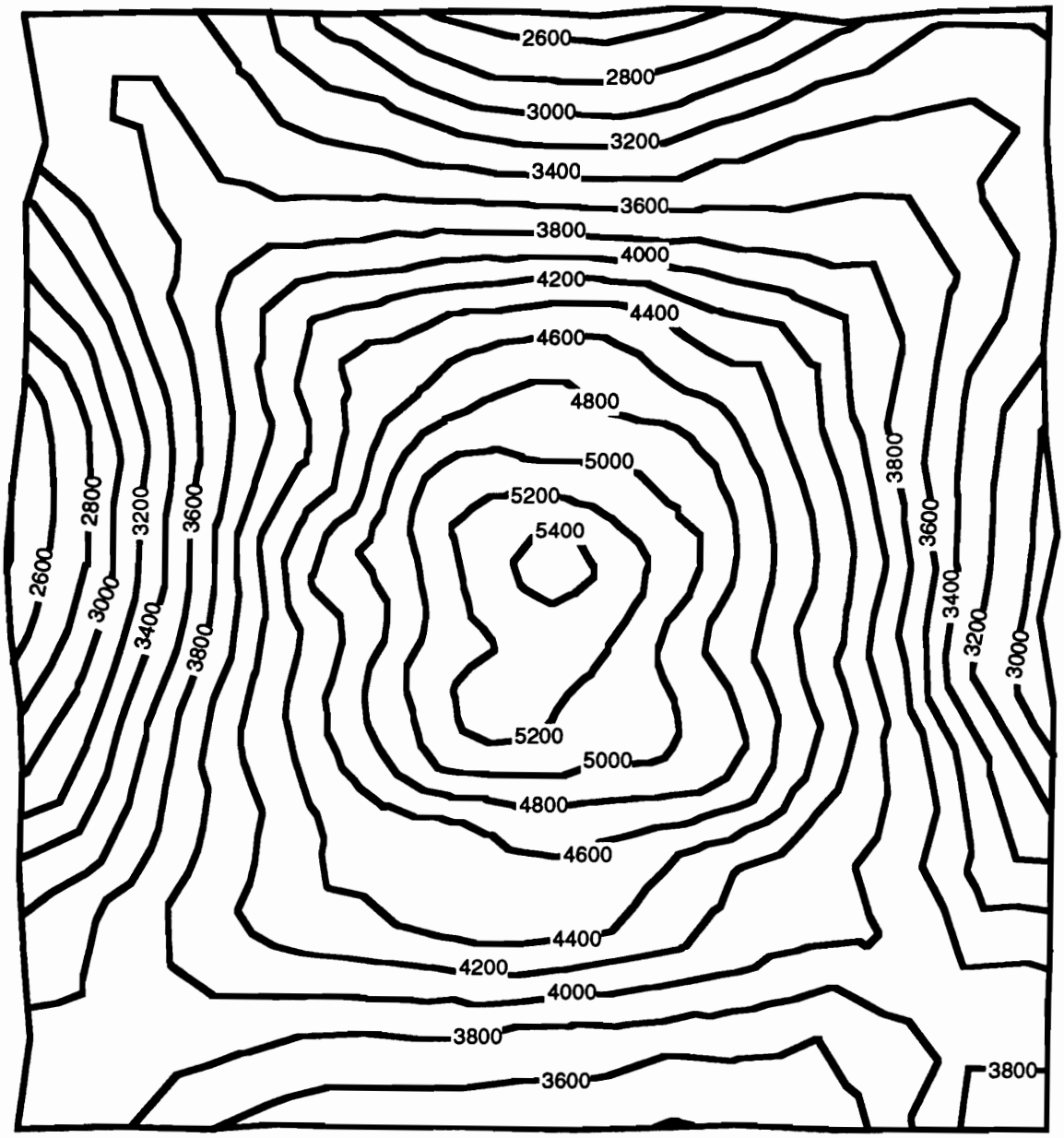

Figure 8.13 The maximum shear strain (γ_{12}) distribution (at 45°±2°) of the cruciform composite specimen from the full-field hybrid method

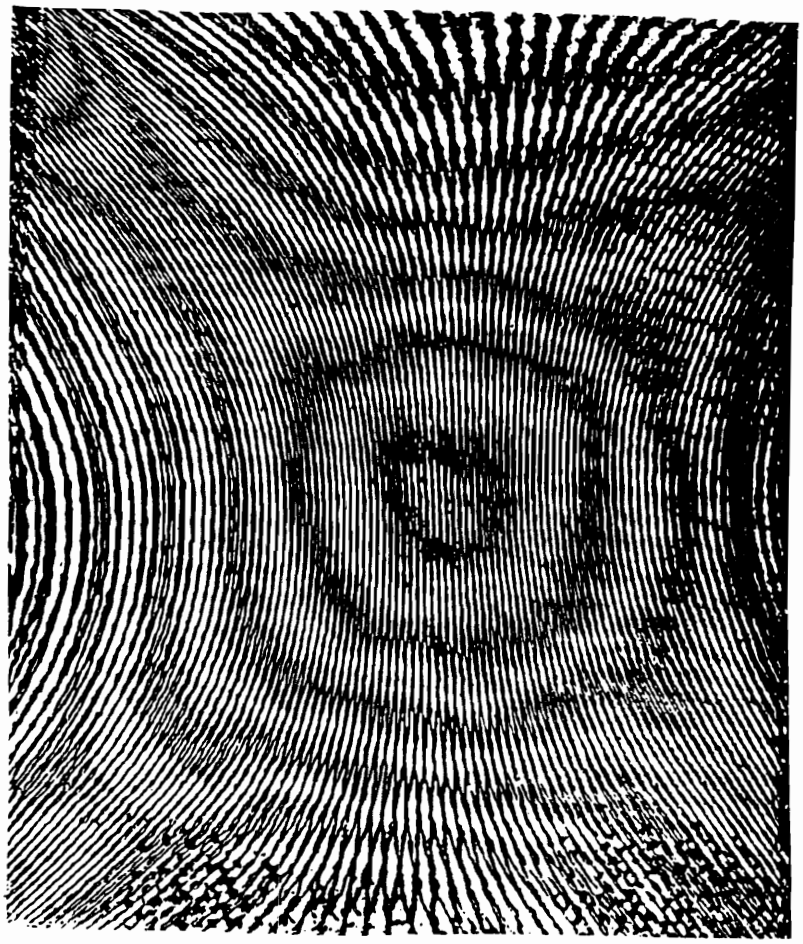

Figure 8.14 Mechanically differentiated U-field. The pattern represents horizontal strain contour.

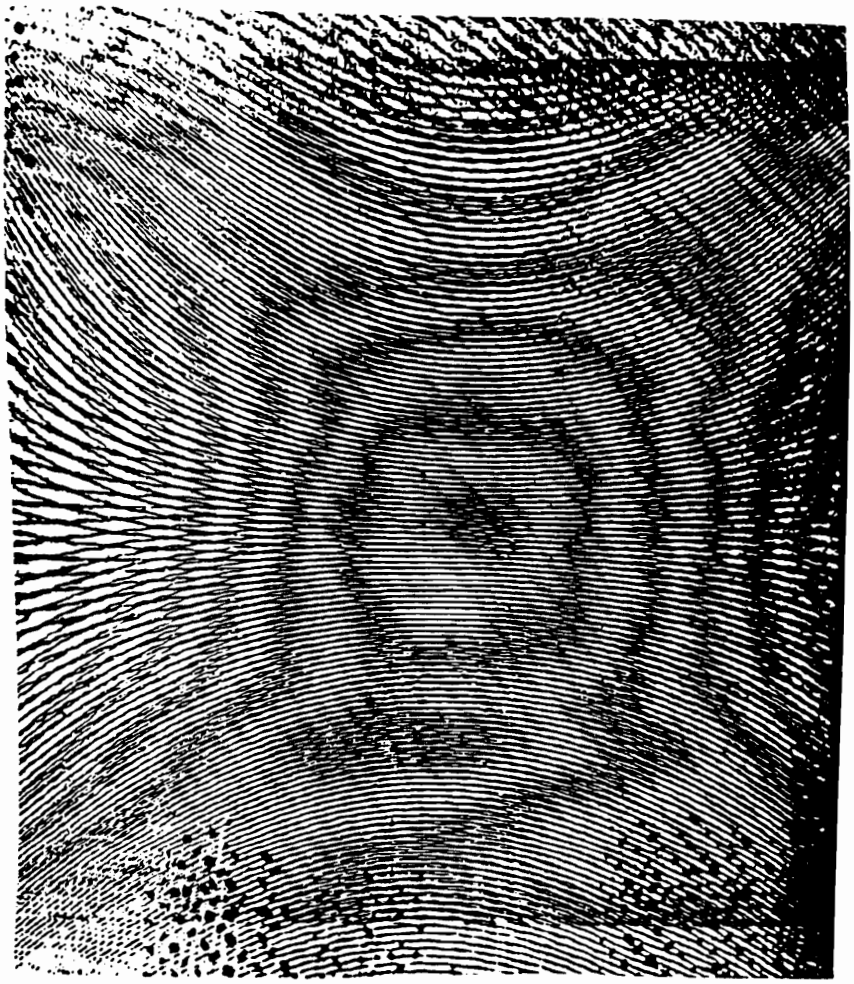

Figure 8.15 Mechanically differentiated V-field. The pattern represents vertical strain contour.

The strain rosette attached to the back of the specimen had a gage length of 1.5 mm. Three strain gages were aligned in 0°, 45° and 90° directions. Its position was at the center of the test section. At the 302 pound load (1343 Newton), the strain reading in the horizontal direction was -2540×10^{-6}. In the vertical direction, it was 2890×10^{-6}. These data matched the results of both hybrid methods. The 45° strain measured was very small. So, the maximum shear strain was about 5430×10^{-6}, which is very close to the maximum shear strain at the front surface. These results confirmed that the out-of-plane bending was negligible.

8-5 Discussion

The achromatic interferometer used in the experiment produced high quality, high contrast moiré fringes over the test section of the cruciform specimen, despite the limited access caused by the loading fixture. Both hybrid methods provided very similar results. However, the full-field analysis appeared to resolve some global non-uniform deformation which does not appear in the localized method. The non-uniformity is thought to be related to the fiber distribution in the specimen. If homogeneous material is tested, both methods should have very similar strain patterns.

Figure 8.16 shows the maximum shear strain distributions of both methods at the center of the test section along the horizontal axis. The maximum difference between the strains represented by

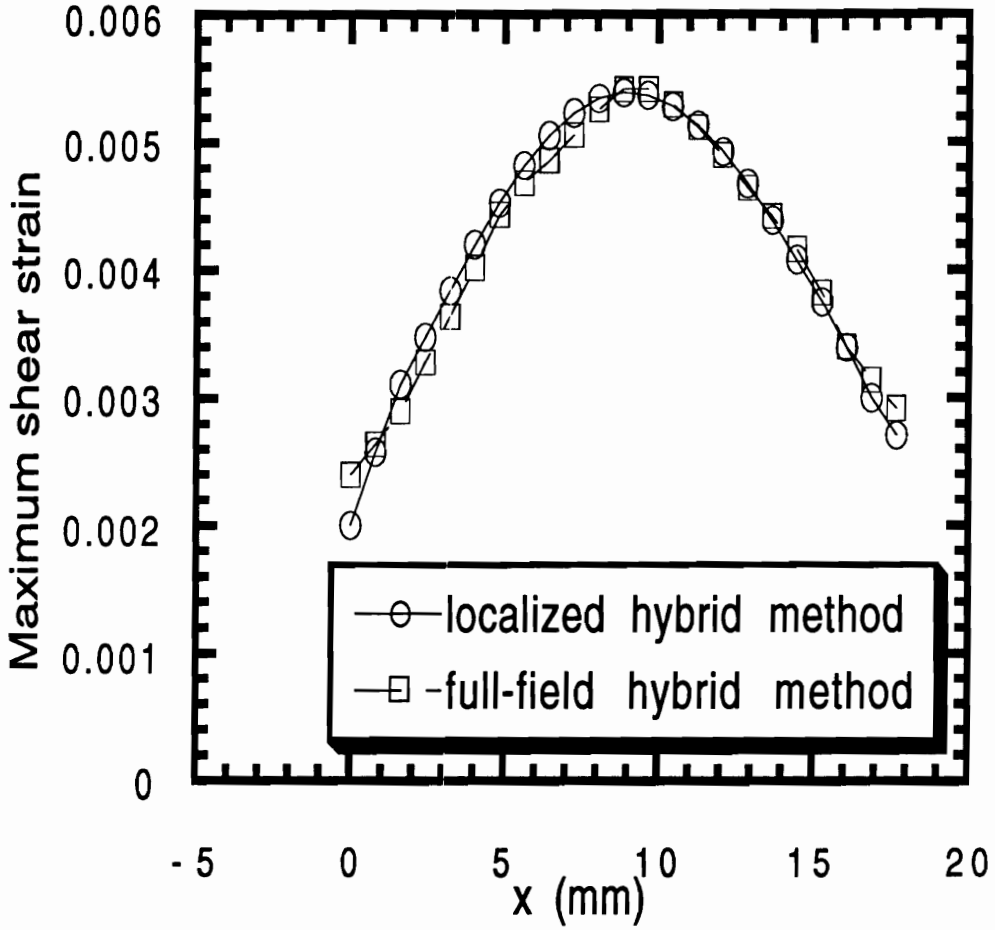

Figure 8.16 Comparison of the maximum shear strain distribution (γ_{12}) along the horizontal center line obtained from both hybrid methods.

the two curves, away from the edges, is only 70×10^{-6}. At the center of the test section, both results are extremely close.

9 SUMMARY

The full-field hybrid method has been demonstrated with two different cases. Even though two moiré systems were used, the results were processed in exactly the same way. The decision to use the moiré system depends solely upon the situation of the experiments. Except for the carrier fringes, which are used in the composite residual test, the conventional moiré test procedures remain unchanged. No extra equipment is required. In addition, this method is not restricted to the moiré test results. Any two dimensional displacement contours could be analyzed with minor or no change in the method. The results of the grid method and holography are possible fields of the applications of the hybrid method.

The composite residual strain test was an extreme case of small test section and small number of fringes. In this case, the amount of error became so critical that the conventional method did not work anymore. The resolution of the moiré data needs to be enhanced, as was done by the high-resolution data-reduction technique. Without the advantage of high-resolution data, the localized hybrid method would have too much error if used to analyze these experimental results. However, with some modification, the high-resolution data-reduction technique could work with the localized hybrid method.

The full-field method demonstrated its capability to attack the situation like the residual case. With high-resolution data, the maximum error in displacement for a data point is less than 20 nm. As demonstrated in the example of Chapter 6, this resolution is still not good enough for a case like this. Therefore, the use of the two-dimensional data-smoothing model is necessary and also successful. Additionally, it is proven in the example that the error percentage is lowered when more data points are taken.

The localized hybrid method worked well with the cruciform composite shear test. It has a comfortable test area and plenty of fringes. The resolution was not critical for this test. In order to complete the localized hybrid method, the material properties were needed for the finite-element analysis. The material uniformity was also assumed. However, it is common that composite materials would show some local effects, like those seen in the vertical strain field of the shear test. The localized hybrid results could not show this effect due to the homogeneous material assumption. On the other hand, the full-field method demonstrated its capability to detect any global non-uniformity on the strain fields. The disturbance shown in the vertical strain field of the cruciform composite shear test was also shown in the pattern derived by the mechanical differentiation. The differentiated pattern shows what really exists in the experimental data except for lower quality. The

full-field method turned out to reflect more detail in the moiré results.

Although the strain contours of the hybrid methods looked different, the difference between them was only up to 70×10^{-6} at any given point away from the edge. As far as the accuracy of the experiment is concerned, the amount of difference is negligible. Also, the maximum values of strains matched the reading of the strain rosette.

The FEM packages used do not affect our results. However, the capability of batch mode execution is preferred, because it can save plenty of time in the analysis. Some popular FEM packages, such as PATRAN and ABAQUS, have been successfully interfaced. These packages can really be used by the hybrid method user as a black box - one does not even have to know how to generate a mesh or read the results. For more convenience, a FEM package (FE77), running on a Macintosh computer for which the programs were written, is also available.

To analyze a pair of full-field moiré patterns, the time required is extremely long if the conventional method is used. If only a few fringes are present in the patterns, it is impossible to get reasonably good results with the conventional method. The full-field hybrid method is developed in such a way that the whole procedure is routine and very much automatic. A regular case will

take three to six hours, depending on how many data points are taken. The digitizing process takes most of the time.

10 Conclusions

The premise of the full-field hybrid method is that two-dimensional results are requested. As it was developed, the advantages of the hybrid method are as follows:

— Moiré system does not have to be changed.

— The method is applicable to any two-dimensional displacement data.

— No material property data are required.

— The method retains full-field nature of the moiré data.

— It provides high-resolution displacement data from moiré.

— It can be used to handle hard-to-analyze patterns.

— It saves time on moiré pattern analysis.

— It can be used to detect any global non-uniformity in the patterns.

— It provides two-dimensional data smoothing to minimize the error.

Compared to the localized hybrid method, the disadvantage is that the full-field method needs more time for the digitizing process. Finally, experience and engineering judgment of the user can really shorten the time needed to perform the analysis.

Appendix A Material property data used in the localized hybrid method for the analysis of cruciform composite shear test results. The data are for a unidirectional lamina.

E_{11}, along the fiber direction	136.6GPa
E_{22}, perpendicular to the fiber direction	9.72GPa
G_{12}, shear modulus	5.03GPa
ν_{12}, Poisson's ratio	0.35

Appendix B Nodal displacement boundary conditions of the localized hybrid method.

x (in mm)	y (in mm)	u (in mm)	v (in mm)
0.000	0.000	0.0196	-0.0008
0.804	0.000	0.0186	-0.0021
1.608	0.000	0.0176	-0.0032
2.411	0.000	0.0167	-0.0041
3.215	0.000	0.0158	-0.0052
4.019	0.000	0.0150	-0.0056
4.823	0.000	0.0142	-0.0062
5.627	0.000	0.0133	-0.0065
6.430	0.000	0.0125	-0.0067
7.234	0.000	0.0117	-0.0069
8.038	0.000	0.0108	-0.0069
8.842	0.000	0.0100	-0.0067
9.646	0.000	0.0091	-0.0064
10.449	0.000	0.0082	-0.0059
11.253	0.000	0.0072	-0.0054
12.057	0.000	0.0063	-0.0048
12.861	0.000	0.0057	-0.0040
13.665	0.000	0.0042	-0.0033
14.468	0.000	0.0031	-0.0024
15.272	0.000	0.0019	-0.0015
16.076	0.000	0.0006	-0.0005
16.880	0.000	-0.0006	0.0006
17.684	0.000	-0.0020	0.0017
0.000	0.804	0.0207	0.0010
0.000	1.608	0.0218	0.0031
0.000	2.411	0.0228	0.0049
0.000	3.215	0.0237	0.0067
0.000	4.019	0.0245	0.0082
0.000	4.823	0.0250	0.0098
0.000	5.627	0.0255	0.0112
0.000	6.430	0.0259	0.0124
0.000	7.234	0.0262	0.0136
0.000	8.038	0.0263	0.0147
0.000	8.842	0.0264	0.0162
0.000	9.646	0.0264	0.0168
0.000	10.449	0.0263	0.0178
0.000	11.253	0.0261	0.0187
0.000	12.057	0.0257	0.0197

0.000	12.861	0.0253	0.0206
0.000	13.665	0.0249	0.0215
0.000	14.468	0.0244	0.0225
0.000	15.272	0.0237	0.0235
0.000	16.076	0.0229	0.0246
0.000	16.880	0.0220	0.0259
0.000	17.684	0.0208	0.0271
0.000	18.487	0.0197	0.0285
0.000	19.291	0.0184	0.0294
0.804	19.291	0.0171	0.0317
1.608	19.291	0.0158	0.0333
2.411	19.291	0.0146	0.0345
3.215	19.291	0.0135	0.0358
4.019	19.291	0.0125	0.0367
4.823	19.291	0.0116	0.0375
5.627	19.291	0.0107	0.0383
6.430	19.291	0.0099	0.0388
7.234	19.291	0.0091	0.0392
8.038	19.291	0.0083	0.0395
8.842	19.291	0.0076	0.0396
9.646	19.291	0.0069	0.0398
10.449	19.291	0.0062	0.0398
11.253	19.291	0.0055	0.0396
12.057	19.291	0.0047	0.0395
12.861	19.291	0.0039	0.0392
13.665	19.291	0.0030	0.0388
14.468	19.291	0.0022	0.0381
15.272	19.291	0.0013	0.0374
16.076	19.291	0.0005	0.0366
16.880	19.291	-0.0004	0.0357
17.684	19.291	-0.0014	0.0346
17.684	18.487	-0.0025	0.0329
17.684	17.684	-0.0035	0.0313
17.684	16.880	-0.0045	0.0297
17.684	16.076	-0.0054	0.0282
17.684	15.272	-0.0063	0.0267
17.684	14.468	-0.0070	0.0254
17.684	13.665	-0.0075	0.0242
17.684	12.861	-0.0080	0.0229
17.684	12.057	-0.0084	0.0215
17.684	11.253	-0.0087	0.0203
17.684	10.449	-0.0089	0.0192
17.684	9.646	-0.0090	0.0180
17.684	8.842	-0.0089	0.0169
17.684	8.038	-0.0088	0.0158
17.684	7.234	-0.0085	0.0145
17.684	6.430	-0.0081	0.0133

17.684	5.627	-0.0078	0.0122
17.684	4.823	-0.0072	0.0109
17.684	4.019	-0.0065	0.0097
17.684	3.215	-0.0057	0.0083
17.684	2.411	-0.0048	0.0067
17.684	1.608	-0.0040	0.0051
17.684	0.804	-0.0030	0.0035

REFERENCES

1 Morton, J., Post, D., Han, B. T., M. Y. Tsai, "A Localized Hybrid Method of Stress Analysis: A Combination of Moiré Interferometry and FEM", Experimental Mechanics, pp195-200, June 1990.

2 Tsai, M. Y., "Application of Localized Hybrid Methods of Stress Analysis to Some Problems in the Mechanics of Composites", Ph.D. Dissertation, Engineering Science & Mechanics Department, Virginia Polytechnic Institute & State University, November 1990.

3 Voloshin, A. S., Burger, C. P., Rowlands,.R. E., Richard, T. G., "Fractional Moiré Strain Analysis Using Digital Imaging Techniques", Experimental Mechanics, 26, pp254-258, September 1986

4 Ning, P.-T., Peng, W.-L., "Automatic Analysis of Moiré Fringe Patterns by Using an Image-Processing System", Experimental Mechanics, 28, pp350-354, December 1988

5 Lee, C. A., Richard, T. G., Rowlands, R. E., "Exact Interpretation of Moiré Fringe Patterns in Digital Images", Experimental Mechanics, 28, pp409-416, December 1988

6 Chen, T. Y., Taylor, C. E., "Computerized Fringe Analysis in Photomechanics", Experimental Mechanics, 29, pp323-329, September 1989

7 Czarnek, R., J. Lee and T. Rantis, "Moiré Interferometry with Enhanced Resolution," Experimental Techniques, 14, pp.24-28 , July/August 1990

8 Lee, J., "High Resolution Interferometric Measurements of Residual Strains in Composites", Ph. D. Dissertation, Engineering Science & Mechanics Department, Virginia Polytechnic Institute & State University, December 1990.

9 Chiang, F. P., "Moiré Methods of Strain Analysis", Doyle, J. F., Phillips, J. W., eds., Chapter 7, Manual on Experimental Stress Analysis, pp107-135, 1989

10 Czarnek, R.,"Three-Mirror, Four-Beam Interferometer and Its Capabilities," Optics and Lasers in Engineering, pp93-101, 15, 1991

11 White, J. W., Fraser, W. A., "Making Optical Elements," U.S. Patent 2,464,738, March 15, 1949.

12 Czarnek, R.,"New Methods in Moiré Interferometry", Ph.D. Dissertation, Engineering Science & Mechanics Department, Virginia Polytechnic Institute & State University, December 1984).

13 Czarnek, R., "High-sensitivity Moiré Interferometry with Compact Achromatic Interferometer", Optics and Lasers in Engineering, pp99-115, 13, 1990

14 Guild, J., "The Interference Systems of Crossed Diffraction Gratings: Theory of Moiré Fringes", Oxford at the Clardendon Press, 1965

15 Tuttle, M. E., Klein, R. J.,"Compressive Creep Strain Measurement Using Moiré Interferometry", Optical Engineering, pp630-635, v.27 No. 8, August 1988

16 Dadkhah, M. S., Wang, F. X., Kobayashi, A. S., "Simultaneous On-line Measurement of Orthogonal Displacement Fields by Moiré Interferometry", Experimental Techniques, pp28-30, July 1987

17 Lin, S. Y., Czarnek, R., Lee, J., "Integration and Processing of High-resolution Moiré-interferometry Data", Proceeding of SEM 1991 Spring Conference

18 Weathers, J. M., Foster, W. A., Swinson, W. F., Turner, J. L., "Integration of Laser-Speckle and Finite-Element Techniques of Stress Analysis", Experimental Mechanics, 25, pp60-65, March 1985.

19 Rowlands, R. E., Winters, K. D., Jensen, J. A., "Full-Field Numerical Differentiation", Experimental Mechanics, 18, pp177-183, March 1978

20 Segalman, D. J., Woyak, D. B., and Rowlands, R. E., "Smooth Spline-like Finite-element Differentiation of Experimental Data over Arbitrary Geometry", Experimental Mechanics, 19, pp429-437, December 1979.

21 Sanford, R. J., "Determining Fracture Parameters with Full-Field Optical Methods", Experimental Mechanics, 29, pp241-247, September 1989.

22 Barker, D. B., Sanford, R. J., and Chona, R., "Determining K and Related Stress-Field Parameters from Displacement Fields", Experimental Mechanics, 25, pp399-407 December 1985.

23 Parks, V. J., "Geometric Moiré", Handbook of Experimental Mechanics, ed. A. S. Kobayashi, Prentice Hall, Englewood Cliffs, New Jersey (1986)

24 Engelstad, S. P., "Hybrid Stress Analysis Using the Finite Element Method and Holographic Interferometry Data", Master Thesis, M. E. department, Auburn University Alabama, August 1983

VITA

Shih-Yung Lin

Shih-Yung Lin was born on August 14, 1960 in Keelung, Taiwan, Republic Of China. In 1978, he began his college education in the Civil Engineering Department of the National Cheng-Kung University in Tainan, Taiwan. Four years later, he graduated from the university and joined the Army of the Republic Of China as a second lieutenant in Engineering. In 1984, he was honorably discharged with award. Right after the military service, he was hired as a teaching and research associate in the Laboratory of Structures & Mechanics, Civil Engineering Department, National Cheng-Kung University.

In 1986, he decided to pursue higher education in the United States and entered the Engineering Science & Mechanics Department at Virginia Polytechnic Institute and State University. Concentrating on the mechanics of composite materials, he received his Master of Science degree in 1988. He believed that a practical experience would help his studies at VPI, so he joined E. I. duPont's Composite Division in Wilmington, Delaware during the summers of 1988 and 1989 as a research engineer. As he continued his studies at VPI, working towards a Ph. D. degree, he was concentrating on the moiré interferometry applied to the material study, especially to composite materials. He received his Ph. D. degree in May 1992, under the guidance of Professor Czarnek.